ABSTRACT

Title of Dissertation: DEVELOPMENT OF BILAYER ELECTROLYTE LT-SOFCs USING ALTERNATIVE BISMUTH OXIDES

Alireza Pesaran, Doctor of Philosophy, 2018

Dissertation directed by: Professor Eric D. Wachsman, Department of Chemical and Biomolecular Engineering

This work is primarily focused on the fabrication and performance of anode supported cells based on gadolinium doped ceria (GDC) and alternative stabilized bismuth oxide bilayer electrolyte that can operate at low temperatures (500-650 °C).The well-known bismuth-based electrolyte (ESB) undergoes ordering phenomena at temperatures ≤600°C, causing rapid decay in conductivity, and in turn the power output. As alternatives, two bismuth oxide compositions: (a) Neodymium-gadolinium stabilized bismuth oxide (NGSB) in rhombohedral phase, and (b)heavily doped composition, $(Bi_{0.75}Y_{0.25})_{1.86}Ce_{0.14}O_{3\pm\delta}$ (YCSB), with Y and Ce as co-dopants in cubic phase were evaluated in this work.

For the GDC/NGSB bilayer SOFCs, thickness of GDC and NGSB layers was varied between 23-70 μm and 0-25 μm, respectively. The results showed the addition of NGSB layer was effective in blocking electronic conduction which increased the OCV

compared to the baseline single layer GDC cell. Further, the relative and total thickness of the two layers showed a significant impact on the OCV of the cell at different temperatures with best performance obtained with cells with lower GDC thickness and higher NGSB thickness.

For the GDC/YCSB bilayer electrolyte SOFCs, a cell with a ~ 20 μm GDC layer and a ~12-13 μm YCSB layer, OCV and MPD of the cell at 650 ℃ reached 0.833 V and 760 mW/cm^2 respectively. OCV stability of this bilayer was measured for 50 hours at 625 and 600 ℃ (100 hours in total) and exceptional stability of OCV and ohmic ASR was observed. In comparison, the cell with 10GDC/ESB bilayer electrolyte showed a very rapid degradation of OCV at 600 ℃ (average hourly degradation rate of 0f -0.55%/h). and the ohmic ASR of the cell with GDC/ESB bilayer electrolyte at 600 ℃ increased by 5 times over the first 50 hours of operation mainly due to the conductivity decay of ESB.

Following the stable performance of GDC/YCSB bilayer electrolyte SOFCs, effect of GDC/YCSB thickness ratio on the performance of the cell was studied. It was shown that MPD of the bilayer electrolyte cells is higher than pristine GDC based cells with reduced ohmic *ASR* values. Specifically, a high MPD of ~1 W/cm^2 at 650℃ was achieved on a GDC(20μm)/ YCSB(12μm) bilayer electrolyte based SOFC, which is 62% higher than pristine GDC based SOFC (0.64 W/cm^2). Such enhancement is due to the 9.3% improvement in OCV (from 0.791 to 0.865 V) and a considerable 36% reduction in ohmic *ASR* values (from 0.094 to 0.069 Ω.cm^2).

Finally, to achieve high power density at low temperatures (≤ 600 ℃), a thin GDC (7-8 μm)/ YCSB (2 μm) bilayer electrolyte was used, and non-ohmic ASR of the cell was

drastically lowered *via* infiltration of Ni/GDC and LSM on anode and cathode, respectively. At 600 and 550 ℃, maximum power density (MPD) of the cell reached 1.73 and 1.25 W/cm^2, respectively, significantly higher than all previously reported values using non-cobalt cathode materials. The effect of infiltrating LSM on LSM-YCSB cathode was studied by varying temperatures and partial pressure of oxygen. It was revealed that by infiltrating the LSM/YCSB cathode with LSM nanoparticles, non-ohmic ASR of cathode reduced remarkably by one order of magnitude. Stability of the infiltrated symmetrical cell at 550 ℃ was measured over a period of 500 hours with no sign of decay.

DEVELOPMENT OF BILAYER ELECTROLYTE LT-SOFCs USING ALTERNATIVE BISMUTH OXIDES

by

Alireza Pesaran

Dissertation submitted to the Faculty of the Graduate School of the
University of Maryland, College Park, in partial fulfillment
of the requirements for the degree of
Doctor of Philosophy
2018

Advisory Committee:
Professor Eric D. Wachsman, Chair
Professor Raymond Adomaitis
Professor Chunsheng Wang
Professor Dongxia Liu
Professor Lourdes Salmanca-Riba

© Copyright by
Alireza Pesaran
2018

Dedication

I dedicate this to my parents for their unconditional love and endless support.

Acknowledgements

I would like to express my sincere and deep appreciation to my supportive advisor, Prof. Eric Wachsman, for his precious advices, encouragement, and patient guidance over the past three years. This dissertation would not have been possible without his continuous help, support and constructive comments.

I would also like to express my deep gratitude to my committee members, Prof. Raymond Adomaitis, Prof. Chunsheng Wang, Prof. Dongxia Liu, and Prof. Lourdes Salmanca-Riba for their invaluable advice and comments.

I am immensely grateful to Dr. Abhishek Jaiswal as my early mentor in the lab and training me on fabrication and testing of SOFCs and also helping me with building the experimental apparatus. His contributions and insights have been vital and extremely helpful for my research progress in this field. I am also very grateful to Dr. A. Mohammed Hussain for helping me with the infiltration studies and also preparing the manuscripts. He has been an absolutely invaluable resource in the lab for all SOFC group members and provided me with precious advices and productive comments all the times.

I would also like to thank my fellow graduate students and office mates, Dr. Yi-lin Huang, Mann Sakbodin, Ian Robinson, Patrick Stanely, Chrsitopher Pellegrinelli and Adam Jolley for our valuable discussions and conversations.

I must also acknowledge Dr. Peter Zavalij at Crystallographic Center (UMD) and Dr. Sz-Chian Liou at AIMLAB (UMD) for training me using the XRD and SEM machines, respectively.

I would like to acknowledge my funding agency, Advanced Research Project Agency-Energy (ARPA-E) of U.S. Department of Energy as well as my advisor, Prof. Eric Wachsman, for financially supporting me throughout this research.

I would truly be remiss without acknowledging my dear Arehzo. Although it has been only a year being together, she has always been a great source of love, inspiration, and motivation. She has always been very patient for my frustrations and complaints and I truly appreciate it.

I would also like to thank my brother and sister-like friends Mohammad and Roshanak for their continuous and unconditional friendship and helping me defeating the odds against me and treating me like a family member.

Last, but by no means least, I want to thank my parents, and my sister, Yasaman, who have given me unequivocal support, offered me selfless love throughout my life, and taught me the way of life, perseverance, humility, honesty and integrity. I am grateful that omnipresent God gave me the strength and provided me with the opportunity to accomplish this study.

Table of Contents

Dedication ii

Acknowledgements iii

Table of Contents v

List of Tables viii

List of Figures ix

List of Abbreviations and Acronyms xv

1 Introduction 1

1.1 History of SOFC Technology and Development Path 1
1.2 Benefits of SOFC Technology 3
1.3 SOFC Operating Basics 4
1.4 SOFC Components 7
1.4.1 Anodes 7
1.4.2 Electrolyte 9
1.4.3 Cathodes 13
1.5 Low-Temperature SOFCs 16
1.6 Ceria/Bismuth Oxide Bilayer Electrolyte SOFCs 17
1.7 Objectives 18
1.7.1 Alternative Bismuth Oxide Compositions 18
1.7.2 Effect of Thickness Ratio 22
1.7.3 Development of ceria/bismuth oxide bilayer electrolyte high-performance LT-SOFCs with nanostructured electrodes 22

2 Bilayer Electrolyte SOFCs-Literature Review 23

2.1 Electrolyte-supported SOFCs 24
2.1.1 2.1.1. Zirconia/Ceria Bilayer IT-SOFCs 24
2.1.2 Ceria/bismuth oxide bilayer IT-SOFCs 30
2.2 Electrode-supported Bilayer Cells 37
2.2.1 Zirconia/ceria bilayer IT-SOFCs 37
2.2.2 Zirconia/Bismuth oxide bilayer based IT-SOFCs 49
2.2.3 Ceria/bismuth oxide bilayer LT-SOFCs 50
2.3 Other types of bilayer electrolyte SOFCs 61
2.4 Final Remarks 62
2.5 Conclusions 63

3 Experimental Methods 65

3.1 Material Synthesis 65
3.1.1 Solid state 65
3.1.2 Sol-gel Method 66
3.2 X-ray Diffraction 66
3.3 Symmetrical-cell Fabrication and Testing 66
3.3.1 Symmetrical Cells for Electrical Conductivity Measurements 66
3.3.2 Symmetrical Cells for Studying Cathode Materials 67
3.3.3 Impedance Spectroscopy 68
3.4 SOFC Button-Cell Fabrication 69
3.4.1 Anode-supported Half-Cell Fabrication 69
3.4.2 Bismuth Oxide Layer Deposition 70
3.4.3 Cathode Deposition 72
3.5 Electrochemical Testing of anode-supported button cells 73
3.6 Post-testing Characterization 73
4 Development of Ceria/Rhombohedral Bismuth Oxide LT- SOFCs 75

4.1 Experimental Details 76
4.2 Phase Composition of Ceria and Bismuth Oxide Electrolyte 77
4.3 Electrical Conductivity of Ceria and Bismuth Oxide Electrolyte 79
4.4 Microstructure of GDC/NGSB Bilayer Electrolyte SOFCs 81
4.5 Electrochemical Performance 85
5 Development of a New Ceria/ Yttria-Ceria Double Doped Bismuth Oxide Bilayer

Electrolyte Low-Temperature SOFC with high Electrochemical Stability 92

5.1 Experimental 93
5.2 Results and Discussion 96
5.2.1 Phase Purity 96
5.2.2 Electrical Conductivity 98
5.2.3 Microstructure 101
5.2.4 Electrochemical Performance 103
5.2.5 Electrochemical Stability 108
6 Optimizing Bilayer Electrolyte Thickness Ratios for High Performing Low-

Temperature Solid Oxide Fuel Cells 113

6.1 Experimental Details 114
6.2 Results and Discussion 115
6.2.1 Effect of the YCSB/GDC thickness ratio and GDC thickness on power output 117
6.2.2 Effect of YCSB/GDC thickness ratio and GDC thickness on OCV 121
6.2.3 Effect of YCSB/GDC thickness ratio and GDC thickness on ohmic and non-ohmic losses 126
7 High-Performance Low-Temperature Solid Oxide Fuel Cell Using Bilayer

Electrolyte and Nanostructured Electrodes 133

7.1 Experimental 134
7.1.1 Symmetrical Cell fabrication 134
7.1.2 Anode-supported button Cell fabrication 135
7.2 Results and Discussion 136
7.2.1 GDC/YCSB Bilayer fabrication using PLD 136
7.2.2 SOFC Testing and Analyses 138
7.2.3 SOFC Electrochemical Stability 141
7.2.4 Microstructure 142
7.2.5 Symmetrical cells 144
8 Conclusions and Future Works 149

8.1 Future Works 152
References 154

List of Tables

Table 2-1 Cell configuration, processing, and performance of zirconia/ceria bilayer based IT and HT-SOFCs 28

Table 2-2 Cell configuration, processing, and performance of ceria/bismuth oxide bilayer based LT and IT-SOFCs 34

Table 5-1 Compositions of the anode, electrolytes, and cathode for three tested cells 95

Table 5-2 Electrochemical performance of cells A, B, and C across the temperature range of 650-500 ℃ 107

Table 6-1 OCV of ceria/bismuth oxide bilayer electrolyte SOFCs as a function of Ceria thickness and bismuth oxide/ceria thickness ratio across the temperature range of 650-500 ℃ 125

Table 7-1 Comparison of Cell structure, materials, and MPD in the temperature range of 500-600 ℃ 140

List of Figures

Figure 1-1 Schematic of a solid oxide fuel cell 5

Figure 1-2 Typical I-V plot of an SOFC..... 7

Figure 1-3 Ionic conductivity of $(CeO_2)_{0.8}(LnO_{1.5})_{0.2}$ at 800 ℃ as a function of dopant ionic radius [9] 11

Figure 1-4 Ionic conductivity of $Ce_{1-x}Gd_xO_{2-x/2}$ at 500 ℃ as a function of Gd concentration [10] 11

Figure 1-5 Comparison of ionic conductivity of different electrolyte materials [12]. 13

Figure 1-6 Schematic of effect of relative thickness of SDC/ESB bilayer on interfacial oxygen partial pressure (pO2) and ESB stability [14] 18

Figure 1-7 Unit cell of cubic fluorite Bi_2O_3..... 19

Figure 1-8 Conductivity stability of NGSB, ESB, and DWSB [55]..... 21

Figure 1-9 Conductivity stability of YCSB (BYC7) at 650, 600, and 500 ºC [56, 57] 21

Figure 2-1 I-V characteristics of monolayer GDC cell at 600 (closed circle) and 700 (open circle) °C and YSZ/GDC bilayer electrolyte cell at 600 (closed triangle) and 700 (open triangle) °C [43] 24

Figure 2-2 Plots of measured electrochemical potential (φ) in Ni-YSZ/YSZ/GDC/LSC-GDC cell under open circuit (a), under intermediate load (c), and under short circuit condition (e). Plots of measured electrochemical potential (φ) in Ni-GDC/GDC/YSZ/LSM-YSZ cell under open circuit (b), under intermediate load (d), and under short circuit condition (f).[58] 26

Figure 2-3 Conductivity of SDC, YSZ/SDC bilayer (YSZ film) and single crystal YSZ samples [75] 30

Figure 2-4 Bright field image of YSZ/SDC sample for EDS elemental analysis. [75] 30

Figure 2-5 OCV as a function of temperature for GDC and GDC/ESB electrolytes. Thickness of ESB layer for GDC/ESB-2 is six times that of GDC/ESB-1 [14]..... 33

Figure 2-6 Grain conductivities of ESB/SDC and SDC and grain boundary conductivies of ESB/SDC and SDC by geometric method (G) and capacitance method (C)[37]..... 36

Figure 2-7 Theoretical and measured OCV of monolayer GDC(10 μm) cell, monolayer YSZ(10 μm) cell, and bilayer YSZ(3 μm)/GDC(7 μm) cell [63] 38

Figure 2-8 I-V characteristics of ScSZ/SDC bilayer electrolyte unit cell using SSC cathode [Zhang, X., et al. Journal of Power Sources, 2008. 175(2)][65] 40

Figure 2-9 Measured OCV value of bilayer YSZ/GDC(1 μm) cells at 600 °C as a function of YSZ thickness. Solid line indicates calculated OCV of GDC with ti = 0.5 and dotted line indicates OCV of YSZ.[70]..... 43

Figure 2-10 I-V characteristics of YSZ/SDC bilayer electrolyte unit cells with various YSZ layer thickness at 600 °C [70] 43

Figure 2-11 Schematic representation of Ceres Power "Steel Cell" [91]..... 46

Figure 2-12 Average cell power and longest durability tests of Ceres Power "Steel Cell" technology over years [91] 47

Figure 2-13 I-V characteristics and impedance spectra of monolayer YSZ cell and YSZ/ESB bilayer electrolyte cell at 700 °C using humidified H2 and air at anode and cathode sides respectively [106] 50

Figure 2-14 Backscattered SEM image showing cross-section of Ni-GDC/GDC(50 μm)/ESB(20 μm)/BRO-ESB/BRO cc unit cell. cc refers to current collector [47].... 52

Figure 2-15 I-V characteristics and impedance spectra of monolayer GDC cell and GDC/ESB bilayer electrolyte cell made by hot/cold PLD [47]..... 53

Figure 2-16 I-V characteristics of (a) GDC/ESB and (b) SNDC/ESB bilayer electrolyte unit cells using LBSM-ESB cathode [109]..... 57

Figure 3-1 Schematic of (a) an electrolyte material, and (b) cathode material symmetrical cell using gold and silver mesh as current -collector 67

Figure 3-2 Experimental apparatus to measure the impedance of symmetrical cells. 68

Figure 3-3 Schematic of bilayer SOFCs manufacturing procedure..... 70

Figure 3-4 Tape-caster (Procast, TC-71LC) used for fabrication of ASL, AFL, and GDC tapes..... 70

Figure 3-5 Fabricated anode supported (a) single GDC electrolyte, and (b) GDC/ESB bilayer electrolyte button cells..... 72

Figure 3-6 Button-cell I-V and impedance testing reactor 74

Figure 4-1 XRD pattern of GDC and NGSB electrolyte powders..... 78

Figure 4-2 XRD pattern of thin film NGSB deposited by PLD on AFL/ASL/GDC half-cells 79

Figure 4-3 Arrhenius plot of grain, grain boundary, and total conductivity of GDC . 80

Figure 4-4 Arrhenius plot of total conductivity of NGSB with heating/cooling cycles 81

Figure 4-5 Representative SEM micrographs of ASL/AFL/GDC/NGSB/LSM-ESB cells at two different magnifications 1,000x and 2,000x – (a), (b) GDC (~23 μm); (c), (d) GDC (~21 μm) / NGSB (~3.6 μm); (e), (f) GDC (~39 μm) / NGSB (~22.3 μm). 82

Figure 4-6 Surface SEM micrographs on GDC and NGSB layers 83

Figure 4-7 EDX line scan for GDC/NGSB interface; NGSB deposited by PLD at 600 ℃ 84

Figure 4-8 SEM micrographs on GDC/NGSB bilayer cells; NGSB deposited by PLD at 600 ℃ 84

Figure 4-9 EDX elemental mapping scan for GDC/NGSB interface; NGSB deposited by PLD at 600 ℃ 85

Figure 4-10 Effect of NGSB thickness on OCV for three GDC thicknesses – ~23, ~38, and (c) ~78 μm 86

Figure 4-11 Effect of GDC thickness on OCV for three NGSB thicknesses (a) 0, (b) 3-9, (c) 12-25 μm 87

Figure 4-12 Open circuit voltage stability of (a) GDC (~23 μm)/NGSB (~9 μm) and (b) GDC (~74 μm)/NGSB (~3 μm) bilayer cells at 500 ℃ and 600 ℃ 90

Figure 4-13 . I-V (filled symbols) and power density (open symbols) of GDC (~20 μm)/NGSB (~4 μm) bilayer cell at 500-650 ℃ 91

Figure 5-1 XRD patterns for YCSB powder synthesized by solid-state (SS) route calcined at 900 and 950 ℃, and sol-gel route calcined at 600 and 800 ℃ 97

Figure 5-2 XRD patterns for LSM-YCSB mixture annealed at 800 ℃ and 850 ℃ for 10 hours 97

Figure 5-3 XRD patterns for BRO7-YCSB mixture annealed at 800 ℃ and 850 ℃ for 10 hours 98

Figure 5-4 Arrhenius plot of ESB, DWSB, and YCSB electrical conductivity measured in air and under OCV condition across the temperature range of 650-350 ℃ using gold and silver mesh as current collector 99

Figure 5-5 Stability of electrical conductivity of YCSB, ESB, and DWSB at 500 ℃ 100

Figure 5-6 stability of electrical conductivity of YCSB at 500, 600, and 650 ℃ ... 100

Figure 5-7 SEM micrographs of GDC/ YCSB (Sol-Gel) bilayers sintered at 775, 825, and 875 ℃ for 2 hours (upper row) and GDC/ YCSB(Solid-state) bilayers sintered at 775, 900, and 1000 ℃ for 2 hours (bottom row). 102

Figure 5-8 (a) EDX elemental mapping, and (b) line scan of GDC/YCSB bilayer interface sintered at 1000 ℃ for 2 hours 102

Figure 5-9 SEM micrographs of NiO-GDC/GDC/ESB/LSM-ESB baseline cell (top row) and NiO-GDC/GDC/YCSB/LSM-YCSB cell (bottom row) 103

Figure 5-10 I-V and power density curves for cell A 104

Figure 5-11 I-V and power density curves for cell B 105

Figure 5-12 I-V and power density curves for cell C 105

Figure 5-13 Nyquist plots for cells A, B, and C across the temperature range of 500-650 ℃ 107

Figure 5-14 stability of NiO/GDC/ESB/LSM-ESB (Cell A), NiO-GDC/GDC/YCSB/LSM-YCSB (Cell B), and NiO-GDC/GDC/YCSB/BRO7-YCSB (Cell C) at 600 ℃, and 625 ℃..... 109

Figure 5-15 ohmic and non-ohmic ASR stability of NiO/GDC/ESB/LSM-ESB (Cell A) at 600 and 625 ℃..... 110

Figure 5-16 ohmic and non-ohmic ASR stability of NiO/GDC/YCSB/LSM-YCSB (Cell B) at 600 and 625 ℃..... 111

Figure 5-17 ohmic and non-ohmic ASR stability of NiO/GDC/YCSB/BRO7-YCSB (Cell C) at 600 and 625 ℃..... 111

Figure 6-1 Schematic of anode-supported GDC/YCSB bilayer electrolyte SOFCs. 115

Figure 6-2 Schematic of a YCSB/GDC bilayer electrolyte SOFC showing the effect of bilayer electrolyte in reducing the average μO2 inside GDC electrolyte 116

Figure 6-3 (a) MPD (W/cm^2) of 10 μm single electrolyte GDC (thickness ratio 0) and YCSB/GDC bilayer electrolyte SOFCs as a function of thickness ratio across the temperature range of 650-50 ℃, (b) Voltage-current curves (left axis) and power-current curves (right axis) for 10 μm GDC electrolytes with three different YCSB/GDC thickness ratios (0, 0.33 , and 1.1) at 650 ℃, and SEM micrographs of 10 μm GDC cells with YCSB/GDC thickness ratios of (c) 0, (d) 0.33, and (e) 1.1 118

Figure 6-4 (a) MPD (W/cm^2) of 20 μm single electrolyte GDC (thickness ratio 0) and YCSB/GDC bilayer electrolyte SOFCs as a function of thickness ratio across the temperature range of 650-50 ℃, (b) Voltage-current curves (left axis) and power-current curves (right axis) for 20 μm GDC electrolytes with three different YCSB/GDC thickness ratios (0, 0.14 , and 0.57) at 650 ℃, and SEM micrographs of 20 μm GDC cells with YCSB/GDC thickness ratios of (c) 0, (d) 0.14, and (e) 0.57 119

Figure 6-5 (a) MPD (W/cm^2) of 40 μm single electrolyte GDC (thickness ratio 0) and YCSB/GDC bilayer electrolyte SOFCs as a function of thickness ratio across the temperature range of 650-50 ℃, (b) Voltage-current curves (left axis) and power-current curves (right axis) for 40 μm GDC electrolytes with three different YCSB/GDC thickness ratios (0, 0.10 , and 0.55) at 650 ℃, and SEM micrographs of 40 μm GDC cells with YCSB/GDC thickness ratios of (c) 0, (d) 0.10, and (e) 0.55 121

Figure 6-6 Effect of YCSB/GDC thickness ratio on the OCV of (a) 10 μm GDC cells, (b) 20 μm GDC cells, and (c) 40 μm GDC cells across the temperature range of 650-500 ℃. Thickness ratio zero refers to single electrolyte GDC cell with no YCSB layer..... 122

Figure 6-7 Representative Nyquist plots for (a)10 μm GDC- inset: equivalent circuit to model the impedance spectra, (b)20 μm GDC, and (c) 40 μm GDC bilayer cells with different YCSB/GDC thickness ratios at 650 ℃..... 127

Figure 6-8 Ohmic ASR of the YCSB/GDC bilayer SOFCs normalized to the single GDC electrolyte cell for (a)10 μm, (b)20 μm, and (c) 40 μm GDC cells across the temperature range of 650-500 ℃..... 128

Figure 6-9 Effect of pO2 on the electrical conductivity of 10GDC and 20GDC [136] 129

Figure 6-10 Ohmic ASR (Ω.cm2) of 20 μm GDC cells as a function on YCSB/GDC thickness ratio across the temperature range of 650-500 ℃. Dot lines represent theoretical ohmic ASR of the electrolyte(s) using their conductivity in air 131

Figure 6-11 Normalized non-ohmic ASR of 10, 20, and 40 μm GDC cells with different YCSB/GDC thickness ratio at 650 ℃..... 132

Figure 7-1 SEM micrographs of YCSB/GDC bilayer samples; YCSB was deposited by PLD at 600 ℃. (a)the cross-section, and (b)surface of the as-deposited sample, (c) cross-section, and (d) surface of the sample annealed at 775 ℃ for 2 hours. 137

Figure 7-2 (a) EDX line scan for GDC/YCSB interface, and (b) EDX elemental mapping scan for GDC/YCSB interface; YCSB deposited by PLD at 600 ℃ and annealed at 775 ℃ for 2 hours..... 137

Figure 7-3 I-V and power density curves for (a) Cell (A), (b) Cell (B); Nyquist plot for (c) Cell (A), (d) Cell (B) at 500-600 °C..... 138

Figure 7-4 Electrochemical stability of Cell (B) at 550 ℃ ;(a) Cell voltage under the constant current density of I=1 A/cm2, (b) OCV, (C) ohmic and non-ohmic ASR of the Cell (B), and (d) MPD..... 142

Figure 7-5 SEM micrographs of (a) Ni-GDC/GDC/YCSB/LSM-YCSB cell and GDC/YCSB bilayer electrolyte at (b) 5.00k and (c) 15.00 k magnifications after electrochemical testing..... 143

Figure 7-6 SEM micrographs of (a) LSM infiltrated LSM-YCSB cathode near the YCSB electrolyte interface, and (b) Ni-GDC infiltrated AFL near GDC electrolyte interface after electrochemical testing 144

Figure 7-7 Impedance spectra of (a) LSM-YCSB and (b) LSM infiltrated LSM-YCSB across the temperature range of 650-500 ℃ measured at OCV in air, and (c) Arrhenius plot of non-ohmic ASR of LSM-YCSB and LSM infiltrated LSM-YCSB in air 145

Figure 7-8 (a) impedance spectra of LSM-YCSB and LSM infiltrated LSM-YCSB at 0.5 and 0.1 atm at 550 ℃, and (b) pO2 dependence of non-ohmic ASR for both LSM-YCSB and LSM infiltrated LSM-YCSB at 550 and 600 ℃..... 147

Figure 7-9 Non-ohmic ASR stability of LSM infiltrated LSM-YCSB and LSM-ESB [203] at 550 ℃..... 148

Figure 7-10 Stability of total ohmic ASR of the LSM infiltrated LSM-YCSB symmetrical cell at 550 ℃..... 148

List of Abbreviations and Acronyms

η	Efficiency, overpotential
ΔG^0	Gibbs free energy
ΔH^0	Enthalpy
AFL	Anode functional layer
ASL	Anode support layer
ASR	Area specific resistance
BBP	Butyl benzyl phthalate
BRO7	Bismuth ruthenium oxide
BSCF	Barium strontium cobalt ferrite
BZCY	Barium cerium oxide doped with zirconia and yttria
DGSB	Dysprosium gadolinium stabilized bismuth oxide
DWSB	Dysprosium tungsten stabilized bismuth oxide
EDS	Energy dispersive x-ray spectroscopy
EIS	Electrochemical Impedance Spectroscopy
ESB	Erbium stabilized bismuth oxide
Emf	Electromotive force
ESL	ElectroScience (company)
F	Farady's constant
GDC	Gadolinium doped ceria
I	Current
I-V-P	Current-voltage-power (referring to power density curves)
LBAYO	Lanthanum barium yttrium oxide
LBSM	Lanthanum bismuth strontium manganese oxide
LSCF	Lanthanum strontium cobalt iron oxide
LSGM	Lanthanum gallate doped with strontium and magnesium
LSM	Lanthanum strontium manganite
LYBO	Lanthanum yttrium stabilized bismuth oxide
MIEC	Mixed ionic electronic conductor
MPD	Maximum power density
n	Number of moles of ions
NbSB	Niobium stabilized bismuth oxide
NGSB	Neodymium gadolinium stabilized bismuth oxide
OCV	Open circuit voltage
ORR	Oxygen reduction reaction
pH_2O	Partial Pressure of H_2O
pO_2	Partial pressure of oxygen
PVB	Polyvinyl butryal
R	Universal gas constant
ScSZ	Scandia stabilized zirconia
SDC	Samarium doped ceria
SEM	Scanning electron microscopy
SNDC	Samarium neodymium doped ceria

SOFC	Solid oxide fuel cell
SS	Solid state
SSC	Samarium strontium cobalt oxide
T	Temperature
TPB	Triple phase boundary
V	Voltage
$V_{\ddot{O}}$	Oxygen vacancy
XRD	X-ray diffraction
YCSB	Yttrium cerium stabilized bismuth oxide
YDC	Yttrium doped ceria
YSB	Yttria stabilized bismuth oxide
YSZ	Yttria stabilized zirconia

1 Introduction

1.1 History of SOFC Technology and Development Path

The earliest demonstration of solid oxide fuel cell (SOFC) technology dates to 1934 when Emil Bauer and Hans Pries successfully generated power using a SOFC with zirconia electrolyte and Fe_3O_4 and carbon as cathode and anode materials respectively. Following that, in 1943, Carl Wagner was the first to identify the existence of oxygen vacancy in the zirconia structure and hence explained the electrical conductivity of zirconia at elevated temperatures as a result of the movement of such vacancies and conducted a more through and systematic study of SOFCs [1]. Zirconia-based materials such as yttria-doped zirconia (YSZ) remained the state-of-the-art electrolyte for over 100 years. However, the conductivity of YSZ rapidly decreases as the temperature decreases below 800 ºC and hence over the past 25 years, tremendous amount of effort has been made into replacing the YSZ with other electrolyte materials with higher ionic conductivity at lower temperatures. At the same time, replacing the precious metals such as platinum and gold as cathode by alternative materials with higher catalytic activity and electrical conductivity such as doped $LaMnO_3$ and doped $LaCrO_3$ has been the focus of many scholars in the field of SOFC technology. In addition to the extensive exploration of new materials for SOFC major components (electrolyte and electrodes) aimed at improving performance metrics such as open circuit voltage (OCV), power density, and area specific resistance (ASR), implementation of advanced thin film fabrication (for low temperature applications) and characterization devices such as pulsed laser deposition (PLD), atomic layer deposition (ALD), and cutting-edge

sputtering, has been the spotlight of many scholarly works in the field. In terms of SOFC structure and design, significant improvements have been made. Early SOFC designs were electrolyte-supported. Such SOFCs with a few hundred microns thick electrolyte, normally suffered from low power density due to the long path for oxygen ions to transfer. However, modern SOFCs have a thin electrolyte layer with supporting porous substrates that could be either the cathode or anode. De souza et al. [2] demonstrated an anode-supported SOFC by co-firing the anode and electrolyte and subsequent insertion of the cathode and showed a significant improvement in the performance. Practical alternative substrates including ceramic or porous stainless-steel interconnect materials. Following the advent of high-tech lithography and deposition devices, An et al.[3] successfully demonstrated a free-standing electrolyte micro-SOFC with an electrolyte thickness of less than 100 nm and achieved a record-breaking performance of 1.3 W/cm^2 at 450 ºC. As far as geometry is considered, SOFCs are made in two distinctive designs: (a) tubular SOFCS (usually for cathode-supported cells), and (b) planar stacks (usually for anode-supported).

As concisely discussed above, the primary research trends in field of SOFCs can be categorized into three sections: (a) development of new electrolyte and cathode materials for improved performance and stability (b) cell fabrication routes and use of advanced deposition devices for making thin film electrolyte SOFCs, and (C) design of cell stacks and integration into power cycles. While the primary focus of the academic scholar works is on the development of new materials and fabrication routes, cell-stack design and integration have more significance to industrial partners and

manufacturers. In the next section, the benefits and principles of SOFC operation will be outlined briefly.

1.2 Benefits of SOFC Technology

SOFC is an electrochemical device which directly converts the chemical energy of a fuel into electrical energy. The conversion is direct without the need for intermediate conversion into heat and mechanical energy, as in the case of traditional turbine/generator systems and is not limited by the Carnot cycle with electrical efficiency up to 50 % achievable [4]. The efficiency is determined by the ratio of the Gibbs free energy to the total enthalpy of the fuel as shown in eqn. (1)

$$\eta_{Fuel\ Cell\ (Theoritical)} = \frac{\Delta G^0}{\Delta H^0} \quad (1)$$

Higher electrical efficiency yields significantly less CO_2 emissions and thus makes the SOFC technology an environmentally friendly power production path. Due to the lower operating temperature of SOFCs comparing to the combustion engines, SOFCs benefit from negligible NOx and SOx emissions. Additionally, fuel cells have limited moving parts (blower) and hence run quietly with essentially no vibration.
Additionally, SOFCS produce high-quality waste heat that can be integrated to combined heat and power (CHP) cycles to further improve the overall system efficiency up to 85% [5].

Unlike many other types of fuel cells, SOFCs ideally have the capacity to internally reform the fuel in presence of catalysts and thus do not require an external fuel reformer and are compatible with various hydrocarbon fuels. The other noticeable advantage of the SOFC technology is that it allows localized, grid-independent power production

which, not only circumvents the power transmission losses but also reliably produces power in the events of grid outage. Lastly, SOFCs have modular designs which enables the easy scale-up and hence provides various applications from small scale such as residential (1-10 kW) to industrial and central power plants (up to 100 MW).

1.3 SOFC Operating Basics

The basic operating principles of a SOFC is schematically shown in Figure **1-1**. At the anode side, fuel such as hydrogen is oxidized and reacts with the oxygen at the catalyst sites (such as nickel) and forms water and free electrons. When the external load is applied to the circuit, electrons transfer through the external circuit and provide useful work. At the cathode side, electrons reduce the oxygen and forms oxygen ions which is transported through the electrolyte. The anodic and cathodic reactions (in kröger-vink notation) of an SOFC using hydrogen as fuel are shown in eqns. (2) and (3) respectively:

$$O_O^X + H_2 \rightarrow H2O + 2e^- + V_{\ddot{O}} \quad (2)$$

$$\frac{1}{2}O_2 + 2e^- + V_{\ddot{O}} \rightarrow O_O^X \quad (3)$$

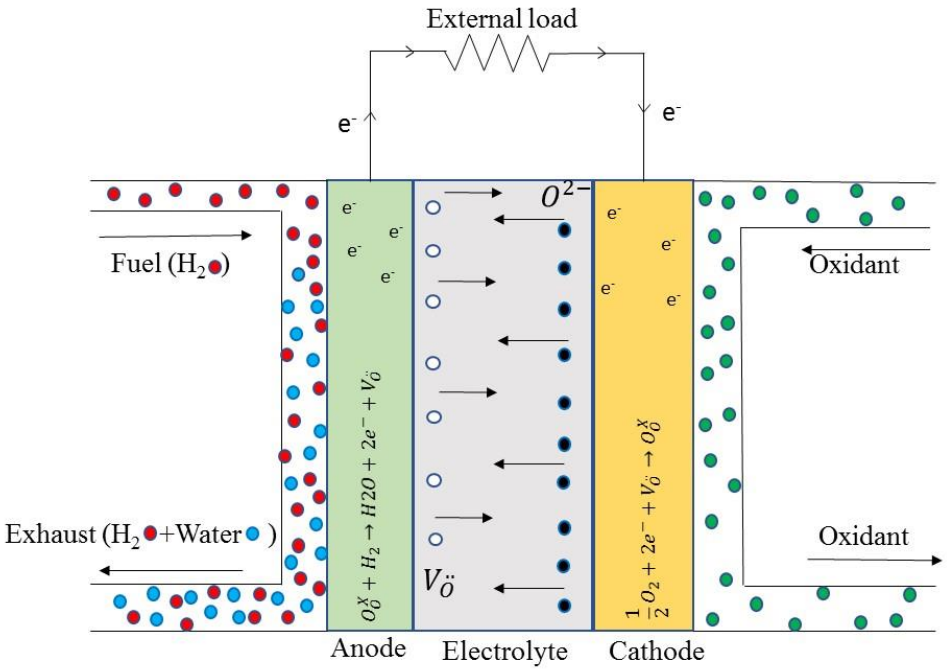


Figure 1-1 Schematic of a solid oxide fuel cell

The difference between the chemical potential of oxygen at the cathode and anode sides produces the electrical potential difference across the cell. The useful work produced by a galvanic cell such as SOFC occurs through transporting the charged species across the potential difference. As shown in eqn. (1), the efficiency of an SOFC is determined by the change of the Gibbs free energy of the system, where for a galvanic cell is calculated by the Nernst equation as shown in eqn.(4)

$$\Delta G = -zFEn \tag{4}$$

Where *n* is the number of moles of ions, *z* is the valence charge, *F* is Faraday's constant, 96485 C/mol and *E* is the electromotive force (EMF) of the cell. For an SOFC operating on hydrogen with anodic and cathodic reaction shown in eqn .(3) and eqn. (4), EMF of the cell is calculated from eqn .(5):

$$E = E^0 - \frac{RT}{2F} ln \frac{P_{H2O}}{P_{H_2} P_{O2}^{\frac{1}{2}}} \tag{5}$$

Where *R* and *T* are the universal gas constant and operating temperature of the system respectively. As shown in eqn. (5), OCV of the cell decreases with increase of temperature and ($\frac{P_{H2O}}{P_{H2}}$). In an actual fuel cell, the efficiency of the cell is lower than the theoretical value and can be calculated from eqn. (6):

$$\eta = \eta_T \times \eta_v \times \eta_f = \left[\frac{\Delta G(T,P)}{\Delta H^o_{r298}}\right] \times \left[\frac{V}{EMF}\right] \times \left[\frac{i/nF}{v_f}\right] \quad (6)$$

Where η_T, η_v, and η_f are theoretical efficiency, voltage efficiency and fuel utilization efficiency respectively. The actual voltage across the cell is smaller than the EMF of the cell and decreases due to: (a) activation polarization loss caused by reaction kinetics at the cathode and anode sides of the SOFC, (b) ohmic polarization losses due to the solid electrolytes, and (c) concentration polarization losses due to the mass transport of gaseous fuel and reaction products. The actual voltage across the cell is calculated using eqn. (7).

$$V(I) = EMF - \eta_{ohmic} - (\eta_{act+}\eta_{conc})_{anode} - (\eta_{act+}\eta_{conc})_{cathode} \quad (7)$$

Where η_{act} , and η_{conc} refer to activation and concentration overpotentials, respectively. Typical I-V plot of an SOFC is shown in **Figure 1-2**. Open circuit potential of the cell is determined by the electronic current leakage through the electrolyte (intrinsic to the nature of the material and its ionic transference number) and gas leakage through the electrolyte. At low current densities, sluggish kinetics of oxygen reduction reaction (ORR) at the cathode side and fuel oxidation kinetics controls the overpotential of the cell. At intermediate current densities, ohmic resistance caused by the electrolyte of the cell is responsible for the major voltage drop

and at high current densities diffusion of the fuel into the electrodes particularly at the anode side for the anode-supported SOFCs dominates the overpotential of the cell.

Enhancing the performance of the cell, essentially requires the minimization of ohmic and non-ohmic losses as well as increasing the open circuit potential of the cell. While the activation and concentration polarization losses are primarily controlled by the electrodes, the open circuit potential and ohmic polarization loss of the cell is largely governed by the electrolyte material and thickness. In the next section, a concise review on different components of an SOFC, i.e. Anode, electrolyte, and cathode will be provided.

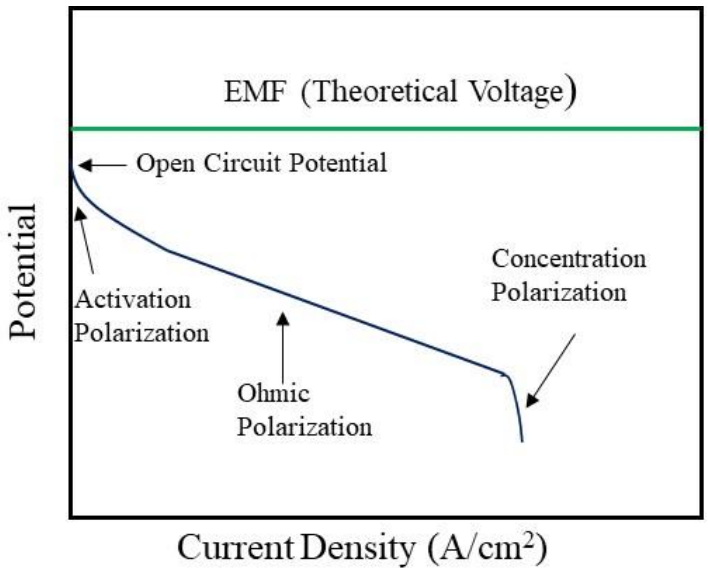


Figure 1-2 Typical I-V plot of an SOFC

1.4 SOFC Components

1.4.1 Anodes

As mentioned earlier, at the anode side, fuel is oxidized and releases the electrons into the external circuit. An appropriate anode material must possess certain qualities. Having sufficient catalytic activity to oxidize the fuel and high electrical conductivity

to conduct the electrons through the anode and into the external circuit are quite crucial for achieving a reasonable power density. Thermal expansion coefficient (TEC) of the anode must be close to that of the electrolyte and hence cermet composites (a mixture of metal and ceramic) are quite common in the state-of-the-art SOFCs. Anode material should be chemically compatible with the electrolyte material under reducing atmosphere and elevated temperatures. Triple phase boundary (TPB), porosity, particle size, and grain size distribution, impact the performance of an anode material significantly and must be tuned carefully[6]. Ni/YSZ cermets are typically used in SOFCs using hydrogen as fuel. Ni as a metal has sufficient catalytic activity to break the hydrogen and CO fuel bonds and it is cheap. The addition of the ceramic component matches the TEC of the anode to that of the electrolyte and prevents the coarsening of Ni particles to some extent. Also, addition of the ceramic component into the anode structure enhances the ionic conductivity of the anode. At approximately 30% volume Ni (Ni percolation) conductivity of the Ni cermets reaches its maximum value[7]. Chemical composition and microstructure play important roles in the performance of the anodes as shown by Ohara et al. [8]. They studied the performance of Ni-Samaria doped ceria cermet anodes as a function of Ni content and found that a cermet with a Ni content of around 50 vol% showed the lowest anodic polarization (~30 mV at 300 mA/cm^2, 800 ºC). At lower temperatures, catalytic and surface activity of nickel for electrochemical oxidation, as well as, for coking and sulfur tolerance reduces. In this respect, Ni-ceria cermet provides advantage due to high activity compared to Ni-zirconia for anode reactions. Doped ceria has mixed ionic-electronic conductivity under reducing atmosphere and enhances the performance of the anode.

1.4.2 Electrolyte

Oxygen ion conducting solid electrolytes are the backbone of SOFCs, allowing selective transport of oxygen ions for electrochemical oxidation of fuel to generate electrical power. In contrast to the electrodes, which must have high electrical conductivity, a robust electrolyte blocks the internal electronic current (ionic transference number close to 1) and forces the electrons to migrate through the external circuit. To meet such requirements, electrolyte materials should have a large band gap and under reducing atmosphere should not have multiple oxidation states. Although various kinds of ions can be transported in an electrolyte, modern SOFCs are based on oxygen ion transport membranes. Oxygen vacancy in the lattice structure, which is normally generated by doping the host lattice with a lower valance cation, is the primary mechanism of oxygen conduction in these materials. Typically, doped fluorite and perovskite materials have loose bonds with oxygen in their lattice and accept a wide range of dopants in their structure and thus exhibit acceptable oxygen ion conductivity. Doped zirconia is the most explored electrolyte material. Cubic structure of zirconia can be stabilized at room temperature up to its melting point by doping with aliovalent ions. Doped zirconia has higher oxygen vacancy concentration and thus exhibits higher conductivity according to the reaction below shown in kröger-vink notation:

$$M_2O_3 + ZrO_2 \rightarrow 2M'_{Zr} + V_{\ddot{O}} + 3O_O^X \quad (8)$$

Zirconia is typically doped with CaO, MgO, Y_2O_3, Sm_2O_3 and Sc_2O_3 and considering the conductivity values, YSZ and ScSZ are far more common than other stabilized

zirconia materials. The conductivity of stabilized zirconia varies as a function of dopant concentration and 8% mole has the highest conductivity. YSZ has ionic transference number close to 1 and benefits from great chemical stability. However, the conductivity of YSZ rapidly decreases as the operating temperature decreases below 800 ºC and hence alternative electrolyte materials must be explored. Doped ceria has a conductivity one order of magnitude higher than YSZ at lower temperatures and thus has been suggested as an electrolyte material for intermediate-temperature SOFCs. Ce^{4+} has a larger ionic radius comparing to Zr^{4+} and thus the structure is far from closed pack providing a clearer path for oxygen conduction. Unlike zirconia, ceria has a cubic structure across the entire temperature range (room temperature to the melting point) and the primary function of doping is to increase the oxygen vacancy concentration and enhance the conductivity. Among different alkaline earth and rare earth dopants, Gd_2O_3, Y_2O_3, and Sm_2O_3 have been extensively explored. Gd^{3+} and Sm^{3+} have the smallest radius mismatch with Ce^{4+} and thus smaller stress inside the lattice is created which results in a lower activation energy and higher oxygen ion conductivity (Figure **1**-**3**) [9]. Similar to YSZ, doped ceria conductivity varies with composition and 10% mole doped ceria with gadolinium (10GDC) is the most common ceria-based electrolyte for IT and LT-SOFCs [10] (Figure **1**-**4**).

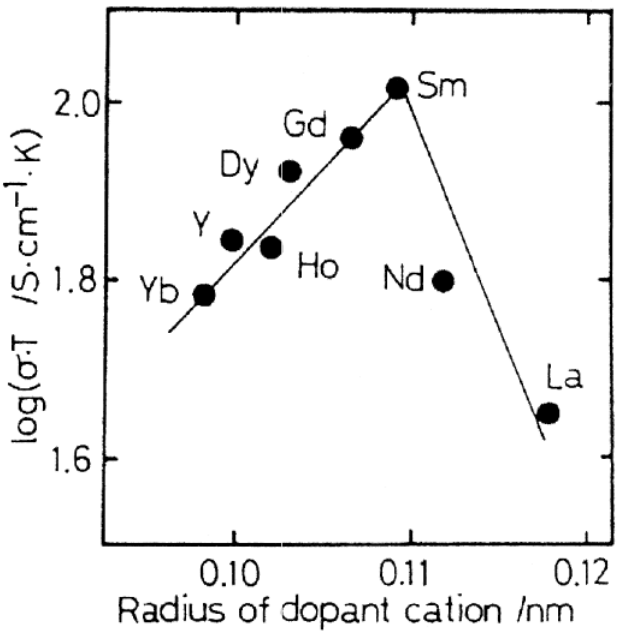


Figure 1-3 Ionic conductivity of $(CeO_2)_{0.8}(LnO_{1.5})_{0.2}$ at 800 ℃ as a function of dopant ionic radius [9]

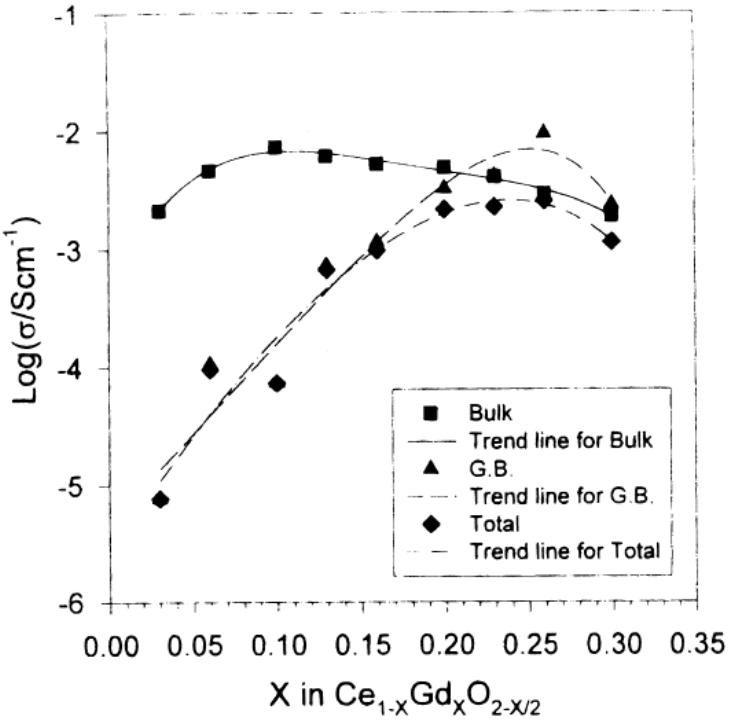


Figure 1-4 Ionic conductivity of $Ce_{1-x}Gd_xO_{2-x/2}$ at 500 ℃ as a function of Gd concentration [10]

Unfortunately, at elevated temperatures and reducing atmospheres of fuel at the anode side, doped ceria undergoes a reduction of Ce^{4+} to Ce^{3+} which creates an internal electronic current caused by small polaron hopping. Internal short circuit results in a lower OCV than the theoretical EMF and can significantly dissipates the power output of the cell and hence must be minimized [11]. To block the internal current, insertion of a second electrolyte layer with an ionic transference number close to unity has been explored. Such SOFCs are typically referred to as bilayer electrolyte SOFCs. Bilayer electrolyte SOFCs differ based on the nature of the electrolyte materials and functionality of each electrolyte in the structure of the cell. More details of bilayer SOFCs will be provided in next sections.

Bismuth oxide based electrolytes show the highest oxygen ion conductivity among all solid electrolytes and are of considerable interest for application in SOFCs, ion transport membranes, and oxygen sensors [12]. Stabilized bismuth oxide shows high ionic conductivity due to high concentration of disordered oxygen ion vacancies (25%) in δ-Bi_2O_3 along with the high polarizability of Bi^{3+} cation and high mobility of anions [13-16]. A comparison of the conductivity of different electrolyte materials is shown in Figure **1-5** [12]. As demonstrated, oxygen ion conductivity of bismuth oxide compositions is orders of magnitude higher than that of YSZ at comparable temperatures.

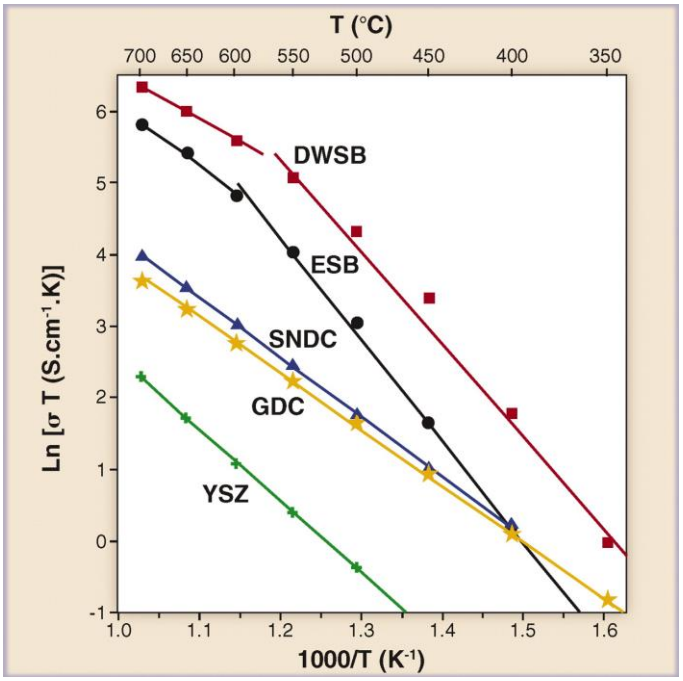


Figure 1-5 Comparison of ionic conductivity of different electrolyte materials [12]

Perovskite materials such as lanthanum gallate and its doped compositions have been extensively explored and suggested as an electrolyte material. In addition to electronic and ionic conductivity considerations for an electrolyte material, an appropriate candidate should have small TEC mismatch compared to adjacent electrode materials, exhibits no chemical reactivity with electrode or secondary electrolyte materials (during fabrication and operation), easy sinterability and gas tightness, and possesses sufficient mechanical strength. The primary focus of this work is to develop low-temperature SOFCs using ceria-based electrolytes and hence other electrolyte materials will not be discussed in more details.

1.4.3 Cathodes

Electrochemical reduction of oxygen occurs at the cathode side. Cathode and anode materials have essentially the same requirements. Candidate cathode materials should

have sufficient catalytic activity for oxygen molecule dissociation and reduction and have enough porosity for gas diffusion. Cathode materials should be compatible with the electrolyte in terms of both chemical reaction and TEC. Since the ORR occurs at the TPB, cathode material should have large TPB with high mixed electronic and ionic conductivity. ORR at the cathode side has a larger activation energy comparing to the anode reaction and thus cathodic overpotential particularly at lower temperatures dominates the non-ohmic losses and hence development of new cathode materials for intermediate and low-temperatures is actively pursued. Typically, perovskite oxides of formula ABO_3 where A is a rare-earth element (usually doped with alkaline earth cations) and B is a transition metal, are used as cathode materials. Doped lanthanum manganite compositions are the most common cathode materials. To enhance the electronic conductivity of lanthanum manganite, lanthanum is partially doped with an aliovalent cation such as (Sr^{2+}) $La(Sr)MnO_3$ (LSM). The difference between the valence of Sr^{2+} and La^{3+} and charge neutrality induces manganese to donate an electron and change its valence state from +3 to +4 and enhance the electronic conductivity through the small polaron hopping mechanism. LSM has low ionic conductivity and hence TPB length is normally extended by addition of an oxygen ion conductor phase such as YSZ into the cathode structure.

At lower temperatures, alternative materials such as $La(Sr)Co(Fe)O_3$ LSCF [17, 18] and $Sr(Sm)CoO_3$ (SSC), which exhibit both ionic and electronic conductivity are typically used. LSCF is chemically compatible with GDC and hence is used as the standard cathode material for GDC-based SOFCs [19, 20]. LSCF is a good electronic conductor (e.g. $La_{0.6}Sr_{0.4}Co_{0.2}Fe_{0.8}O_3$ - 300S/cm at 750 ºC) and also shows fast

oxygen surface exchange with higher oxygen ion conductivity than that of LSM (e.g. 10^{-3} S/cm at 750 ºC) [20].

Among this family, the Fe rich compositions are more attractive than Co rich compositions as they have lower thermal expansion coefficient and hence, better matched with ceria electrolytes [21]. $La_{0.6}Sr_{0.4}Co_{0.2}Fe_{0.8}O_3$ -$Ce_{1-x}Gd_xO_{2-\delta}$ composite cathodes have been studied by Dusastre et al. [19] and Murray et al. [20] and were found to be very effective in improving the performance over single phase $La_{0.6}Sr_{0.4}Co_{0.2}Fe_{0.8}O_3$ cathodes. Optimum composition was found to be between 30-50 wt% $Ce_{0.9}Gd_{0.1}O_{2-\delta}$ with area specific resistance (ASR) values of 0.33-0.6 $\Omega.cm^2$ at 600 ºC. Recently, Çelikbilek et al. [22] have studied the effect of sintering temperature on the microstructure and performance of the LSCF-GDC composite cathodes. By using electrostatic spray deposition, synthesis of a nano-structure, and lowering the sintering temperature to 800 ºC, they achieved the ASR of 0.13 $\Omega.cm^2$ at 600 ºC [22]. $Ba_{0.5}Sr_{0.5}Co_{0.8}Fe_{0.2}O_3$ (BSCF) based cathode was reported to exhibit low ASR due to its high catalytic activity and high oxygen diffusivity but BSCF shows fast degradation rates due to its low stability. In comparison, $Sm_{0.6}Sr_{0.4}CoO_3$ (SSC) showed reasonable high stability and catalytic activity. Ag-$(Bi_2O_3)_{0.75}(Er_{25}O_3)_{0.2}$ and Ag-BIMEVOX cermet cathodes have been also reported for low temperature applications [23, 24]. Other studied cathode materials are based on pyrochlore bismuth ruthenate [25-27], lead ruthenate and yttrium ruthenate mainly due to the catalytic activity of ruthenium oxide for oxygen reduction. Relative ratio of the electron to ion conducting phases, particle size ratio and spatial distribution to obtain percolation for both phases can significantly affect the performance of a composite cathode material.

1.5 Low-Temperature SOFCs

As mentioned earlier, yttria-stabilized zirconia (YSZ) is the state-of-the-art electrolyte material used in SOFCs operating in the temperature range of 800-1000 ºC. YSZ has negligible electronic conductivity and high chemical stability in both oxidizing and reducing atmospheres [28-33]. However, reasonable ionic conductivity and thus power density for YSZ based SOFCs is obtained only at high operating temperatures. Operation of the SOFCs at high temperatures requires expensive materials for different components of the stack and balance-of-plant. Additionally, thermal management of the stack and choice of components to minimize chemical reactivity between adjacent layers become critical at high operating temperatures. By reducing the operating temperature to low-temperature range (450-650 °C), cheap stainless-steel alloys can be implemented as interconnect materials and thus commercialization of the SOFCs technology can be accelerated. Additionally, lower operating temperature increases the lifetime of the stack, and shortens the start-up time of SOFCs which is critical for mobile applications [34-38]. However, the ionic conductivity and thus the power density of YSZ electrolyte based SOFCs decreases significantly at low temperatures. T wo approaches to compensate for lower conductivity at lower temperatures have been actively pursued: (a) decreasing the thickness of the electrolyte layer (oxygen ion conduction path), and (b) developing new electrolyte materials with higher conductivity and new electrode materials with better catalytic activity at lower temperatures. Alternative electrolytes based on doped ceria and stabilized bismuth oxide show significantly higher (more than an order of magnitude) conductivities than YSZ at low temperature and, hence, have received significant attention [39-41].

Unfortunately, as discussed previously, doped ceria has a narrow electrolytic region and in fuel atmosphere at the anode of a SOFC, doped ceria reduces from Ce^{4+} to Ce^{3+}, resulting in electronic conduction in the electrolyte by small-polaron hopping mechanism [42]. As mentioned earlier, such electronic leakage current reduces the ionic transference number of the electrolyte and results in lower cell voltage and power density. Yahiro et al. [43] demonstrated the concept of bilayer-electrolyte SOFC for the first time where a zirconia layer was used to block the leakage current through the GDC layer and showed improvement of the OCV for the bilayer cell comparing to single electrolyte GDC cell.

1.6 Ceria/Bismuth Oxide Bilayer Electrolyte SOFCs

Bilayer electrolytes based on doped ceria/stabilized bismuth oxide have been proposed as a measure to block the electronic leakage current in doped ceria and was first demonstrated by Wachsman et al. [37, 44-51]. Unfortunately, stabilized bismuth oxide decomposes into metallic bismuth at oxygen partial pressure (p_{O2}) levels below 10^{-13} atm. [52] and, hence, must be shielded by a secondary electrolyte layer against exposure to low p_{O2} side of the fuel cell. The primary advantage of ceria/bismuth oxide bilayer was that instead of using a less conductive YSZ electrolyte to protect the ceria-based electrolyte, a high conductive material (ESB) was used to block the electronic leakage current of ceria (Figure **1-6**). At the same time, the ceria layer increases the oxygen partial pressure at the interface providing stability to the bismuth oxide layer. As outlined by Wachsman et al. [14], relative thickness as well as the transport properties of the two layers have a key effect on the interfacial p_{O2} value and, therefore,

the electrochemical stability and any electronic leakage current of bilayer electrolyte based SOFCs. A bilayer electrolyte is schematically shown in Figure **1-6**. For fixed low and high Po_2 values at anode and cathode sides of the electrolyte, the relative thickness of each electrolyte layer can change the interfacial Po_2 and determine the thermodynamic stability of the bismuth oxide layer. A thorough review of the bilayer electrolyte SOFCs is given in chapter 2.

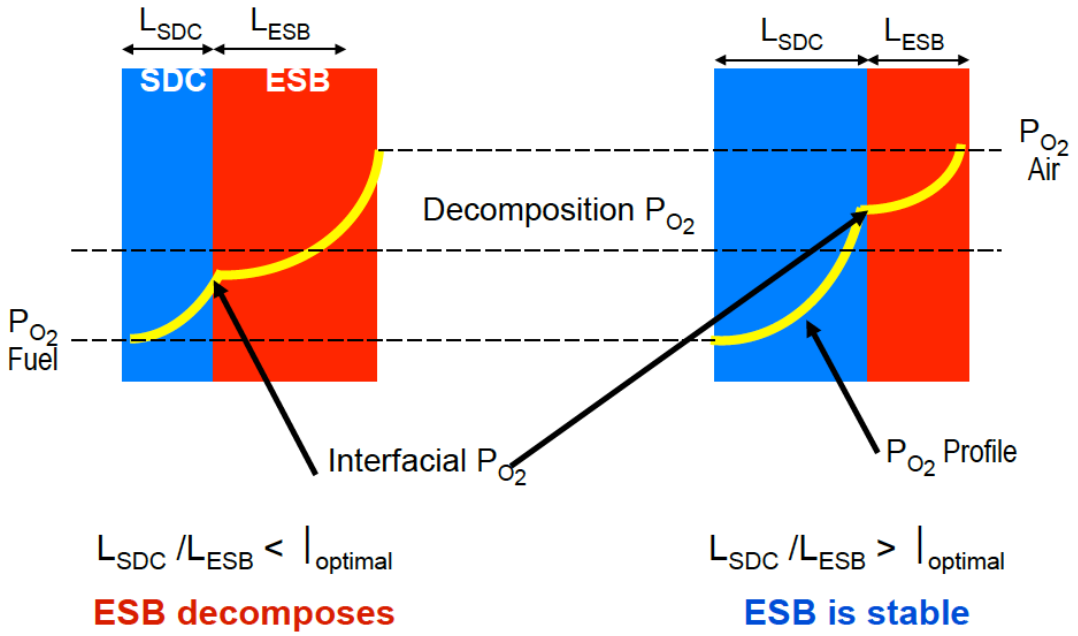


Figure 1-6 Schematic of effect of relative thickness of SDC/ESB bilayer on interfacial oxygen partial pressure (pO2) and ESB stability [14]

1.7 Objectives

1.7.1 Alternative Bismuth Oxide Compositions

Pure δ-Bi_2O_3 has the highest oxygen ion conductivity among all oxygen ion conductors [53]. Such high conductivity is due to the high concentration of intrinsic oxygen vacant sites (25%). However, below 730 ºC due to the phase transformation into the monoclinic phase, a discontinuous drop of conductivity happens. All lanthanide

dopants with radii between Yb^{3+} and Dy^{3+} stabilize bismuth oxide in cubic fluorite structure. The unit cell of cubic bismuth oxide consists of four cations in the FCC positions and six anions in the eight tetrahedral positions and 2 oxygen vacancy sites. The unit cell of the cubic bismuth oxide is shown in Figure **1-7**.

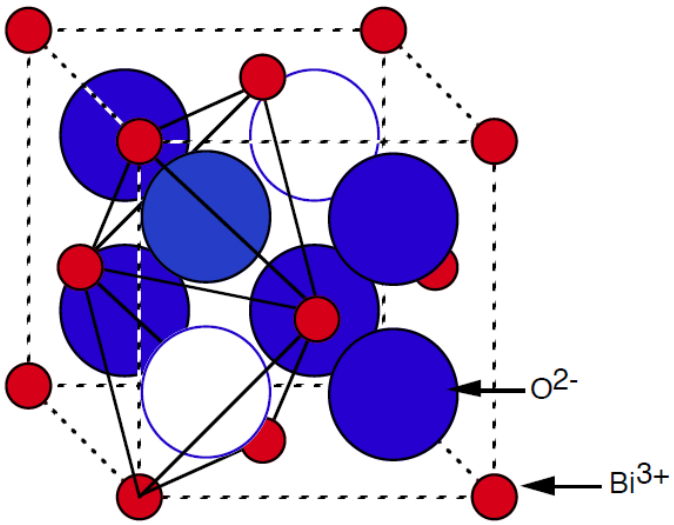


Figure 1-7 Unit cell of cubic fluorite Bi_2O_3

As will be discussed in the literature review section, majority of ceria/bismuth oxide bilayer SOFCs use cubic fluorite bismuth oxide compositions such as ESB, YSB and DWSB. Such cubic structures although initially show high ionic conductivity, they suffer from disorder-order transition and their conductivity decay below 600 ºC. Such conductivity decays have been attributed to the displacement of the oxygen ions from the center of cation tetrahedra (8c-sites) to the faces of the cation tetrahedra (32f-sites) in <111> direction which limits the mobility of oxygen ion vacancies resulting in conductivity decay as isothermally annealed under 600 ºC [53, 54]. Since these bismuth oxide compositions are normally used as both the electrolyte material and oxygen ion conductor phase in the cathode composition, conductivity decay can increase the ohmic

and non-ohmic ASR of the cell and results in major power density degradation. The primary objective of this proposal is to implement and evaluate the new bismuth oxide compositions as: (a) bilayer electrolyte material for GDC/stabilized bismuth oxide, and (b) oxygen ion conductor phase in the cathode for LT-SOFCs. The following two bismuth oxide compositions will be primarily investigated:

Rhombohedral bismuth oxide: Our group has been working on the development of several compositions of bismuth oxides stabilized with single dopant or multiple dopants for low temperature SOFCs. Neodymium-gadolinium stabilized bismuth oxide, 4Nd4GdSB (NGSB) is a newly developed double-doped bismuth oxide electrolyte for low temperature SOFCs. NGSB exists in the rhombohedral phase and shows stable ionic conductivity at ~500°C. Moreover, compared to bilayer SOFCs based on gadolinium doped ceria (GDC) and ESB, GDC/NGSB bilayer SOFCs have showed promising initial electrochemical results and hence has been studied in more details. The stability of NGSB conductivity with time is shown in **Figure 1-8**.

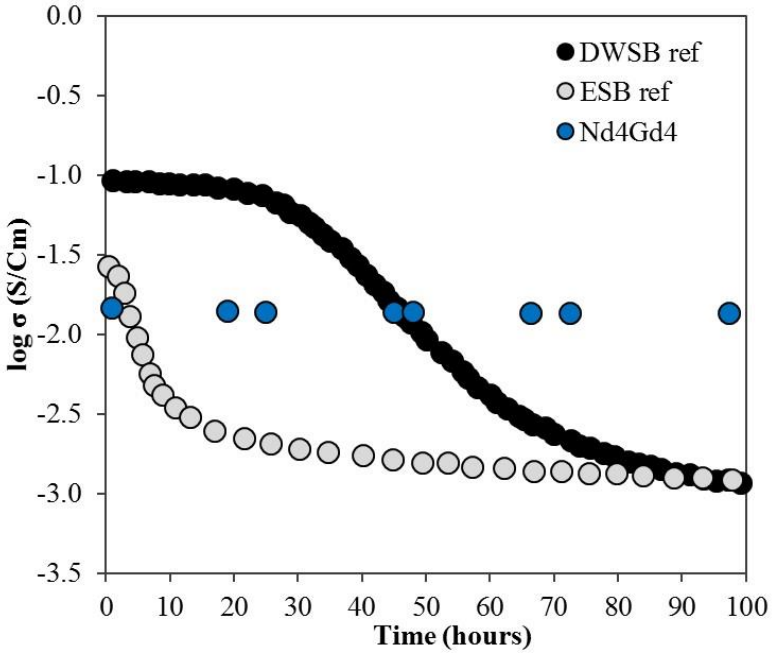


Figure 1-8 Conductivity stability of NGSB, ESB, and DWSB [55]

Cubic bismuth oxide: Huang et al. [56] have developed a cubic bismuth oxide with negligible conductivity decay in the temperature range of 500-600 ℃. Conductivity of $(Bi_{0.75}Y_{0.25})_{0.93}Ce_{0.07}O_{1.5\pm\delta}$ (YCSB) at 500, 600, and 650 ºC are shown in **Figure 1-9**. YCSB has been reported to not suffer from oxygen-ion ordering at low temperatures and, hence, application of YCSB as both bilayer electrolyte as well as cathode oxygen ion conductor is proposed in this work.

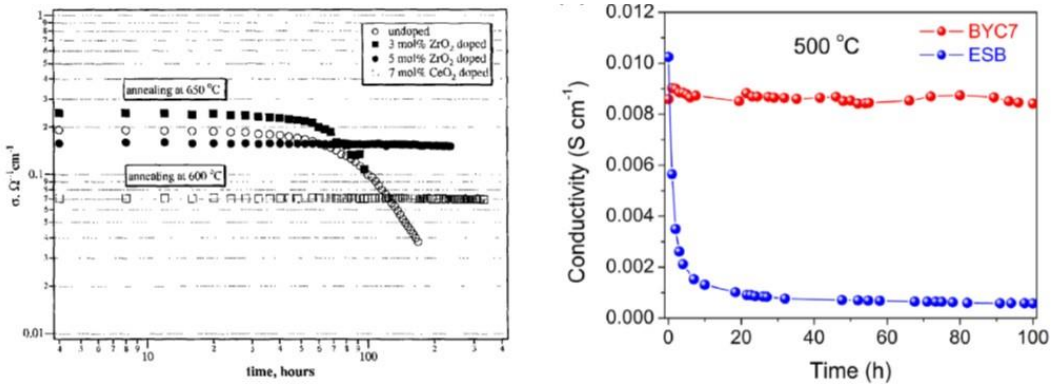


Figure 1-9 Conductivity stability of YCSB (BYC7) at 650, 600, and 500 ºC [56, 57]

1.7.2 Effect of Thickness Ratio

As schematically shown in Figure 1-6, ceria/bismuth oxide thickness ratio impacts the interfacial p_{O2} value and hence can affect the OCV of the cell. Additionally, due to the difference between the ionic conductivity of doped ceria and bismuth oxide, varying the thickness ratio results in different ohmic ASR values across the bilayer electrolyte. Hence, a proper thickness ratio that balances between high OCV and low ohmic ASR and maximizes the power density of the cell must be identified. Until now, effect of ceria/bismuth oxide thickness ratio on the performance of anode-supported ceria/bismuth oxide bilayer electrolyte SOFCs has not been explored nor reported in literature.

1.7.3 Development of ceria/bismuth oxide bilayer electrolyte high-performance LT-SOFCs with nanostructured electrodes

Finally, using the alternative bismuth oxide composition with stable ionic conductivity at temperatures below 600 ℃, as identified in section 1.7.1 and a proper electrolyte thickness and thickness ratio as suggested by the results of section 1.7.2, a high-performance anode-supported ceria/bismuth oxide bilayer electrolyte SOFC will be developed. To further enhance the power density of the cell in the temperature range of 600-500 ℃, nanostructured electrodes, synthesized through low-temperature deposition of nano-particles on the backbone of the composite anode and cathode (infiltration), will be explored.

2 Bilayer Electrolyte SOFCs-Literature Review

The earliest demonstration of a bilayer electrolyte SOFC dates back to 1988 when Yahiro et al. [43] showed the potential of using an electron blocking layer (zirconia) at the anode side of a ceria based electrolyte to enhance the open circuit voltage (OCV) of the cell. Although the primary focus of their work was to evaluate the conductivity of various ceria based electrolytes and the effect of cathode on the cell performance, they found that coating the ceria electrolyte on the anode side with a thin layer of zirconia deposited by RF-sputtering significantly improved OCV as shown in **Figure 2-1** I-V characteristics of monolayer GDC cell at 600 (closed circle) and 700 (open circle) °C and YSZ/GDC bilayer electrolyte cell at 600 (closed triangle) and 700 (open triangle) °C [43], resulting in 33% higher power density. Following that, many scholars implemented the same approach to empower the concept of replacing the less-conductive zirconia-based electrolyte with the more-conductive ceria-based electrolytes and lowering the operating temperature of the cell. The initial structural design of SOFCs was constrained to electrolyte- supported cells. Such cells suffered from large ohmic losses across the electrolyte layer and thus did not show reasonable power density output. With the advent of sophisticated thick and thin film fabrication methods such as tape casting and pulsed laser deposition (PLD) respectively, thickness of the electrolyte was significantly reduced, which resulted in much smaller ohmic losses and higher power density output. In this work electrolyte supported SOFCs will be reviewed briefly. However, electrode-supported SOFCs will be discussed in more detail.

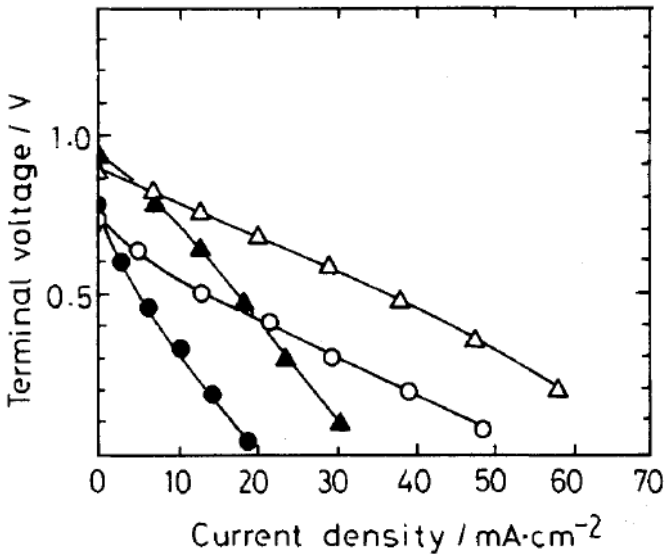


Figure 2-1 I-V characteristics of monolayer GDC cell at 600 (closed circle) and 700 (open circle) °C and YSZ/GDC bilayer electrolyte cell at 600 (closed triangle) and 700 (open triangle) °C [43]

2.1 Electrolyte-supported SOFCs

2.1.1 2.1.1. Zirconia/Ceria Bilayer IT-SOFCs

The results of Yahiro [43] spurred several research activities based on zirconia/ceria bilayer electrolytes for application in IT-SOFCs. There were two key considerations for the development work – Firstly, design of the zirconia/ceria bilayer whether the ceria layer should be on the anode side or on the cathode side and the minimum thicknesses of the zirconia layer to block electronic conduction in the ceria layer. Ceria on the cathode side allows the possibility of using cobalt containing cathodes (LSC, LSCF, SSC, BSCF), with higher performance at lower temperatures compared to LSM, which tend to react with zirconia. Secondly, fabrication of the bilayer to match shrinkage rates of zirconia and ceria layers and to avoid formation of resistive secondary phases at the interface during sintering.

Lim and Virkar [58] measured the chemical potential of oxygen in YSZ/GDC bilayer electrolyte SOFCs and found that the position of YSZ layer, whether on the anode side or the cathode side, affected the chemical potential profile and the cell performance. Thickness of GDC and YSZ electrolyte was 45 and 5 μm, respectively, and the electric potential inside the GDC electrolyte was measured using Pt embedded electrodes. LSM-YSZ and LSC-GDC were used as the cathode for the bilayer cell with GDC at the anode side and the cathode side, respectively. The embedded probe measurements indicated that with GDC at the cathode, electric potential inside the GDC was a function of position and load; oxygen partial pressure at the GDC/cathode interface showed a small change (Figure **2-2**). However, with GDC at the anode, electric potential inside the GDC was independent of position and load and a sharp change in oxygen partial pressure was observed at the YSZ/cathode interface. In terms of performance, the cell with GDC at the anode showed >3 times higher MPD than the cell with GDC at the cathode (0.52 vs. 0.14 W/cm^2 at 650 °C). However, a majority of the work that followed focused on zirconia/ceria bilayer electrolytes with ceria on the cathode side as it allowed use of cobalt containing cathodes which improve performance at lower temperatures. In another work, Kwon et al. [59] suggested that YSZ/GDC thickness ratio of about 2×10^{-7} is sufficient to block the electronic leakage current in GDC electrolyte. However, fabrication limitation prevents the development of bilayers with such ultra-thin YSZ layer. Cell configuration, processing, and performance of zirconia/ceria bilayer based IT-SOFCs is summarized in Table **2-1**.

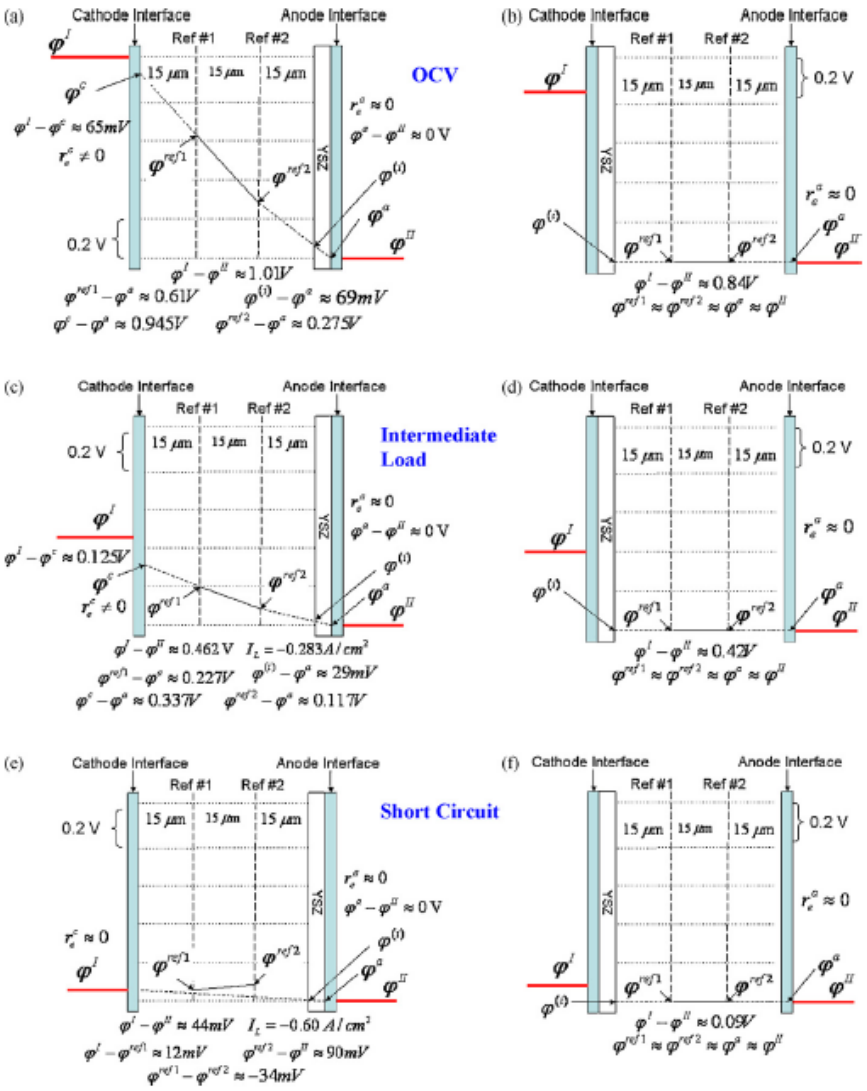


Fig. 6. Plots of the measured φ in the cathode/GDC/YSZ/anode cell under open circuit (a), under intermediate load (c), and under short circuit condition (e). Plots of the measured φ in the cathode/YSZ/GDC/anode cell under open circuit (b), under intermediate load (d), and under short circuit condition (f).

Figure 2-2 Plots of measured electrochemical potential (φ) in Ni-YSZ/YSZ/GDC/LSC-GDC cell under open circuit (a), under intermediate load (c), and under short circuit condition (e). Plots of measured electrochemical potential (φ) in Ni-GDC/GDC/YSZ/LSM-YSZ cell under open circuit (b), under intermediate load (d), and under short circuit condition (f).[58]

Electrolyte supported YSZ/YDC bilayer electrolyte cell was developed by Kim et al.[60] using a thick 1.6 mm YDC pellet made by sintering of co-precipitated powders at 1600 °C. YSZ layer was deposited by spin coating and sintered at 1400 °C. Compared to monolayer YDC cell, YSZ/YDC bilayer cell increased OCV slightly by

0.05 V between 700-1050 °C. However, MPD of YSZ/YDC bilayer cell at 800 °C (0.12 W/cm^2) was comparable to that of monolayer YSZ cell at 1000 °C (0.14 W/cm^2) due to the higher conductivity of YDC. Based on the model developed by Virkar [61], p_{O2} at YSZ/YDC interface was estimated to be two orders of magnitude higher than the stability limit of ceria at 800 °C.

Hsieh et al. [62] fabricated and tested electrolyte supported micro-tubular SOFCs based on ScSZ/GDC bilayer electrolyte. GDC micro-tubes were extruded and pre-sintered at 1100 °C. NiO-GDC anode (60:40) and LSCF-GDC cathode (80:20) were deposited on the inner surface and outer surface of micro-tubes and sintered at 1400 °C and 1100 °C, respectively. For the bilayer cell, ScSZ was deposited prior to the anode deposition and sintered at 1400 °C. Thickness of the sintered ScSZ and GDC was 8 and 285 μm, respectively. ScSZ layer in the bilayer cell significantly improved OCV from 0.92 to 1.06 V at 650 °C by blocking the electronic conduction in GDC, but decreased MPD from 0.20 to 0.16 W/cm^2 due to high interfacial resistance across ScSZ/GDC and anode/ScSZ interfaces. At 800 °C, the bilayer cell showed better performance compared to the monolayer GDC cell and MPD of the cell increased from 0.36 W/cm^2 to 0.42 W/cm^2.

Table 2-1 Cell configuration, processing, and performance of zirconia/ceria bilayer based IT and HT-SOFCs

Bilayer Electrolyte[1]	**Anode/Cathode**	**Processing**[2]	**OCV, MPD 550 °C**	**OCV, MPD 650 °C**	**OCV, MPD 800 °C**	**Reference**
YSZ (2 μm)/YDC (1.6 mm)	Pt/Pt	SP/SLC/SLC/SP			0.85 V, 0.12 W/cm^2	[60]
ScSZ (8 μm)/GDC (285 μm)	Ni-GDC/LSCF-GDC	SLC/SLC/EX/SLC		1.06 V, 0.16 W/cm^2	0.98 V, 0.42 W/cm^2	[62]
YSZ (3 μm)/GDC (7 μm)	Ni-YSZ/LSCF-GDC	PP/SPC/SPC/SP			1.05 V, 0.68 W/cm^2	[63]
YSZ (8 μm)/SDC (12 μm)	Ni-YSZ/BSCF	PP/SP/SP/SP		1.10 V	1.06 V	[64]
ScSZ (2 μm)/SDC (4 μm)	Ni-SSZ/SSC	TC-SP/SP/SP/SP	1.04 V, 0.13 W/cm^2	1.03 V, 0.55 W/cm^2	0.99 V, 1.80 W/cm^2	[65]
ScSZ (6-7 μm)/SDC (6-7 μm)	Ni-SDC/SSC	TC-SP/PLD/PLD/SP	1.05 V, 0.51 W/cm^2	1.04 V, 1.38 W/cm^2		[66]
YSZ (4 μm)/GDC (1.5 μm)	Ni-YSZ/LSCF-GDC	TC/MS/MS/SP			1.12 V, 1.25 W/cm^2	[67]
YSZ (0.7 μm)/SDC (5 μm)	Ni-YSZ/LSCF	TC/PLD/PLD/SP		0.95 V, 1.37 W/cm^2		[68]
YSZ (2 μm)/SDC (6 μm)	Ni-YSZ/SSC-SDC	PP-SLC/PLD/PLD/SP	1.03 V, 0.42 W/cm^2	1.01 V, 0.90 W/cm^2		[69]
YSZ (0 - 0.2 μm)/GDC (1 μm)	Ni-YSZ/LSC	PLD-TC/PLD/PLD/ PLD		1.08 V, 1.13 W/cm^2 (600 °C)		[70]
YSZ (0.1 μm)/GDC (0.1 μm)	Ni-YSZ/LSCF-GDC	PP-SP/SLC/CSD/CSD	1.01 V, 0.71 W/cm^2	1.00 V, 1.35 W/cm^2		[71]
ScSZ (2 μm)/SDC (20 μm)	Ni-SDC/SSC-SDC	SLC/PLD/PLD/SP	1.00 V, 0.14 W/cm^2			[72]
GDC (4 μm)/ScCeSZ (7 μm)/ GDC (4 μm)	Ni-GDC/LSCF	SP/TC/TC/TC/SP	1.20 V	1.15 V, 0.19 W/cm^2		[73]

[1]Anode/Electrolyte-1/Electrolyte-2/Cathode

[2]PP – Powder Pressing, SPC – Spray Coating, SLC – Slurry Based Coating, SP – Screen Printing (or similar), TC – Tape Casting, DCS – DC Sputtering, EX – Extrusion, PLD – Pulse Laser Deposition, MS – Magnetron Sputtering, CSD – Chemical Solution Deposition

Electrolyte supported YSZ/GDC bilayer electrolyte SOFCs with ultra-thin (28-150 nm) YSZ film was fabricated by Jee et al. [74] using atomic layer deposition (ALD). Thick 0.43 mm GDC electrolyte support was fabricated by pressing and sintering and ultra-thin YSZ film was deposited by ALD at 230 °C. NiO-GDC anode and LSCF-GDC cathode was sintered at 1200 °C and 1400 °C, respectively. High sintering temperatures resulted in significant inter-diffusion of cerium into YSZ layer as observed by XPS. Furthermore, morphological changes in the YSZ thin film were observed – YSZ grains coalesced at GDC grain boundaries, uncovering the underlying GDC layer. In electrochemical test with H_2 as fuel, OCV was found to be stable only for YSZ/GDC bilayer SOFCs with 150 nm YSZ protection layer, suggesting that ultra-thin YSZ protective layer may not be practically feasible.

An electrolyte supported GDC/YSZ/GDC trilayer electrolyte based SOFCs was developed by Timurkutluk et al. to suppress the leakage current between anode and cathode [73]. A thin layer of doped zirconia (YSZ, ScSZ, ScCeSZ) was laminated between two thick GDC layers made by tape casting. NiO-GDC (60:40) anode and LSCF-GDC (50:50) were then screen printed. Doped zirconia layer improved OCV of the trilayer cells at 550-650 °C but MPD was found to be lower than that of monolayer GDC cell due to higher resistance. At 650 °C, MPD of the monolayer GDC cell was ~0.25 W/cm^2, while trilyaer cell with ScCeSZ showed ~25% lower MPD (0.19 W/cm^2). In another study, Wu et al.[75] measured the conductivity of YSZ/SDC bilayer consisting of a thin 250 nm YSZ film deposited on SDC substrate by electron-beam evaporation at 200 ° C. YSZ/SDC bilayer samples were sintered at 1000 °C and showed lower conductivity than single crystal YSZ, as presented in Figure **2-3**. TEM-EDS

analysis indicated formation of a solid solution layer at the YSZ/SDC interface due to interdiffusion of cerium and zirconium resulting in lower ionic conductivity **(Figure 2-4**).

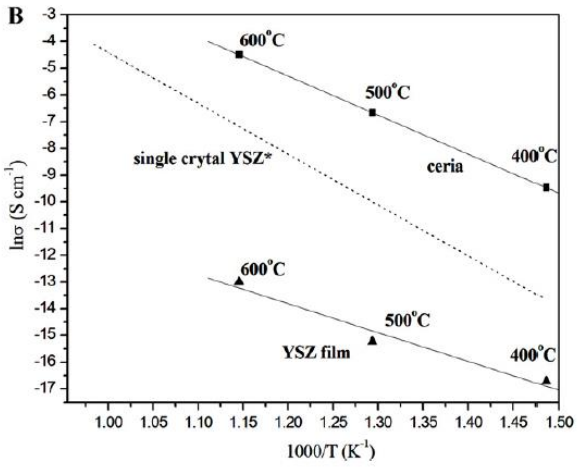


Figure 2-3 Conductivity of SDC, YSZ/SDC bilayer (YSZ film) and single crystal YSZ samples [75]

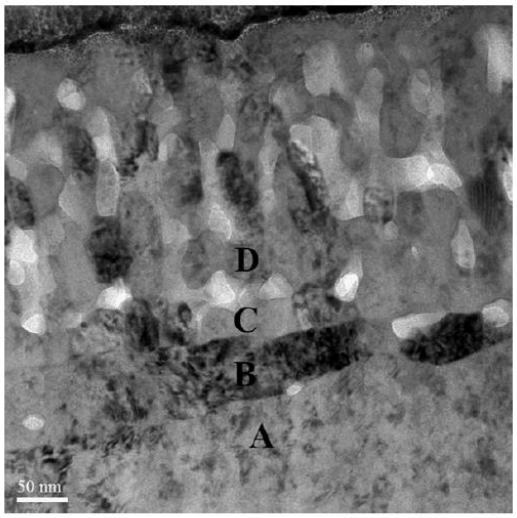


Figure 2-4 Bright field image of YSZ/SDC sample for EDS elemental analysis. [75]

2.1.2 Ceria/bismuth oxide bilayer IT-SOFCs

Ceria/bismuth oxide bilayer electrolyte based SOFCs was first proposed by Wachsman et. al. to combine two low-temperature high-conductivity electrolytes, which cannot operate efficiently as a single electrolyte in SOFC environment [14]. With ceria on the

anode side and bismuth oxide on the cathode side, a functional bilayer electrolyte based SOFCs was demonstrated. It was suggested that the partial electronic conduction in ceria layer could be blocked by the bismuth oxide layer, while the ceria layer increased the oxygen partial pressure at the interface above the decomposition potential of bismuth oxide. Practical devices required development of cathodes compatible with stabilized bismuth oxide as platinum and conventional LSCF cathode for IT-SOFCs show significant reactivity with bismuth oxide. This resulted in the development of new alternative cathodes such as bismuth ruthenate-ESB [76, 77] and LSM-ESB [78] composites for low temperature operation. Initial concept demonstration of ceria/bismuth oxide bilayer cells was done with electrolyte supported cells using noble metal (gold, silver) electrodes which was then followed with development of anode supported cells with thick/thin film bilayer electrolyte showing high performance at low temperatures. Low temperature operation of SOFCs allows the possibility to use stable nanostrucutured electrodes (without undue sintering during operation) with higher surface area-to-volume ratio and higher catalytic activity. By shifting the effective particle diameter of the catalytic phase from the micro (10^{-6}) to the nano (10^{-9}) regime, TPB density [$(10^{-6}/10^{-9})^3 = 10^9$] is dramatically increased and can be used to compensate for the exponentially decreasing area-specific electrode reaction rates (activation polarization) with decreasing temperature [79]. Some of these advances have been employed to improve the performance of bilayer electrolyte SOFCs. Recent work on ceria/bismuth oxide bilayer has focused on utilizing new bismuth oxide compositions such as double-doped cubic bismuth oxides (DWSB, DGSB) with high oxygen ion conductivity. Cell configuration, processing, and

performance of ceria/bismuth oxide bilayer based LT-SOFCs is summarized in Table **2-2**.

Wachsman et al [14] [45] used different stabilized bismuth oxides (5-60 μm [45]), including $(Y_2O_3)_{0.2}(Bi_2O_3)_{0.8}$ and $(Er_2O_3)_{0.2}(Bi_2O_3)_{0.8}$, to block the electronic transport across thick self-supporting pellets (~ 0.8-1 mm) of doped ceria – $(CeO_2)_{0.9}(MO_{1.5})_{0.1}$ where M is Y, Sm and Gd. The samples were coated with Au and Pt paste on the cathode and anode side, respectively, and tested with humidified H_2 and O_2 as fuel and oxidant, respectively. The results of the experiments indicated that all bilayer cells have higher OCV compared to the cell with the single layer ceria cell of the same composition. The higher OCV of the bilayer cells was suggested to be due to the electron blocking capability of the bismuth oxide layer, which was stable due to high interfacial p_{O2} provided by the ceria layer. SDC cells (both monolayer and bilayer electrolyte) showed higher OCV compared to YDC cells at all temperatures, due to the higher transference number (t_i) of SDC compared to YDC. For the SDC/ESB bilayer cell, increasing the density of the ESB layer increased the OCV and at 500 °C, OCV was higher by 90-160 mV depending on temperature compared to the monolayer SDC cell [45]. The effect of ESB thickness on the performance of bilayer electrolyte cells was studied using GDC electrolyte and it was found that thick ESB resulted in lower OCV compared to thin ESB, possibly due to the lower interfacial p_{O2} in the case of thick ESB cell (**Figure 2-5**). The SDC/ESB cell was operated under open circuit condition for 1,400 hours and was found to be stable. Moreover, it was found that the addition of ESB not only increased the OCV but also decreased the cell area specific resistance (ASR), resulting in 33% higher power density for SDC/ESB bilayer cell [45].

This result favorably compared ceria/bismuth oxide bilayer to zirconia/ceria bilayer in which resistive secondary phases form leading to higher resistance and lower performance [75].

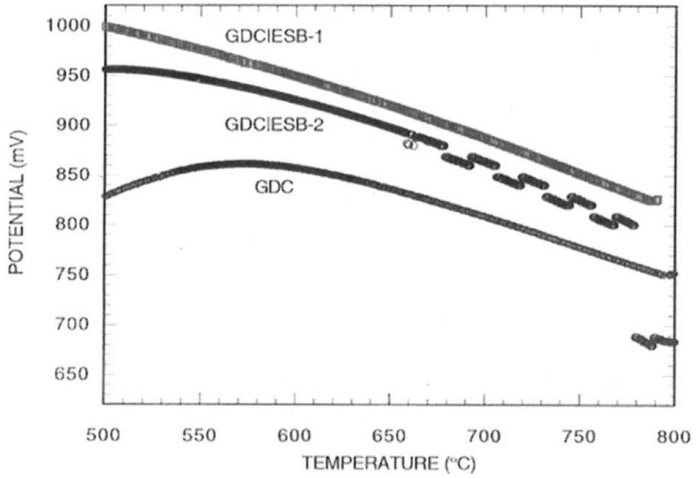


Figure 2-5 OCV as a function of temperature for GDC and GDC/ESB electrolytes. Thickness of ESB layer for GDC/ESB-2 is six times that of GDC/ESB-1 [14]

Table 2-2 Cell configuration, processing, and performance of ceria/bismuth oxide bilayer based LT and IT-SOFCs

Bilayer Electrolyte[1]	**Anode/Cathode**	**Processing**[2]	**OCV, MPD 450 °C**	**OCV, MPD 550 °C**	**OCV, MPD 650 °C**	**Reference**
Electrolyte-Supported						
SDC (800 μm)/ESB (5-60 μm)	Pt/Au	SP/PP/SP/SP		0.92 V	0.87 V	[14]
SDC (1 mm)/ESB (30 μm)	Pt/Au	SP/PP/SLC/SP		0.98 V	0.96 V	[44]
Electrode-Supported						
GDC (10 μm)/ESB (4 μm)	Ni-GDC/BRO-ESB	TC/SPC/PLD/SP			0.77 V, 1.95 W/cm^2	[80]
GDC (10 μm)/ESB (5 μm)	Ni-GDC/BRO-ESB	TC/SPC/SLC/SP		0.85 V	0.78 V, 1.47 W/cm^2	[48]
GDC (25 μm)/ESB (2 μm)	Ni-GDC/LSM-ESB	TC/SPC/SLC/SP	0.87 V, 0.09 W/cm^2	0.80 V, 0.34 W/cm^2	0.73 V, 1.01 W/cm^2	[81]
SDC (26 μm)/YSB (6 μm)	Ni-SDC/LSM-YSB	PP/PP/DCS/SP		0.86 V, 0.15 W/cm^2	0.85 V, 0.38 W/cm^2	[46]
GDC (20 μm)/YDB (10 μm)	Ni-GDC/LSM-YDB	PP/SLC/SP/SP		1.00 V, 0.28 W/cm^2	0.89 V, 0.53 W/cm^2	[82]
SNDC (20 μm)/ESB (20 μm)	Ni-SNDC/LBSM-ESB	PP/PP/SLC/SP	0.97 V, 0.13 W/cm^2	0.90 V, 0.52 W/cm^2	0.80 V, 0.98 W/cm^2	[50]
SNDC (22 μm)/ESB (20 μm)	Ni-SNDC/PBM-ESB	PP/PP/SLC/SP	0.97 V, 0.10 W/cm^2	0.91 V, 0.48 W/cm^2	0.80 V, 0.99 W/cm^2	[83]
GDC (20 μm)/DGSB (3-5 μm)	Ni-GDC/LSM-ESB	TC/TC/SP/SP			0.80 V, 1.31 W/cm^2	[84]
GDC (23-70 μm)/xSB (0-25 μm)	Ni-GDC/LSM-ESB	TC/TC/SP/SP		0.84 V, 0.31 W/cm^2	0.85 V, 1.06 W/cm^2	[85]

[1]Anode/Electrolyte-1/Electrolyte-2/Cathode

[2]PP – Powder Pressing, SPC – Spray/Spin Coating, SLC – Slurry Based Coating, SP – Screen Printing (or similar), TC – Tape Casting, DCS – DC Sputtering

Following the initial promising results with ceria/bismuth oxide bilayer cells, Park et al. [37] fabricated and studied the electrical conductivity of SDC/ESB bilayer electrolyte. SDC powder was produced by conventional solid state reaction and pressed into ~2 mm thick pellets. ESB layer was made by two methods – a) PLD for thin film and b) dip coating for thick film. For PLD target, ESB powder was made by solid state route, while for dip-coating, ESB powder was fabricated by citrate process. ESB powder made by citrate process required lower calcination temperature (650 °C) compared to the solid state route (800 °C) and enabled densification of the dip-coated film. Thickness of the ESB layer was controlled by the deposition time and solid loading of the slurry for PLD and dip-coating method, respectively. XRD pattern of SDC/ESB bilayer showed only peaks from SDC and ESB phases and no other secondary phase was identified. Absence of reaction between SDC and ESB was also confirmed through EDX scans across the bilayer interface. Conductivity measurements showed that SDC/ESB bilayer electrolyte has a slightly higher conductivity comparing to SDC monolayer electrolyte, which was likely due to the formation of more conductive solid solution phase at the SDC-ESB interface. Further analysis as shown in Figure 2-5 indicated that the grain boundary conductivity of SDC/ESB bilayer electrolyte was higher than SDC monolayer electrolyte, which was attributed to the scavenging effect of bismuth oxide for silica-rich impurities at the grain boundaries in SDC resulting in a lower activation energy for oxygen transport through the bilayer electrolyte.

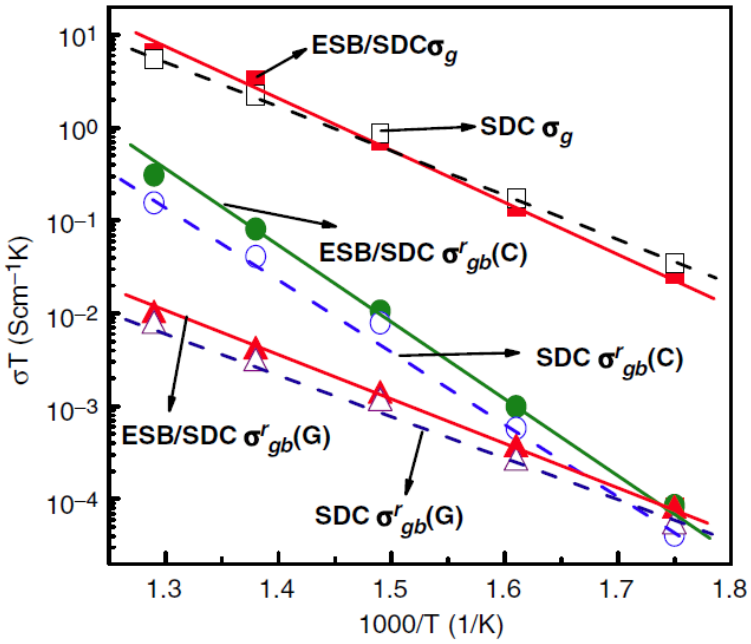


Figure 2-6 Grain conductivities of ESB/SDC and SDC and grain boundary conductivies of ESB/SDC and SDC by geometric method (G) and capacitance method (C)[37]

In another study, Park and Wachsman [44] looked at the effect of relative thickness of bilayer electrolyte layers and anode oxygen partial pressure (p_{O2}) on OCV and t_i of SDC/ESB bilayer SOFCs at 600-800 °C. Thin ESB layer (1.5 μm) was made by PLD and thick ESB (9-30 μm) layer was made by dip-coating in ESB suspension. At high anode p_{O2} levels, t_i of SDC monolayer electrolyte and ESB/SDC bilayer electrolyte was almost identical. However, as the anode p_{O2} was decreased, the bilayer electrolyte showed a higher t_i compared to SDC monolayer electrolyte and the increase in t_i with bilayer electrolyte was more pronounced at higher temperatures. The effect of relative thickness of the two layers was also examined and it was found that t_i and OCV increased with increase in the relative thickness of ESB/SDC, showing a sigmoidal (s-shaped) relationship. t_i of bilayer electrolyte reached ~0.9 at ESB/SDC relative thickness of 0.03. Performance of Au and Ag-ESB cathode was also studied and it was found that Ag-ESB cathode has a lower overpotential resulting in a higher OCV. In

another study [38], Park et al. looked at the application of SDC/ESB bilayer electrolytes for ceramic oxygen generators.

2.2 Electrode-supported Bilayer Cells

2.2.1 Zirconia/ceria bilayer IT-SOFCs

2.2.1.1 Bilayer cells with zirconia at the anode side

Results with electrolyte supported zirconia/ceria bilayer electrolyte cells were not promising in terms of power density which led researchers to evaluate anode supported configuration using both thick and thin film processing for fabrication of zirconia and ceria layers. Some studies with cathode supported and metal supported configuration have also been reported but the performance was found to be lower compared to anode supported cells.

To understand the effect of zirconia/ceria bilayer on ionic conductivity of the electrolyte, Brahim et al.[86] measured the conductivity of YSZ/GDC bilayer deposited by DC magnetron sputtering on LSM cathode. Five bilayer samples with different thickness ratios of YSZ and GDC layers were studied. The results of impedance spectroscopy studies showed that the bilayer electrolyte resistance increased with increase in thickness of both YSZ and GDC layers and, as expected, the effect of YSZ thickness on bilayer resistance was more pronounced. Overall, the effect of thickness ratio was found to be more important than the electrolyte thickness and the bilayer sample with YSZ:GDC thickness ratio of 1:2.2 showed lower conductivity than all other samples with ratio of 1:5 or lower but with higher thicknesses.

Liu et al. fabricated Ni-YSZ anode supported YSZ/GDC bilayer SOFCs with LSCF-GDC composite cathode. Ni-YSZ cermet anode was made by powder pressing and pre-sintering at 900 ^{o}C. Spray coating was used to deposit YSZ and GDC layers of 3 and 7 μm thickness, respectively. OCV of the bilayer cell was 1.05 V at 800 °C, significantly higher than that of 10 μm monolayer GDC cell (0.59 V) as shown in **Figure 2-7**; suggesting that YSZ layer significantly suppressed the electronic leakage in GDC. However, MPD of the bilayer cell was low (0.68 W/cm^2 at 800 °C), which was attributed to gas diffusion limitation inside Ni-YSZ anode. [63]

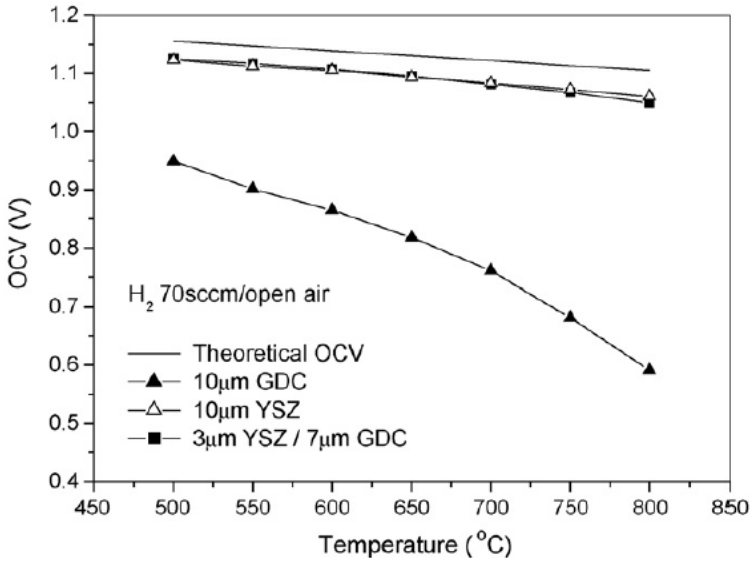


Figure 2-7 Theoretical and measured OCV of monolayer GDC(10 μm) cell, monolayer YSZ(10 μm) cell, and bilayer YSZ(3 μm)/GDC(7 μm) cell [63]

Wang et al. fabricated and tested YSZ/GDC bilayer electrolyte SOFCs using BSCF ($Ba_{0.5}Sr_{0.5}Co_{0.8}Fe_{0.2}O_3$) cathode [64]. NiO-YSZ (50:50) anode substrate was prepared by pressing and pre-sintering at 1000 °C. YSZ layer was screen-printed and sintered at 1400 ^{o}C, followed by screen-printing and sintering at 1400 ^{o}C of SDC layer. Thickness of YSZ and SDC layers was 2-8 and 12 μm, respectively. Reaction between YSZ and

SDC layers after sintering at 1400 ºC was confirmed by shift in XRD peak positions and EDX showed significant diffusion of cerium and samarium into YSZ layer. Moreover, conductivity of YSZ/SDC pellet was found to be 7 times lower than of SDC pellet. At 750 °C, OCV of a bilayer cell with 2 μm thick YSZ was 0.88 V while cells with 5-8 μm thick YSZ showed ~1.05 V, suggesting that YSZ layer below 5 μm may not be able to completely block SDC leakage current at higher temperatures. MPD of bilayer cell with 5 μm YSZ was 0.82 W/cm^2 at 750 °C, but after only two thermal cycles non-ohmic ASR increased resulting in 35% lower MPD.

Zhang et al. [65] used tape casting to fabricate thin ScSZ/SDC bilayer electrolyte SOFCs. NiO-YSZ support was fabricated by tape-casting followed by screen-printing of NiO-SSZ (56:44) active anode layer. Thickness of ScSZ and SDC electrolyte layers after co-firing at 1400 °C was 2 and 4 μm thickness, respectively. As shown in Figure **2-8**, OCV of the bilayer cell was 1.03 V at 650 °C indicating that ScSZ layer successfully blocked the electronic leakage current in SDC layer. MPD of ScSZ/SDC bilayer cell was 0.54 and 1.8 W/cm^2 at 650 and 800 °C, respectively. Further analysis suggested that 1 μm thick interdiffusion layer at ScSZ/SDC interface accounted for more than 90% of the electrolyte ohmic ASR, as the conductivity of the interfacial layer was 2-3 times lower than ScSZ and 1-2 orders of magnitude lower than SDC. Long term stability studies showed that MPD decreased with time largely due to increase in non-ohmic ASR at an approximately constant rate, following an initial 6-7 hours decrease. It was suggested that cathode performance degraded over time due to coarsening of cathode microstructure and diffusion of strontium away from SSC cathode.

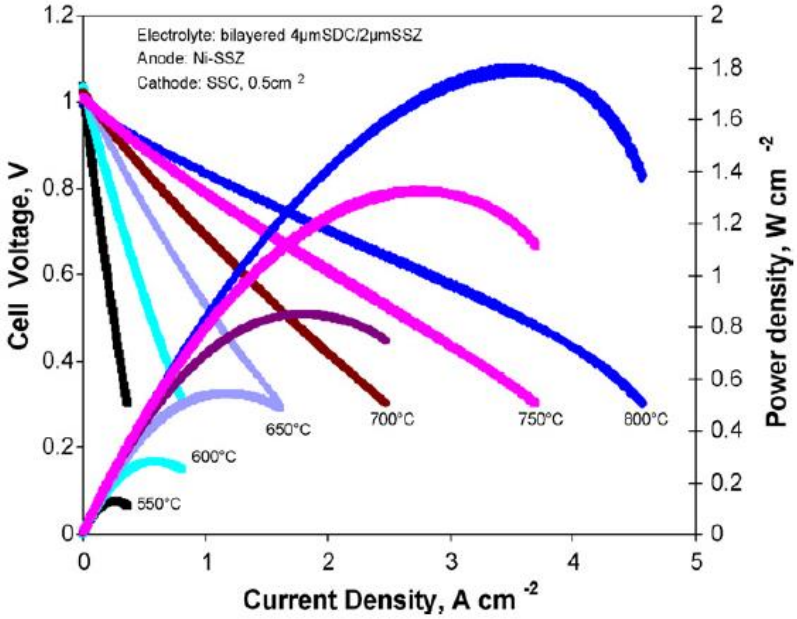


Figure 2-8 I-V characteristics of ScSZ/SDC bilayer electrolyte unit cell using SSC cathode [Zhang, X., et al. Journal of Power Sources, 2008. 175(2)][65]

Thin film ScSZ/SDC bilayer electrolyte based SOFCs were developed by Yang et al. [66] using PLD. PLD process parameters for the two layers were optimized to achieve cubic phase for ScSZ and SDC at 400 and 200 °C, respectively, and no reaction was observed because of the low processing temperatures. With increase in substrate temperature, density of ScSZ layer was found to decrease while density of SDC layer was found to increase due to the different band gaps vis a vis the laser photons. For the fabrication of full-cells, ScSZ film of 1 μm thickness was first deposited at 200-400 °C on NiO-SDC substrate, followed by deposition of SDC film of 6-7 μm thickness at 400-600 ^{o}C. OCV of ScSZ/SDC bilayer cell with SSC-SDC (75:25) cathode was 1.04 V and MPD was 0.5 and 1.6 W/cm^2 at 550 and 700 °C, respectively.

Solovyev et al. [67] used bipolar reactive magnetron sputtering to fabricate YSZ/GDC bilayer electrolyte SOFCs with NiO-YSZ anode and LSCF-GDC cathode. Monolayer YSZ and GDC cells were also fabricated and tested. It was shown that bipolar reactive magnetron has almost three times higher deposition rate than DC sputtering. The deposited YSZ and GDC layers showed cubic structure without the presence of any secondary phase. Monolayer YSZ cell studies indicated that below 2 μm YSZ thin film did not provide sufficient gas tightness and OCV decreased significantly. Among the different monolayer YSZ cells, a 4 μm thick YSZ cell showed the highest MPD of 0.25 and 0.58 W/cm^2 at 650 and 800 °C, respectively. In comparison, a 2.8 μm thick monolayer GDC cell showed a higher MPD of 0.54 mW/cm^2 at 650 °C. On the other hand, a bilayer cell with YSZ and GDC thickness of 4 and 1.5 μm, respectively, showed OCV of 1.13 V and MPD of 1.25 W/cm^2 at 800 °C. Unfortunately, the performance of bilayer samples below 750 °C was not reported in this study.

Lu et al. [68] tested YSZ/SDC bilayer electrolyte SOFCs made by PLD. NiO-YSZ anode substrate was prepared by tape casting and lamination. YSZ and SDC thin film of 0.5-1 and 5 μm, respectively, were deposited at 1000 °C. $La_{0.6}Sr_{0.4}Co_{0.2}Fe_{0.8}O_3$ layer was screen printed and then coated with $La_{0.8}Sr_{0.2}CoO_3$ layer to act as cathode functional layer and cathode current collector, respectively. At 650 °C, OCV and MPD of YSZ/SDC bilayer cell was 0.95 and 0.99 V and 0.95 and 1.37 W/cm^2 in air and oxygen at cathode, respectively. The power density improvement in oxygen was due to the significantly lower non-ohmic ASR of the cell. Stability of YSZ/SDC cell was tested at 1 A/cm^2 and 650 °C for 400 hours and only a slight decrease in cell voltage was observed.

Effect of anode functional layer (AFL) on YSZ /SDC bilayer electrolyte based SOFCs was studied by Qian et al. [69]. Both electrolyte films were deposited on pressed NiO-YSZ (60:40) anode by PLD at 600 °C, followed by post-anneal at 800 °C. To achieve smoother, denser electrolyte films, NiO-YSZ (50:50) AFL of 12 μm thickness was deposited on the anode substrate by drop-coating of AFL slurry. Thickness of YSZ and SDC films was 2 and 6 μm, respectively. Using SSC-SDC (70:30) cathode, OCV of YSZ/SDC cell without AFL was 0.85 V, which was higher than that of monolayer SDC cell (0.78 V); MPD of the cell without AFL was 0.75 W/cm^2. In comparison, YSZ /SDC bilayer cell with AFL showed higher OCV and MPD of 1.01 V and 0.9 W/cm^2 at 650 °C, respectively. The increase in MPD was attributed to the lower polarization resistance of the cell because of AFL addition. The stability of YSZ /SDC bilayer cell was tested at 600 °C for 50 hours and OCV slightly dropped by 0.98%.

Myung et al. [70] fabricated and tested ultra-thin YSZ/GDC bilayer electrolyte SOFCs by PLD. NiO-YSZ AFL (2 μm thick) was deposited by PLD to modify surface roughness of NiO-YSZ anode substrate; LSC cathode was also deposited by PLD. Thickness of YSZ film was varied between 0-0.2 μm, while thickness of GDC film was 1.0 μm. YSZ grains in the thin film demonstrated a homoepitaxial relationship with YSZ grains in the anode and a heteroepitaxial relationship with GDC grains. YSZ/GDC bilayer electrolyte was found to increase OCV from 0.6 V to over 1 V at 600 °C (Figure **2-9**). Furthermore, MPD of bilayer cells was significantly higher (>1 W/cm^2 at 600 °C) compared to monolayer GDC cells (0.38 W/cm^2 at 600 °C) as shown in Figure **2-10**. It was noted that roughness of the anode substrate played an important role in the reproducibility of OCV among cells with the same thickness.

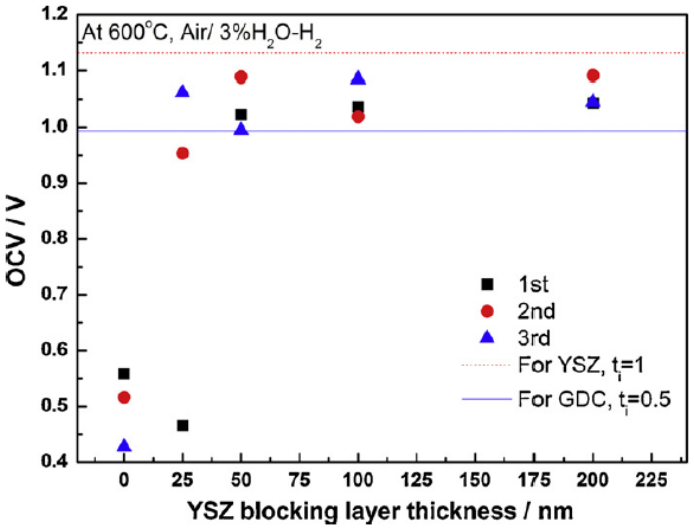


Figure 2-9 Measured OCV value of bilayer YSZ/GDC(1 μm) cells at 600 °C as a function of YSZ thickness. Solid line indicates calculated OCV of GDC with ti = 0.5 and dotted line indicates OCV of YSZ.[70]

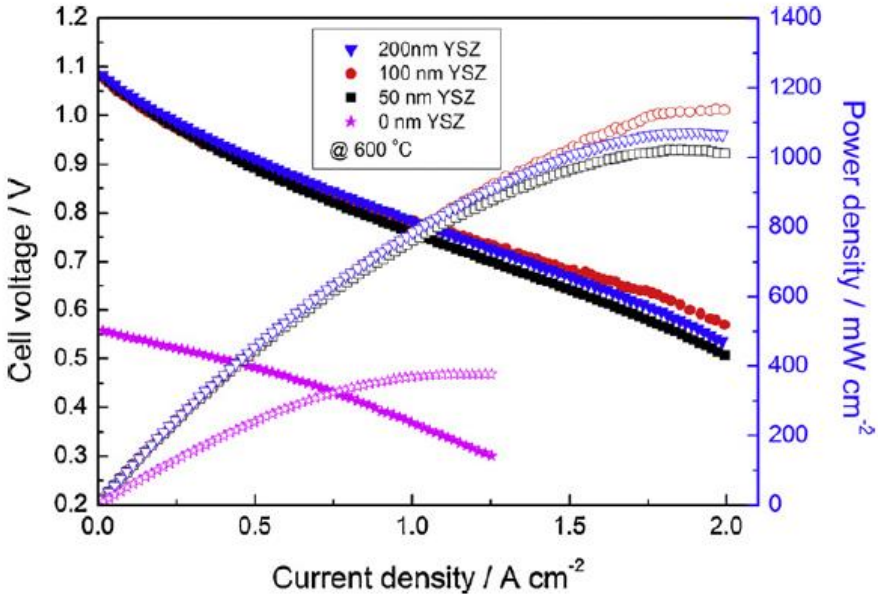


Figure 2-10 I-V characteristics of YSZ/SDC bilayer electrolyte unit cells with various YSZ layer thickness at 600 °C [70]

Ultra-thin YSZ/GDC bilayer electrolyte based SOFCs using chemical solution deposition (CSD) technique were fabricated by Oh et al. [71]. A nanoparticle based solution with 5% volume loading was spin-coated on NiO-YSZ substrate (56:44). CSD

required that the film thickness be greater than both grain size of the film and pore size of the substrate but allowed the fabrication of thin films of YSZ (0.1 μm) and GDC (0.1 μm) at substantially lower sintering temperatures. It was noted that addition of slow-sintering nanoparticles to the chemical solution was effective in suppressing generation of macro-defects and directional development of film microstructure, which typically is observed in CSD due to constrained sintering. Full cells were made with LSCF-GDC cathode. OCV of YSZ/GDC bilayer cells was >1 V at 500-650 °C and MPD was 1.3 W/cm^2 at 650 °C. The authored claimed to have developed the thinnest bilayer SOFCs and suggested that CSD can effectively replace vacuum deposition of thin film SOFCs.

Cathode supported micro-tubular design was used to evaluate performance of ScSZ/GDC bilayer electrolyte by Yamaguchi et al. in multiple studies but unfortunately, the performance was comparatively lower than that of anode supported designs [87] [88] [89]. LSM cathode support was fabricated by extrusion and ScSZ/GDC bilayer electrolyte was fabricated by dip-coating in GDC and ScSZ slurries and co-firing at 1300 °C. NiO-GDC anode layer was also made by dip coating. The final sintered bilayer electrolyte cell consisted of 15 μm ScSZ and 20 μm GDC thick layers. OCV of the bilayer cell was 1.1 V at 500 °C and MPD was 0.07 and 0.20 W/cm^2 at 600 and 750 °C, respectively. Electrode ASR accounted for the low power density and LSM-GDC interlayer was added at GDC/LSM interface [88] which reduced the electrode ASR from 20 to 5 Ωcm^2 at 600 °C and MPD of the cell was increased from 0.23 to 0.38 W/cm^2 at 750 °C. The tubular design allowed rapid heating and cooling cycles without performance degradation after 5 cycles. In another study, the anode

composition was optimized and NiO:GDC at 50:50 ratio was found to show 6 times higher MPD than that at 70:30 ratio [89], due to lower mass transport limitations.

Metal supported ScSZ/SDC bilayer electrolyte SOFCs with SSC-SDC cathode were developed by Hui et al.[72]. SS430 was used as the metallic support and NiO-SDC anode was deposited by spin-coating. ScSZ (2 μm) and SDC (20 μm) layers were deposited by PLD and sintered at comparatively low temperature of 850 °C to minimize oxidation of the metallic support. OCV of ScSZ/SDC bilayer cell was found to be 1.00-1.03 V at 400-600 °C. MPD was low (0.16 W/cm^2 at 600 °C) but the performance at 500 °C was stable for over 11 days. It was found that most the voltage loss was due the ohmic resistance of the cell.

2.2.1.2 Bilayer cells with zirconia at the cathode side

A ceria/zirconia bilayer electrolyte based micro-SOFC with ceria on the anode side was developed by Lee et al. [90]. Stainless steel (STS-434L) was used as substrate to deposit a nano-porous Ni layer by screen printing and sintering in dry hydrogen at 575 °C. NiO-GDC (60:40) anode, GDC, YSZ, $La_{0.7}Sr_{0.3}CoO_3$ layers were deposited by PLD. OCV and MPD of the cell was 0.91 V and 0.03 W/cm^2 at 450 °C and remained stable for over 100 hours of testing. It was noted that ohmic resistance of the cell remained constant, indicating that delamination between the cell components did not occur. Non-ohmic resistance of the cell significantly decreased during the first 100 hours and then remained stable, which was attributed to slow kinetic of NiO reduction at 450 °C. The authors claimed their work to be the longest lasting operation of a micro-SOFC based on STS-NiO metallic support.

Ceres Power is working on commercialization of metal supported trilayer electrolyte

based SOFC technology [91]. The company's "Steel Cell" is based on a thick film GDC layer which provides mechanical integrity and gas tightness, a thin film electron blocking layer (most likely zirconia based) to block leakage current in GDC, and a thin film GDC layer to avoid reaction between the electron blocking layer (which would be necessary if that electron blocking layer is zirconia based as described in section below) and perovskite based cathode (Figure **2-11**). The layers including nickel-ceria anode are deposited on a ferritic stainless steel substrate using conventional ceramic processing techniques. Additionally, metal support provides improved mechanical robustness compared to the anode supported planar design. OCV of the trilayer electrolyte based cell was improved to 1.17 V by reduction in electrolyte defects and other improvements. Over the years, power per cell was increased from 10 W in 2010 to 20 W in 2015 largely by optimization in materials and mechanical design within the stack as shown in Figure **2-12**[91]. Lastly, the metal supported design showed encouraging long term stability and thermal cycling results.

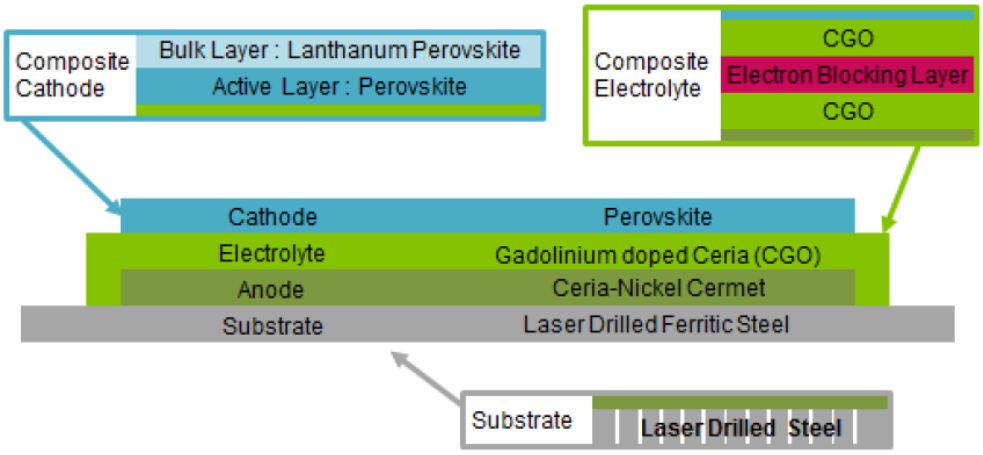


Figure 2-11 Schematic representation of Ceres Power "Steel Cell" [91]

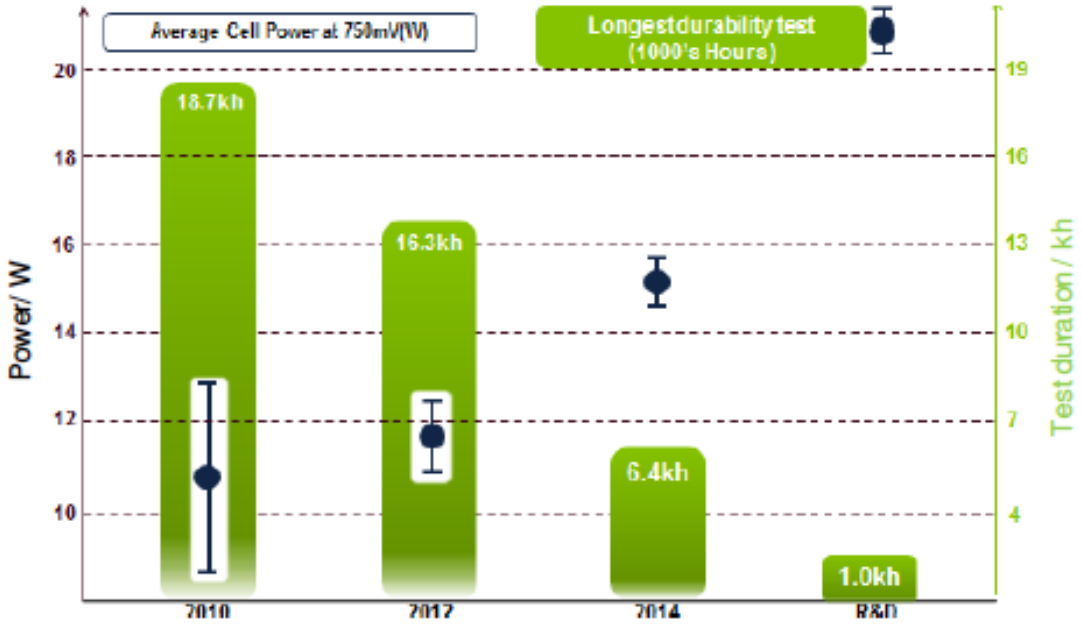


Figure 2-12 Average cell power and longest durability tests of Ceres Power "Steel Cell" technology over years [91]

2.2.1.3 Zirconia based Zirconia/Ceria bilayer HT-SOFC

The primary purpose of ceria based bilayer electrolytes paired with zirconia is to protect the GDC layer from reduction and enhance the OCV of the cell. However, zirconia/ceria based bilayers have been used for other reasons. Within the structure of Zirconia based bilayer cells, the thinner GDC layer is normally inserted as a buffer layer to limit the diffusion of strontium and cobalt from the cobalt containing cathode such as LSC and LSCF into the YSZ and thus preventing the formation of resistive phases. However, YSZ and GDC are known to have chemical incompatibility. During the conventional high temperature sintering of the electrolyte at 1450 ºC resistive compounds with two orders of magnitude lower conductivity than YSZ form and surface porosity as a result of Kirkendhal effect occurs. Hence, the major focus of different works in this category is to develop methods for low temperature fabrication

of zirconia/ceria electrolyte such as effect of additives for lowering the sintering temperature of the bilayer electrolyte[92] [71] [93], using sputtering for deposition of electrolytes [94] [95] [96], spray pyrolysis [97], PLD [98] [99], and electron beam physical vapor deposition (EB-PVD) [100].

Due to the relatively low conductivity of YSZ and sluggish oxygen reduction reaction kinetics at lower temperatures, many works targeting 500 ºC and lower temperature SOFCs are focused on the fabrication of ultra-thin electrolytes and using noble metal electrodes such as platinum. In such zirconia based YSZ/GDC bilayer electrolyte SOFCs, GDC layer is usually implemented to reduce electrode overpotential and achieve high OCV despite the extremely thin (few hundreds nm) electrolytes. It is well known that oxygen ion conductivity of the electrolytes adjacent to the cathode and anode impacts the non-ohmic polarization and a faster oxygen ion conductor such as doped ceria comparing to zirconia can enhance the performance of the cell particularly at lower temperature. Although such thin bilayer electrolyte micro-SOFCs showed high performance at lower temperatures (1.3 w/cm^2 at 450 ºC [3]), they are typically fabricated using semi-conductor processing equipment such as plasma enhanced atomic layer deposition (PEALD) [101], aerosol assisted chemical vapor deposition (AA-CVD) [102], and combination of ALD and PLD [3] and require noble metals such as platinum as their electrodes and thus are very expensive to fabricate. Following the same rational, a few works in literature showed the application of a thin GDC layer at the anode side of a zirconia based SOFC to reduce the anodic overpotential of the cell [103] [104] [105].

2.2.2 Zirconia/Bismuth oxide bilayer based IT-SOFCs

Some researchers have looked at improving the performance of YSZ based SOFCs for intermediate temperature operation by incorporating a bismuth oxide layer on the cathode side. Joh et al. [106] fabricated a YSZ/ESB bilayer electrolyte SOFCs using LSM-ESB cathode. NiO-YSZ anode (65:35) was made by tape casting and pre-sintered at 900 °C. Both YSZ and ESB electrolytes were deposited via colloidal drop-coating and sintered at 1400 and 800 °C, respectively. LSM-ESB cathode (50:50) was screen-printed and sintered at 800 °C. No reaction between YSZ and ESB layers was observed after heat treatment at 800 °C and after testing of unit-cells by EDS analysis. OCV of the bilayer cell with 7 μm YSZ layer and 5 μm ESB layer was >1.10 V at all temperatures due to the unity transference number (t_i) of YSZ electrolyte and at 650 °C, MPD of the bilayer cell was 1.62 W/cm^2. MPD of the bilayer cell was 2.08 W/cm^2 at 700 °C, which compared favorably to the monolayer 7 μm YSZ cell which showed MPD of 0.86 W/cm^2 (Figure **2-13**). The significant improvement in power density of the bilayer cell was attributed to faster oxygen reduction reaction at the cathode/electrolyte interface in presence of ESB layer. The enhanced electrode kinetics was confirmed by the reduction in cathodic overpotential and a higher exchange current density.

In another work, Wang et al. [107] have looked at YSZ/21NbSB bilayer electrolyte SOFCs made by RF magnetron sputtering. Ni-SDC and silver was used as anode and cathode, respectively. YSZ layer was deposited at 300 °C using Ar:O2 mixture of 30:1. For 21NbSB layer, the composition of the deposited film depends greatly on the gas mixture composition which with an Ar:O2 mixture of 31:7 yielded the closest film

composition to the target composition. It was found that the bilayer electrolyte deposited at 300 °C was thermally stable and did not crack after 700 °C anneal. However, MPD of the cell was rather low 0.01 W/cm^2 at 600 °C using 4 μm YSZ and 1.5 μm NbSB bilayer electrolyte.

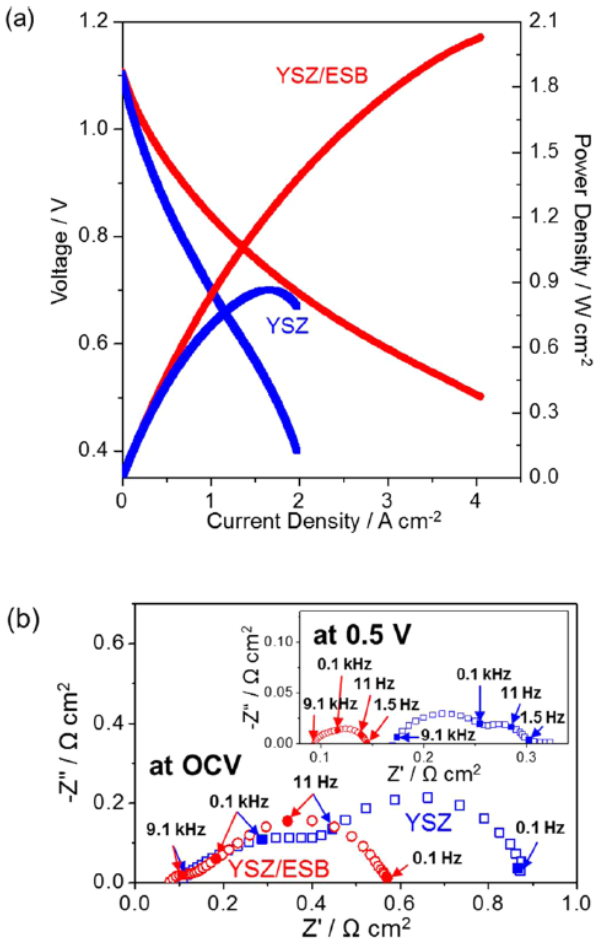


Figure 2-13 I-V characteristics and impedance spectra of monolayer YSZ cell and YSZ/ESB bilayer electrolyte cell at 700 °C using humidified H2 and air at anode and cathode sides respectively [106]

2.2.3 Ceria/bismuth oxide bilayer LT-SOFCs

As reviewed in the previous section, the initial bilayer electrolyte cells were built using thick electrolyte pellets and noble metal electrodes, and the cell performance was low.

To improve bilayer cell performance, research focused on developing anode supported cells using thin film electrolyte and new cathode materials compatible with bismuth oxide electrolyte were carried out. Traditional cathode materials for IT-SOFCs such as perovskite LSCF show extreme reactivity with bismuth oxide and among noble metals, Pt is known to form secondary phases such as $Bi_2Pt_2O_7$ with bismuth oxide [57]. One of the cathodes discovered was a bismuth ruthenate (BRO)-ESB composite by Jaiswal [76]. It was shown that BRO and ESB phases are compatible with each other by XRD and DSC studies. Another system under investigation is LSM-ESB composite [108]; however, the compatibility results are non-conclusive with respect to reaction between LSM and ESB and the consequent effect on electrode performance and stability.

Ahn et al. [47] [80] fabricated anode supported cells with thick film bilayer electrolyte by different fabrication routes and studied cell performance using different cathodes. Ni-GDC/GDC half-cells were made by either co-pressing of anode and GDC powders or by spray coating of GDC layer on tape-casted anode. Co-pressing method resulted in a relatively thick (~50 μm) GDC layer, while spray coating method resulted in 10-20 μm GDC layer. For the cells made by the co-pressing method, an ESB layer was made by screen-printing using solid-state powders. For the cells made by spray-coating, ESB layer was made by either screen-printing using co-precipitated powders or by hot/cold PLD. In the last step, BRO-ESB cathode was brush-painted to complete the cell. SEM cross-section image of a GDC/ESB bilayer cell is shown in **Figure 2-14**. The performance of the bilayer cells was compared with monolayer GDC cell using standard LSCF-GDC cathode. For the co-pressed cells, screen-printed ESB layer did not sinter completely into a dense layer due to large size of solid-state powders and,

thus, was found to not effectively increase OCV of the bilayer cell. On the other hand, the BRO-ESB cathode reduced ASR of the bilayer cell resulted in a maximum power density (MPD) of 0.59 W/cm^2 at 650 °C which was higher than that of the monolayer GDC cell with LSCF-GDC cathode (0.34 W/cm^2). For the cell made by spray-coating, OCV was significantly lower due to the lower thickness (10-20 μm) of GDC layer but the screen-printed ESB layer was found to be effective in increasing OCP from 0.67 to 0.75 V, resulting in an increase in MPD of the cell from 0.41 to 0.61 W/cm^2 at 650 °C.

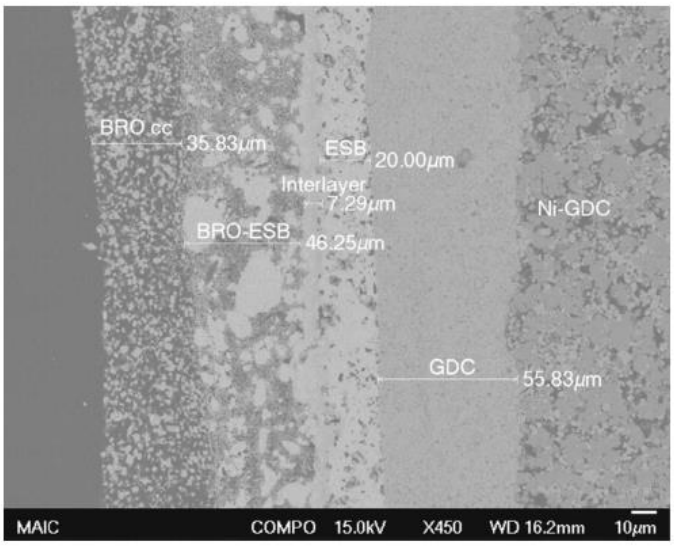


Figure 2-14 Backscattered SEM image showing cross-section of Ni-GDC/GDC(50 μm)/ESB(20 μm)/BRO-ESB/BRO cc unit cell. cc refers to current collector [47]

Moreover, the ESB layer made by hot PLD exhibited lower ohmic and non-ohmic ASR and higher OCV (0.77 V vs. 0.72 V at 650 °C) compared to that of the monolayer GDC cell, resulting in 93% increase in MPD from 1.03 W/cm^2 for monolayer cell to 1.95 W/cm^2 for bilayer cell with ~ 4 μm thick ESB layer made by hot PLD (**Figure 2-15**). The improvement in cell performance was ascribed to the combined effect of higher OCV using ESB layer and 43% lower ASR using BRO-ESB composite cathode. This ~2 W/cm^2 at 650 °C performance set the benchmark for high power density

ceria/bismuth oxide bilayer electrolytes and a subsequent publication [34] laid out the potential and issues for this technology.

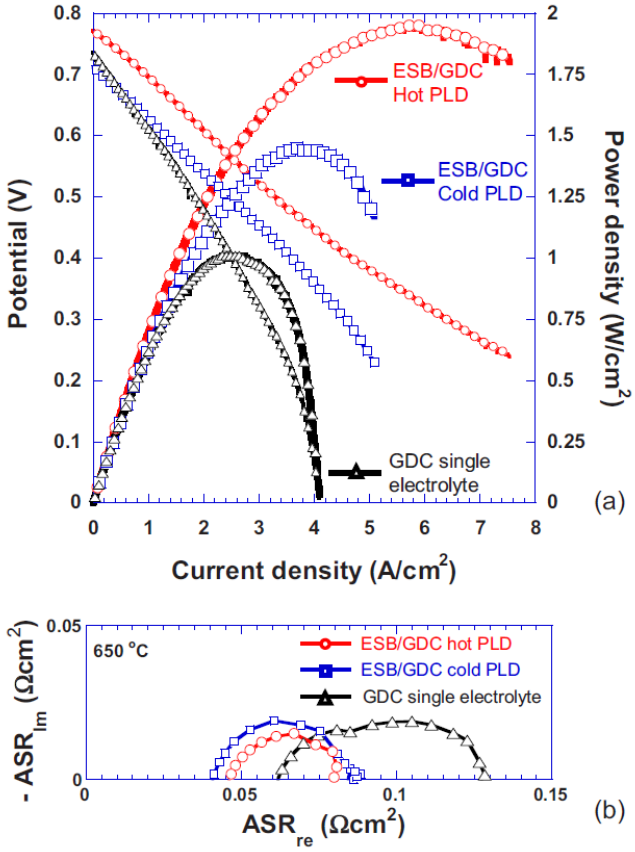


Figure 2-15 I-V characteristics and impedance spectra of monolayer GDC cell and GDC/ESB bilayer electrolyte cell made by hot/cold PLD [47]

As a result, numerous groups investigated this approach and continued the improvement in OCP and power density. However, while the result of ceria/bismuth oxide bilayer electrolyte based SOFCs was impressive, the OCV was lower than theoretical, suggesting that further optimization of relative thickness and total thickness of the bilayer electrolyte needs to be carried out. As such, there is tradeoff in optimizing total thickness of bilayer electrolyte between reducing ASR with thinner electrolytes and increasing OCV with thicker electrolytes [79]. In addition, for bilayer electrolytes,

OCV further depends on the relative thickness of the two layers. Lee et al. [48] studied anode supported GDC/ESB bilayer cell with BRO-ESB cathode to understand the effect of relative thickness of the two electrolyte layers on the cell performance. GDC electrolyte layer was deposited by spin coating of GDC slurry on NiO-GDC anode support. ESB layer was fabricated by drop-coating using powders made from solid-state and co-precipitation methods. It was found that powders made by co-precipitation were finer and resulted in dense ESB layer after sintering at 800 °C. Cells with different GDC and ESB thicknesses were fabricated and it was observed that by increasing the thickness of GDC and ESB layers, OCV of the cell increased. MPD of a bilayer cell with 10 μm GDC and a 5 μm thick ESB reached over 1.5 W/cm^2 at 650 °C. The increase in MPD compared to the monolayer GDC cell (0.87 W/cm^2) was due to both higher OCV (0.8 vs. 0.75 V) and 47.6% lower ASR.

Lee et al. [81] studied the performance of GDC/ESB bilayer cells with LSM-ESB cathode using tape-cast anode and anode functional layer (AFL). GDC and ESB layers were deposited with spin coating of a colloidal solution and the sintered thickness was 25 and 2 μm, respectively. MPD of the cell was 1.02 W/cm^2 at 650 °C which was higher than all previously reported LSM cathode based SOFCs. In addition, cathode and cell performance was stable for over 80 and 200 hours of testing, respectively. Further improvement in cell performance was suggested by replacing GDC/ESB bilayer combination with higher conductivity doped ceria and stabilized bismuth oxide electrolytes such SNDC and DWSB [79]. Redox Power Systems is utilizing these developments in ceria/bismuth oxide bilayer electrolyte to develop commercial SOFCs operating at low temperatures.

Recent reports on ceria/bismuth oxide bilayer electrolyte based SOFCs by Zhang et al. [46], Lee et al. [82], and Hou et al. [50] [109] have looked at SDC and SNDC based ceria electrolytes, YSB based bismuth oxide electrolytes, and LSM based cathodes. For SDC/YSB bilayer SOFCs using LSM-YSB cathode, by Zhang et al. [46], NiO-SDC (60:40) anode and SDC electrolyte were co-pressed and co-fired at 1250 °C. YSB electrolyte was deposited using DC magnetron sputtering in argon/oxygen mixture at room temperature and then annealed at 800 °C for 2 hours. Thickness of the SDC and YSB layers was 26 and 6 μm, respectively. Using the bilayer electrolyte, OCV of the bilayer electrolyte cell increased to 0.85 V compared to 0.78 V of the monolayer SDC cell at 650 °C. MPD also increased from 0.29 W/cm^2 for the monolayer cell to 0.38 W/cm^2 for the bilayer cell. Ohmic resistance of the bilayer cell did not change with the addition of the YSB layer due to its high conductivity. However, the non-ohmic resistance of the bilayer cell under load was much lower than that of the monolayer cell due to the positive effect of YSB electrolyte on cathodic polarization. Overall increase in MPD was attributed to the higher OCV and lower cathodic polarization of the bilayer electrolyte.

Lee et al. [82] reported on their work on GDC/YSB bilayer SOFCs using LSM-YSB cathode. NiO-GDC anode support was fabricated by powder pressing and sintering at 1100 °C. GDC electrolyte was deposited by drop coating and sintering at 1400 ^oC, while YSB electrolyte and LSM-YSB (50:50) cathode was screen-printed and sintered at 800 °C and 850 °C, respectively. Thicknesses of GDC and YDB layer was 20 and 10 μm, respectively. For the reference monolayer GDC cell, LSM-GDC was used as the cathode material. The bilayer cell showed a slightly higher ohmic ASR but a

significantly lower non-ohmic ASR compared to the monolayer cell with LSM-GDC cathode. The lower non-ohmic ASR was attributed to the lower resistance of LSM-YDB for charge transfer at electrode/electrolyte interface. It was also noted that despite a significantly lower ionic conductivity of LSM compared to LSCF, LSM-YSB cathode showed similar performance to that of LSCF cathode at 650 °C, suggesting to the beneficial effect of YSB in the composite cathode. The bilayer electrolyte enhanced the OCV from 0.50 to 0.89 V and MPD improved from 0.21 to 0.53 W/cm^2 at 650 °C.

Hou et al. [50] [109] fabricated $Sm_{0.075}Nd_{0.075}Ce_{0.85}O_2$ (SNDC)/ESB and GDC/ESB bilayer electrolyte SOFCs using $La_{0.74}Bi_{0.1}Sr_{0.16}MnO_3$(LBSM)-ESB (50:50) as cathode. Ni-ceria (60:40) anode and ceria electrolyte was prepared by co-pressing and sintering at 1400 °C. ESB electrolyte was deposited by drop coating and sintering at 800 °C. Thickness of ceria and ESB layers after sintering was 20 μm each. Bismuth doping of LSM was found to be effective in limiting any reaction between LBSM and ESB after high temperature sintering as confirmed by the XRD diffraction pattern analysis. Impedance spectroscopy showed that above 550 °C, ohmic losses accounted for majority of the cell resistance. At 650 °C, OCV and MPD of the SNDC/ESB bilayer cell reached 0.80 V and 0.98 W/cm^2 , respectively, as shown in Figure 2-16 [109]. At 450 °C, MPD of the bilayer cell was 0.13 W/cm^2, which the authors claimed to be the highest recorded value at 450 ^{o}C [109]. Hou et al. in another work compared the electrochemical performance of SNDC/ESB to that of GDC/ESB bilayer electrolyte SOFCs [109]. At 650 °C, OCV and MPD of SNDC/ESB and GDC/ESB cells was 0.81 V and 0.93 W/cm^2 and 0.83 V and 0.90 W/cm^2, respectively. The higher MPD of SNDC/ESB cell was attributed to the lower ohmic ASR of the SNDC/ESB cell, as

confirmed by the impedance spectroscopy. In addition, it was noted that the conductivity of the bilayer electrolyte calculated from the overall thickness of the electrolyte and the ohmic ASR of the cell was higher than that of SNDC and GDC. The authors argued that the measured conductivity in an operating cell was higher than the conductivity measured in air due to consumption of oxygen at anode. However, impedance measurements were performed at open circuit condition and, hence, consumption of oxygen at anode should be negligible and cannot be expected to affect the conductivity of the bilayer electrolyte.

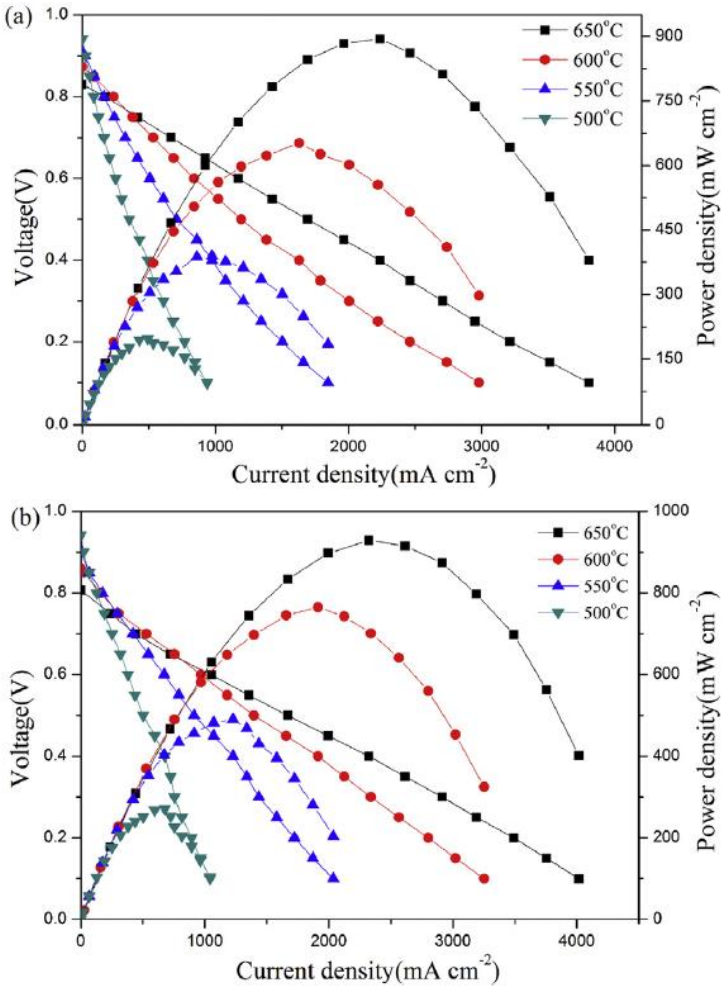


Figure 2-16 I-V characteristics of (a) GDC/ESB and (b) SNDC/ESB bilayer electrolyte unit cells using LBSM-ESB cathode [109]

Other researchers have studied ceria/bismuth oxide bilayer electrolyte using different cathode materials – Pt [110], Ag-YSB [49], and $Pr_{0.5}Ba_{0.5}MnO_3$ (PBM) [83]. Leng [82] and Chan [110] fabricated GDC/YSB bilayer SOFCs using Pt cathode. NiO-GDC anode and GDC electrolyte was fabricated by co-pressing and sintering at 1350 °C. YSB was applied by screen printing and sintered at 900 °C. SEM micrograph of the bilayer cell showed a dense, 84 μm thick GDC layer and porous, 16 μm thick ESB layer. The porous ESB layer was able to marginally enhance OCV of the bilayer cell from 0.75 to 0.81 V at 700 °C. Although the ohmic resistance of the cell did not change, the non-ohmic polarization ASR of the bilayer decreased by 36%. MPD of the bilayer cell was relatively modest but increased from 0.16 to 0.26 W/cm^2 at 700 °C due to the higher OCV and lower ASR of the bilayer cell. Zhang et al. [49] fabricated and tested SDC/YSB bilayer electrolyte SOFCs with Ag-YSB cathode. NiO-SDC anode and SDC electrolyte were pressed and co-fired at 1250 °C for 5 hours. YSB layer was deposited using the DC magnetron sputtering and annealed at 800 °C for 2 hours. Thickness of SDC and YSB layer was 26 and 6 μm. Ag-YSB (60:40) composite cathode was deposited by screen-printing. The bilayer SDC/YSB electrolyte improved OCV from 0.80 to 0.89 V at 500 °C, while MPD of the cell improved from 0.13 to 0.22 W/cm^2. At 600 °C, MPD of the bilayer cell was 0.57 W/cm^2. Impedance studies using symmetrical cells showed ASR of Ag-YSB cathode on the YSB electrolyte was lower than that on the SDC electrolyte and suggested that the increase in MPD of the bilayer cell was due to both higher OCV and lower interfacial polarization compared to the monolayer SDC electrolyte cell. Hou et al. [83] developed a new PBM perovskite and

ESB (50:50) based composite cathode for SNDC/ESB bilayer electrolyte SOFCs. PBM and ESB powders were made using citric acid-nitrate gel combustion method. PBM showed a perovskite structure composed of cubic and hexagonal phases but after firing with ESB at 750 °C for 3 hours showed minor secondary phase in the XRD diffraction patterns. Activation energy for PBM-ESB cathode was estimated to be 1.38 eV. NiO-SNDC (60:40) anode substrate and SNDC electrolyte were co-pressed and fired at 1400 °C. ESB electrolyte was deposited by drop-coating and sintered at 800 °C. OCV and MPD of the bilayer cell with 22 μm thick SNDC layer and 20 μm thick ESB layer was 0.80 V and 0.99 W/cm^2 at 650 °C, respectively.

In solid electrolytes, doping of aliovalent cation increases the oxygen vacancy concentration but the oxygen ion conductivity can be enhanced by increasing the dopant concentration only up to a certain level. Beyond that level, the ionic conductivity decreases due to association of vacancies or formation of defect complexes in the dilute solution range and formation of super-lattices or ordering of vacancies in concentrated solution range [53, 54]. Extent of anion sublattice ordering can be reduced by using highly polarizable dopants with ionic radii close to that of the host cation and randomizing the site energetics by multi-cation doping [111]. This approach has been used to develop double-doped ceria and double-doped, such as samarium and neodymium co-doped ceria (SNDC) [112] and dysprosium and tungsten co-stabilized bismuth oxide (DWSB) [111], which show higher oxygen ion conductivity compared to ESB and GDC, respectively. In bismuth oxide system, double doping reduces the amount of dopant required to stabilize the cubic phase to room temperature and, hence, increases the ionic conductivity compared to traditional

ESB. In addition, cubic ESB electrolyte suffers from disorder-order transformation on the oxygen-ion sublattice at ~500 °C, resulting in decay in oxygen ion conductivity with isothermal aging [54]. Recent understanding on the interplay between dopant type/level and phase composition has resulted in the development of new stabilized bismuth oxide composition which show stable ionic conductivity at ~500°C[85, 113]. Ruth et al. [84] have studied the performance of bilayer SOFCs using double-doped bismuth oxides, i.e. GDC/DWSB and GDC/DGSB. At 650 °C, conductivity of DGSB and DWSB was 0.94 and 0.53 S/cm, respectively, which was significantly higher than of ESB. Ni-GDC and LSM-ESB was used as anode and cathode material, respectively. OCV of bilayers cells with 20 μm GDC and 3-5 μm bismuth oxide layers at 650 °C was ~0.8 V, while MPD was 0.6, 0.9, and 1.3 W/cm^2 for ESB, DWSB, and DGSB based bilayers, respectively.

An interesting work on layered heterostructure consisting of alternating GDC/ESB layers was reported by Sanna et el. [114] with the goal to improve the stability of ESB phase to room temperature and in reducing environments. The alternating GDC/ESB layers were deposited on a MgO substrate using PLD to result in $MgO/GDC/[ESB/GDC]_N$ structure, where N was varied from 1 to 30. For a constant film thickness of 60 nm, N = 20 showed the highest conductivity in both air and reducing environments. Unlike bulk ESB, the order-disorder transition and related conductivity decay was not observed at 600 °C in air. Moreover, the conductivity of a heterostructure with N=20 was found to increase by two orders of magnitude in $90\%H_2/10\%\ N_2$ reducing environment at 533 °C. Lastly, the heterostructure was found to be stable in the reducing environment and the electrical conductivity was constant.

The conductivity results for the heterostructure were extremely interesting but no full cell results using the heterostructured electrolyte were presented.

2.3 Other types of bilayer electrolyte SOFCs

As mentioned previously, bilayer electrolytes serve distinct functions in a SOFC structure. In ceria/bismuth oxide or ceria based ceria/zirconia bilayers, bismuth oxide and zirconia layers block the leakage current through ceria and increases OCV. However, in other types of bilayer electrolyte SOFCs, the main electrolyte is not reduced and near theoretical OCV can be obtained and the major functionality of the secondary electrolyte is to suppress the reaction between the electrolyte and electrodes or protecting the electrolyte from reaction with fuel constituents such as water, CO_2 or SO_2. For instance, LSGM has high oxygen ion conductivity and shows near theoretical OCV. However, LSGM and Ni-based cermets react and resistive phases with low conductivity form at the interface. Hence many scholars have studied the potential of using a thin ceria based electrolyte such as SDC [115] [116] [117] [118] [119], or LDC [120] [121] [122] [123] as a diffusion barrier between the LSGM electrolyte and Ni-cermet anode. Proton conductor based SOFCs typically use doped $BaCeO_3$ as their electrolyte. Despite its high ionic conductivity $BaCeO_3$ suffers from poor chemical stability under CO_2, acidic gases and steam, which are prevalent under the operating environment of a SOFC. On the other hand, $BaZrO_3$ has a conductivity one order of magnitude lower than that of $BaCeO_3$. However, it possess a good chemical stability and hence the potential of protecting the $BaceO_3$ with a thin layer of $BaZrO_3$ has been studied in literature [124] [125] [125] [126]. Interested readers are referred to other

types of bilayers such as ceria/ BZCY [127] [128], LBAYO/SDC [129] or biphasic electrolytes [130, 131] [132] as a mean to improve the OCV of ceria based SOFCs.

2.4 Final Remarks

As summarized in **Table 2-1** and **Table 2-2**, for similar total electrolyte thickness and temperature, ceria/zirconia bilayer IT and HT-SOFCs yield higher OCV values compared to ceria/bismuth oxide IT and LT-SOFCs. However, due to the significantly lower ohmic ASR across the ceria/bismuth oxide bilayer electrolyte layers, these bilayer electrolyte SOFCs have the potential of delivering higher power density at lower temperatures. For example, at 650 ℃, ScSZ (6-7 μm)/ SDC(6-7 μm) bilayer electrolyte SOFC [66] and GDC (10 μm)/ESB (4 μm) bilayer electrolyte SOFC [80] (total electrolyte thickness of 14 μm) demonstrated OCVs of 1.04 V and 0.77 V, respectively; however, in terms of MPD, they achieved 1.38 and 1.95 W/cm^2 respectively.

As such, although many scholarly works in developing IT-SOFCs, are primarily focused on depositing a thin stabilized zirconia layer at lower temperatures using alternative processing methods, these bilayers often suffer from higher ohmic losses and hence despite having higher OCV, they deliver lower power output. Consequently, ceria/bismuth oxide bilayer electrolyte SOFCs are suggested as a more promising approach to reduce the SOFC operating temperature to 650-500 ℃. Towards this goal, (a) new doped bismuth oxide compositions with stable oxygen ionic conductivity at temperatures below 600 ℃ must be explored, (b) structure of the cell, i.e. bilayer electrolyte thickness ratio and fabrication processes must be engineered, and (c) new

cathode materials with low ASR at low temperatures, that are compatible with bismuth oxide, should be developed.

2.5 Conclusions

Lowering the operating temperature of the solid oxide fuel cell below 650 ºC reduces the manufacturing cost, decreases the performance degradation rate, and increases efficiency and hence can promote the commercialization of SOFC technology. Two major approaches to reduce the operating temperature are typically pursued as reviewed in this chapter: (a) Using alternative electrolyte materials with higher ionic conductivity such as doped ceria instead of the traditional YSZ, and (b) few microns or sub-micron electrolyte SOFCs. Sub-micron electrolyte SOFCs show reasonable power density at lower temperatures. However, fabrication requires more expensive semi-conductor processing such as advanced lithography, ALD, or sputtering and hence may not be cost effective for large scale power generation potential and so were not reviewed in detail in this work. Doped ceria such as GDC and SDC have ionic conductivity orders of magnitude higher than YSZ and hence have been explored extensively. However, ceria reduces under fuel condition of the SOFC which causes an internal leakage current and power dissipation. Stabilized bismuth oxide compositions such as ESB, YSB and DWSB have been shown to be capable of blocking the leakage current and increasing the OCV of the cell. Although many scholars have investigated the potential of using a thin zirconia layer to block the leakage current, ceria/bismuth oxide bilayer SOFCs showed higher power density values due to the much higher ionic conductivity of stabilized bismuth oxide compared to YSZ. Ceria/bismuth oxide thickness ratio controls the interfacial PO_2 and thus thermodynamic stability of bismuth oxide layer

and hence is of great importance and must be tuned carefully. Bilayer electrolyte SOFCs can serve other functions (other than blocking the leakage current) such as a diffusion barrier layer between electrolyte and adjacent electrodes or enhancing the catalytic activity of the cathode as a fast oxygen ion conductor.

3 Experimental Methods

In this chapter, experimental methods and procedures to synthesize and characterize materials will be outlined. In addition, experimental methods to fabricate the SOFC button cells and subsequent electrochemical testing including house-made reactor apparatus and sample preparation will be discussed.

3.1 Material Synthesis

3.1.1 Solid state

Majority of bismuth oxide compositions used in this work, were synthesized using solid state (SS) route. Solid state synthesis essentially requires adequate mixing of bismuth oxide with the dopant(s) oxide of interest, followed by a high-temperature calcination step. Various bismuth oxide compositions such as $(Bi_{0.8}Er_{0.2})_2O_3$ (ESB), $(Bi_{0.92}Nd_{0.04}Gd_{0.04})_2O_3$ (NGSB), and $(Bi_{0.75}Y_{0.25})_{1.86}Ce_{0.14}O_{3\pm\delta}$, (YCSB) were synthesized by mixing bismuth (III) oxide (99.99% purity, Alfa Aesar) with dopant oxides such as erbium oxide (Alfa Aesar, 99.99%) cerium oxide (Alfa Aesar, 99.99%), yttrium oxide (Alfa Aesar, 99.99%), and gadolinium oxide (Alfa Aesar, 99.99%) in sthiociometric ratios. Precursor materials were ball-milled in a 125 mL Nalgene (HDPE) bottle containing spherical 5 mm yttria-stabilized zirconium oxide (YSZ) milling media and ethanol for 48 hours. The powder was then dried in oven at 100 ℃. The obtained powder was then collected in an alumina crucible and calcined at 800 ℃ for 16 hours. The calcined powder was then ball-milled in ethanol for another 24 hours and then dried in oven (100 ℃) and grinded with a mortar and pestle.

3.1.2 Sol-gel Method

In order to synthesize nano-sized powder and obtaining a bismuth oxide composition with a higher purity, sol-gel method was used for the fabrication of YCSB powder. Stoichiometric amounts of bismuth nitrate (Alfa Aesar, 99.999%), cerium nitrate (Alfa Aesar, 99.99%), and yttrium nitrate (Alfa Aesar, 99.9%) were dissolved in HNO_3 and then citric acid ($C_6H_8O_7$) (Alfa Aesar 99+%) was added to the solution at citric acid:metal ions molar ratio of 1.5:1. Solution was then heated to 70 ℃ until gel was formed and then was heated to 350 ℃ for auto-ignition and combustion. Following the completion of the combustion process and formation of ash, powder was grinded, collected and calcined at 600 ℃ and 800 ℃ for 2 hours.

3.2 X-ray Diffraction

Phase purity and crystallinity of synthesized powders were analyzed using Bruker D8 Advance, Cu Kα at Crystallographic Center at the University of Maryland. Calcined powders were first ground using a mortar and pestle and then mounted on a silicon sample holder.

3.3 Symmetrical-cell Fabrication and Testing

Symmetrical cells were fabricated to measure the conductivity of a synthesized powder or study the performance of a cathode system under various conditions.

3.3.1 Symmetrical Cells for Electrical Conductivity Measurements

Conductivity of various electrolyte materials including GD, ESB, NGSB, and YCSB were measured using symmetrical cells and impedance spectroscopy. 1 gram of the

synthesized powder or purchased powder (GDC, Fuel Cell Materials) were pressed in a 10 mm diameter cylindrical die under a 2.5 tons load for 5 minutes. The pressed powder was then sintered at 1450 ℃, 800 ℃, 800 ℃, and 1100℃ for GDC, ESB, NGSB, and YCSB respectively. Following that, sintered pellet was polished, and dimensions of the pellets were measured and recorded. Gold paste (Electro-Science Laboratories) was brush painted on both sides of the pellets, together with silver mesh, and fired at 775 °C for 2 hours to form symmetrical cells. A bismuth oxide symmetrical cell is schematically shown in Figure **3-1** (a).

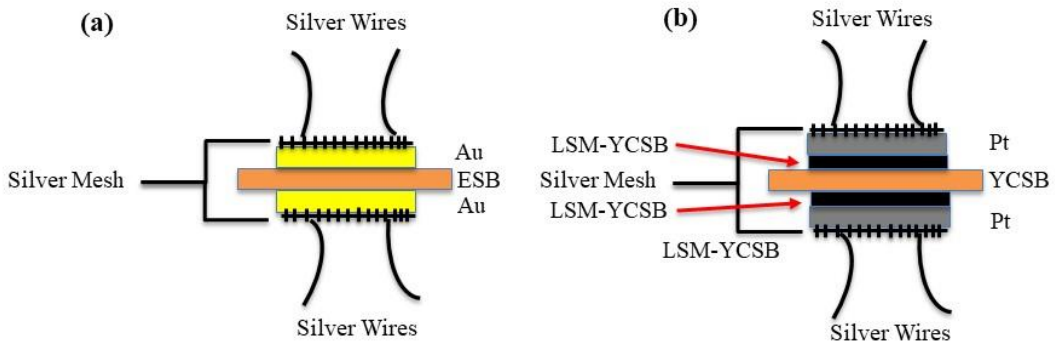


Figure 3-1 Schematic of (a) an electrolyte material, and (b) cathode material symmetrical cell using gold and silver mesh as current -collector

3.3.2 Symmetrical Cells for Studying Cathode Materials

In this work, nano-structured electrodes were developed and studied. To enhance the power density of a GDC/YCSB bilayer electrolyte SOFC, cathode and anode sides of the cell were infiltrated (as discussed in the future sections) with LSM and Ni/GDC nano-particles respectively. Effect of cathode infiltration was studied systematically at different temperatures and pO2 values. Symmetrical cells were prepared by blade-coating both sides of the YCSB pellet (as discussed in the previous section) with the LSM-YCSB (40:60 wt%) paste followed by oven drying (100 ℃ for 5 hours) and

sintering at 775 ℃ for 2 hours. Following that, silver mesh and wires were attached to the symmetrical cell using platinum paste and oven dried before the impedance spectroscopy measurements. The schematic of the LSM-YCSB/YCSB/LSM-YCSB symmetrical cell is shown in Figure **3-1** (b).

3.3.3 Impedance Spectroscopy

Impedance spectroscopy was done on the symmetrical cells in air or other pO2 values with oscillation voltage of 50 mV in frequency range of 0.1 Hz–10 MHz at different temperatures using Solartron 1470E frequency response analyzer and ZPlot software (Scribner Associates). The apparatus to measure the impedance of symmetrical cells is shown in Figure **3-2**.

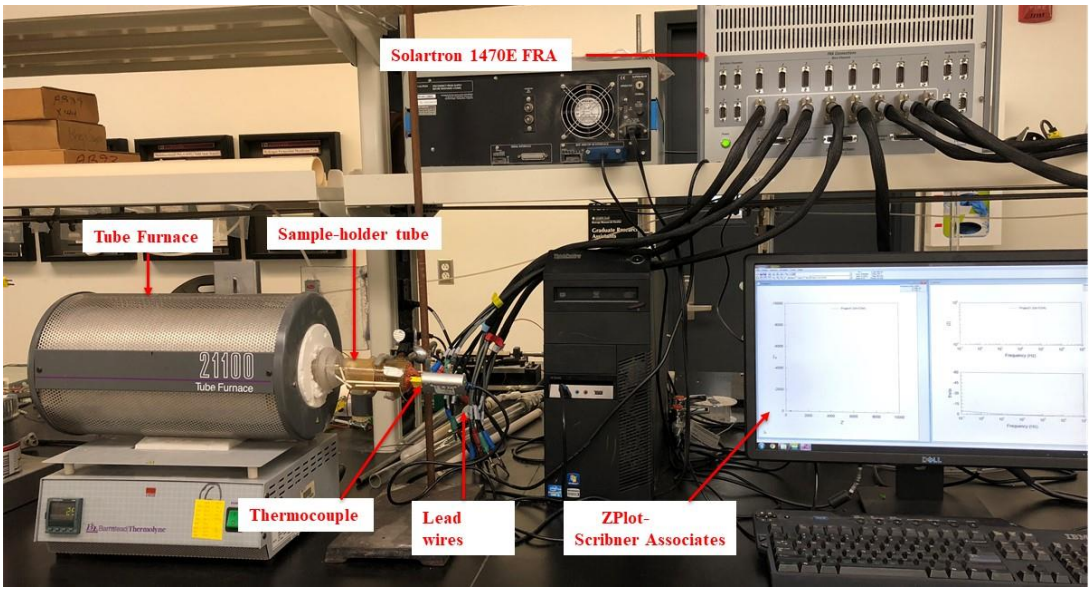


Figure 3-2 Experimental apparatus to measure the impedance of symmetrical cells.

3.4 SOFC Button-Cell Fabrication

3.4.1 Anode-supported Half-Cell Fabrication

Typical configuration of bilayer SOFCs consisted of ~600 μm NiO-$Ce_{0.9}Gd_{0.1}O_{2-\delta}$ anode support layer (ASL), ~20 μm NiO-$Ce_{0.9}Gd_{0.1}O_{2-\delta}$ anode functional layer (AFL), 10-70 μm $Ce_{0.9}Gd_{0.1}O_{2-\delta}$ first electrolyte layer, 2-25 μm stabilized bismuth oxide second electrolyte layer, and 20-40 μm cathode layer. The procedure to fabricate the bilayer SOFCs is schematically shown in Figure **3-3**. The individual layers of ASL, AFL, and GDC were made by tape casting process using a lab tape caster (Procast, TC-71LC) as shown in Figure **3-4**. For ASL tape, NiO (99.0% purity, 0.39 m^2/g, Alfa Aesar) and $Ce_{0.9}Gd_{0.1}O_{2-\delta}$ (99.0% purity, 12 m^2/g, Fuel Cell Materials) powders were oven-dried and mixed in a 60:40 weight ratio, followed by ball-milling in ethanol/toluene for 24 hours with Z3 menhanden fish oil (Tape Casting Warehouse) as dispersant. Following that, B-79 polyvinyl butyral binder (Tape Casting Warehouse) and S-160 benzyl butyl phthalate plasticizer (Tape Casting Warehouse) were added to the slurry and ball-milled for another 24 hours. The final slurry was degassed for 2 hours and cast as ASL tape. The same procedure was used for the casting of AFL and GDC electrolyte tapes. For AFL tape, high surface area NiO (99.40% purity, 4 m^2/g, J.T.Baker) and $Ce_{0.9}Gd_{0.1}O_{2-\delta}$ (Fuel Cell Materials) powders were mixed in a 50:50 wt. ratio. While for GDC electrolyte tape, $Ce_{0.9}Gd_{0.1}O_{2-\delta}$ (Fuel Cell Materials) was used. Square pieces were cut from the different tapes and laminated together in a hot press at 3 ton for 3 hours. Typically, three tapes of ASL were laminated first, followed by one tape of AFL. Multiple tapes of GDC were laminated together to get the desired electrolyte thickness. After lamination, discs of ~1.25-inch diameter were punched and

then sintered at 1450 °C. A multi-step heating profile was used for binder burnout and alumina setter plates were used to ensure flatness of the samples. After final sintering, diameter of anode supported GDC half-cell was ~1.00 inch.

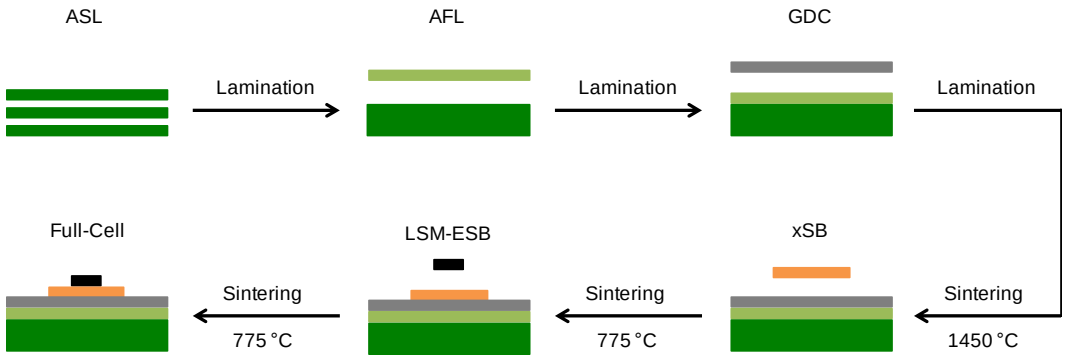


Figure 3-3 Schematic of bilayer SOFCs manufacturing procedure



Figure 3-4 Tape-caster (Procast, TC-71LC) used for fabrication of ASL, AFL, and GDC tapes

3.4.2 Bismuth Oxide Layer Deposition

In case of ceria/bismuth oxide bilayer electrolyte SOFCs, the second bismuth oxide layer electrolyte was deposited using different methods depending on the desired thickness. For a thin dense, 1-2 μm bismuth oxide layer, pulsed laser deposition (PLD) was implemented in this work. One of the key parameters in PLD is the substrate temperature for deposition and two different temperatures (450 and 600 °C) were

looked at with respect to the quality of the resultant bismuth oxide thin film including phase purity, density, and thickness. ASL/AFL/GDC half-cells described earlier were used as substrates and NGSB and YCSB pellets, made by conventional solid-state method, was used as PLD target for deposition. Targets were made by pressing 8-9 grams of powder in a ~ 28.6 mm cylindrical die. NGSB and YCSB pellets were then sintered at 800 ℃/2h and 1100 ℃/5h respectively. PLD Deposition was done in 100 mtorr of oxygen pressure using KrF laser beam (248 nm) of 22 mJ energy at 10 Hz frequency.

For bilayer electrolyte cells with a thicker bismuth oxide layer (≥ 2 μm), screen-printing was used. Bismuth oxide pastes were made by ball-milling the powders i.e. ESB, NGSB, YCSB in a 125 Nalgene bottle containing 5 mm spherical YSZ grinding media and ethanol. Following that, ethanol was successively evaporated and replaced by ESL441 binder (Electro-Science Laboratories) in a planetary centrifugal mixer (ARE-310 Thinky Mixer). The final ratio of the powder to ESL441 binder was controlled to be ~ 1:1. The obtained paste was then screen-printed (for a 4-10 μm layer) or blade-coated (for a 10-30 μm layer) on the electrolyte side of the half-cell, oven-dried for 5 hours, and then sintered at 775 °C for 2 hours with a 2 h step at 400 ℃ to burn out the binder. For GDC/NGSB bilayer electrolyte cells, thickness of the NGSB electrolyte layer was varied through multiple coatings of NGSB paste followed by sintering. However, for GDC/YCSB bilayer cells, thickness of the YCSB layer was adjusted by increasing the number of the stacked scotch tapes used as the mask during the blade-coating process.

3.4.3 Cathode Deposition

Deposition of the cathode on the electrolyte layer is the last step in the fabrication of the button cell. Cathode paste was made using the same method used for making the bismuth oxide electrolyte paste. The electron conductor phase i.e. LSM or $Bi_2Ru_2O_7$ (BRO7) and oxygen ion conductor phase i.e. ESB or YCSB were mixed in desired weight ratio and ball-milled in ethanol for 24 hours. Following that ethanol was successively evaporated and replaced by ESL441 binder (Electro-Science Laboratories) in a planetary centrifugal mixer (ARE-310 Thinky Mixer). The final ratio of the powder to ESL441 binder was controlled to be ~ 1:1. Cathode paste was finally blade coated, oven dried for 5 hours, and sintered at 775 °C for 2 hours to complete the anode supported bilayer fuel cell. Anode-supported single electrolyte and bilayer electrolyte button cells are shown in Figure **3-5**.

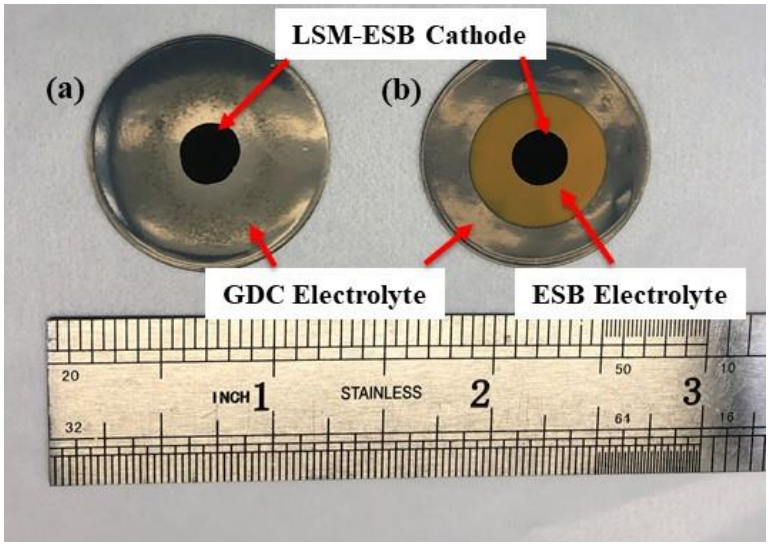


Figure 3-5 Fabricated anode supported (a) single GDC electrolyte, and (b) GDC/ESB bilayer electrolyte button cells

3.5 Electrochemical Testing of anode-supported button cells

For the electrochemical testing, button cells were sealed on an in-house built fuel cell test reactor using ceramic cements (Aremco 516 and 552). Gold (Electro-Science Laboratories) or platinum paste (Heraeus) were used to attach silver-mesh current collectors on the anode and cathode side, respectively. The cells were tested in air at the cathode and 97% H_2 / 3% H_2O at the anode using Solartron 1470E multichannel potentiostat and 1400A impedance analyzer. After securing the button cell and attaching the current collector mesh and wires, Ceramabond seal was initially dried at room temperature for 5 hours followed by curing steps at 94 ℃ and 265 ℃ each for 2 hours. To avoid thermal shock and cracking of the button cells, heating ramp rate was adjusted to 3 ℃ /min. Typical test protocol consisted of reduction of anode at 650 °C, followed by open circuit voltage (OCV), impedance, and I-V measurements of the cell across the temperature range of 650 to 500 °C. Following that, long-term stability studies of the cell were done under primarily open circuit condition with periodic impedance and I-V measurements at desired temperatures. Button-cell testing apparatus is shown in Figure **3-6**. All the lead wires are attached to Solartron 1470E potentiostat coupled with 1400 frequency response analyzer (FRA).

3.6 Post-testing Characterization

Following the completion of the electrochemical testing of the cells, microstructural features such as thickness and density of individual layers, adherence of adjacent layers together, and reactivity between electrolyte layers, were carefully examined using

scanning electron microscopy (SEM) (Hitachi SU-70 FEG) coupled with a Bruker EDS detector.

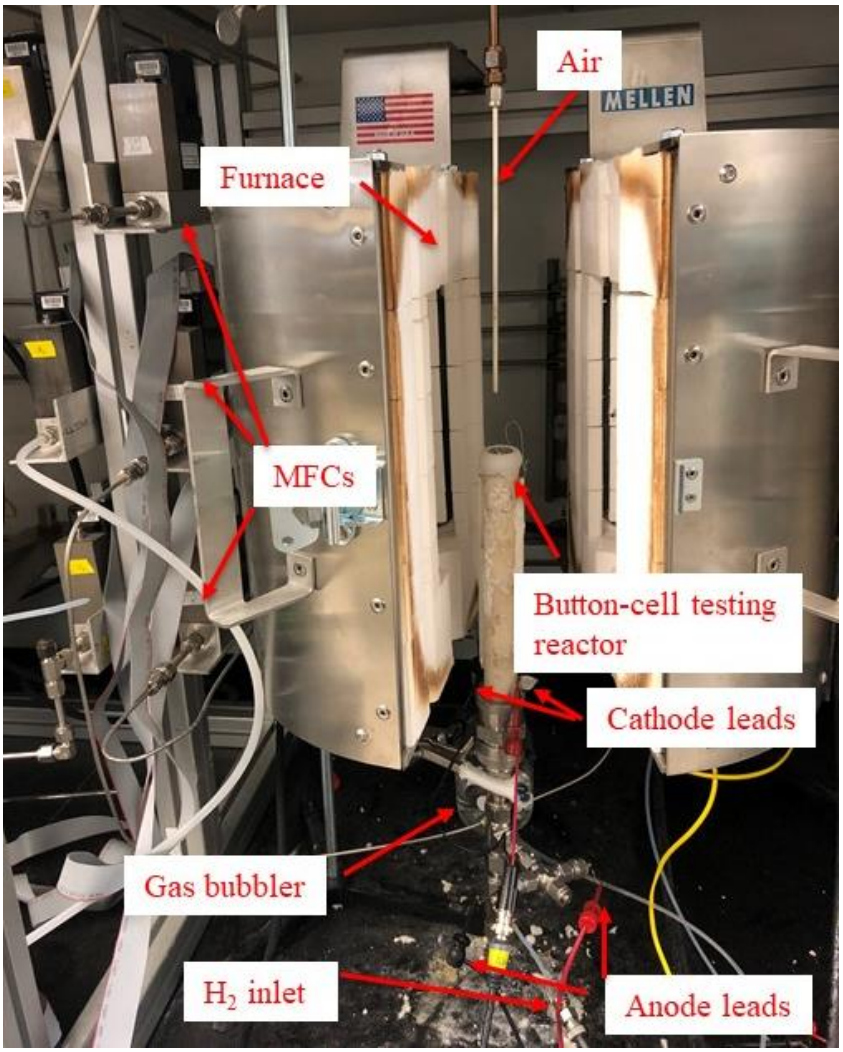


Figure 3-6 Button-cell I-V and impedance testing reactor

4 Development of Ceria/Rhombohedral Bismuth Oxide LT-SOFCs

As mentioned earlier, by reducing the operating temperature to low-temperature range (450-650 °C), commercialization of the SOFCs technology can be accelerated. Low operating temperatures allow the use of cheap metallic components, increase the stack lifetime, and shorten the start-up time of SOFCs [34-38]. Bilayer electrolytes based on doped ceria/stabilized bismuth oxide have been proposed as a measure to block the electronic leakage current in doped ceria [37, 44-51]. Stabilized bismuth oxide shows high ionic conductivity due to its high oxygen vacancy concentration and high mobility of anions [13-16]. However, stabilized bismuth oxide decomposes into metallic bismuth at oxygen partial pressure (p_{O2}) levels below 10^{-13} atm. and, hence, must be protected by the doped ceria layer against exposure to low p_{O2} side of the fuel cell. As outlined by Wachsman et al. [14], relative thickness as well as the transport properties of the two layers has a key effect on the interfacial p_{O2} value and, therefore, the electrochemical stability and any electronic leakage current of bilayer electrolyte based SOFCs.

Our group has been working on the development of several compositions of bismuth oxides stabilized with single dopant or multiple dopants for low temperature SOFCs. Traditional yttria stabilized bismuth oxide (YSB) or erbia stabilized bismuth oxide (ESB) exist in cubic phase and suffer from disorder-order transformation on the oxygen-ion sublattice at ~500 °C, resulting in conductivity decay with aging. On the other hand, a newly developed stabilized bismuth oxide composition doped with neodymium and gadolinium $(Bi_{0.92}Nd_{0.04}Gd_{0.04})_2O_{3\pm\delta}$ (NGSB) shows stable ionic

conductivity at ~500°C. Moreover, compared to bilayer SOFCs based on gadolinium doped ceria (GDC) and ESB, GDC/NGSB bilayer SOFCs have showed promising initial electrochemical results. In this chapter, we looked at GDC/NGSB bilayer cells more in detail – in particular, the effect of relative thickness and total thickness of GDC and NGSB layers on the electrochemical performance. Anode supported unit-cells of Ni-GDC/GDC/NGSB/LSM-ESB configuration with three different GDC thicknesses of ~20, ~40, and ~70 μm and different NGSB thicknesses (2-25 μm) were fabricated and tested under fuel cell conditions. The performance of the bilayer cells based on the OCV values and long-term stability was examined along with the microstructural analysis of the cells.

4.1 Experimental Details

Typical configuration of bilayer SOFCs consisted of ~600 μm NiO-$Ce_{0.9}Gd_{0.1}O_{2-\delta}$ anode support layer (ASL), ~20 μm NiO-$Ce_{0.9}Gd_{0.1}O_{2-\delta}$ anode functional layer (AFL), 20-70 μm $Ce_{0.9}Gd_{0.1}O_{2-\delta}$ first electrolyte layer, 2-25 μm NGSB second electrolyte layer, and 20-40 μm icnLSM-ESB cathode layer. The procedure to fabricate the bilayer SOFCs is schematically shown in Figure **3-3** and outlined in **section 3.4**.

NGSB powder was prepared by the standard solid-state method explained in **section 3.1.1** using Stoichiometric ratios of the dopant oxides including neodymium and gadolinium oxides (99.9% purity) and bismuth (III) oxide (99.99% purity, Alfa Aesar). NGSB electrolyte paste was then prepared by successive evaporation of ethanol and addition of ESL441 binder (Electro-Science Laboratories) in a planetary centrifugal mixer (ARE-310 Thinky Mixer). The obtained paste was blade-coated on the electrolyte side of the half-cell, oven-dried for 5 hours, and then sintered at 775 °C

for 2 hours. To vary the thickness of NGSB electrolyte layer, multiple coatings of NGSB paste were done followed by sintering. icnLSM-ESB cathode powder was prepared by *in situ* co-assembly method as described previously [78]. Cathode paste was made using the same method used for making the NGSB paste. icnLSM-ESB cathode paste was finally blade coated, oven dried for 5 hours, and sintered at 775 °C for 2 hours to complete the anode supported bilayer fuel cell. Sintering profiles for both NGSB and cathode layers included a step at 400 °C for 2 hours to burn out the binder. GDC and NGSB pellets were fabricated as outlined in **section 3.3.1**. Impedance spectroscopy was done on the symmetrical cells in air with oscillation voltage of 50 mV in frequency range of 0.1 Hz–10 MHz at temperatures between 325-725 °C using Solartron 1260 frequency response analyzer and ZPlot software (Scribner Associates). Over 15 bilayer cells were fabricated and tested, including duplicate cells, to characterize the effect of relative thickness and total thickness of the two electrolyte layers on cell performance. The details of electrochemical testing are explained in **section 3.5**.

4.2 Phase Composition of Ceria and Bismuth Oxide Electrolyte

Figure **4-1** shows the XRD patterns for GDC and NGSB powders. GDC powder was used as received from the manufacturer and NGSB powder was calcined at 800 °C for 16 hours was used for the analysis. XRD pattern of GDC indicated a single phase of cubic symmetry with Fm-3m space group, while the pattern for NGSB indicated a rhombohedral phase with space group R-3m (166). The lattice parameter for GDC and NGSB was estimated to be a = 5.4255 Å and a = 3.9737 Å, c = 27.718 Å, respectively, by Rietveld refinement using whole pattern fitting. XRD pattern of the NGSB thin film

deposited by PLD at 600 °C is shown in Figure **4-2**, showing intense peaks of NGSB indicative of the high crystallinity of the deposited thin film. Due to the low thickness of the NGSB film, GDC peaks with cubic symmetry from the underlying half-cells were also observed in the pattern.

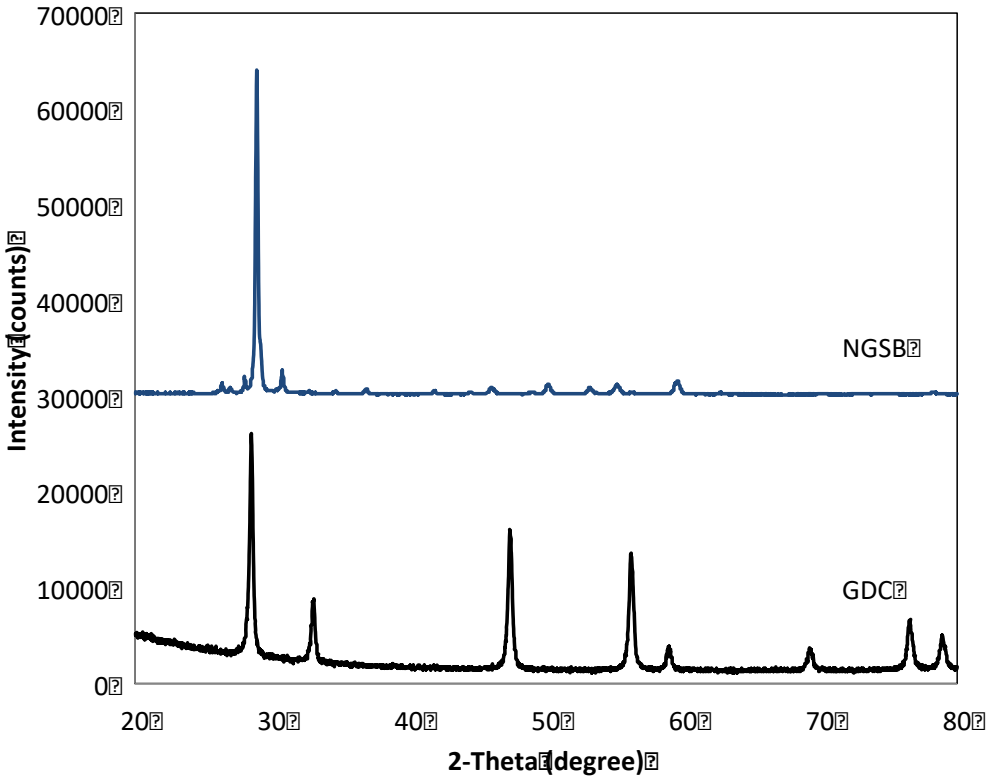


Figure 4-1 XRD pattern of GDC and NGSB electrolyte powders

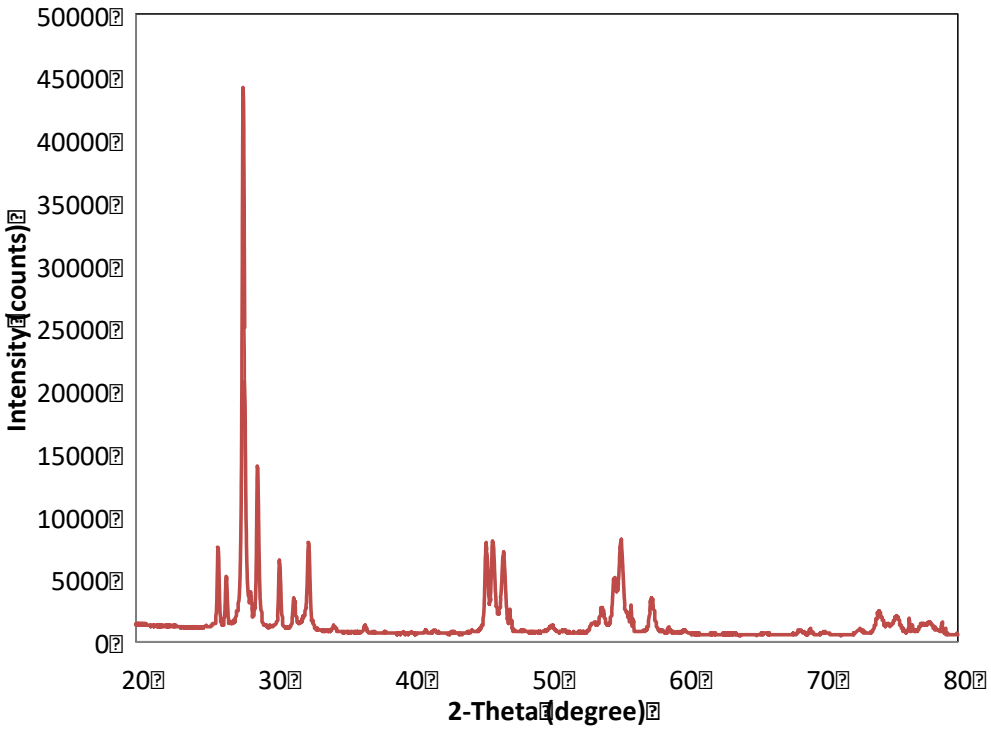


Figure 4-2 XRD pattern of thin film NGSB deposited by PLD on AFL/ASL/GDC half-cells

4.3 Electrical Conductivity of Ceria and Bismuth Oxide Electrolyte

Figure **4-3** shows the Arrhenius plots of grain, grain boundary, and total conductivity of GDC. Below ~425 °C, grain boundary conductivity was smaller than grain conductivity and effectively reduced the total conductivity of GDC. While above ~425 °C, the total conductivity is equal to the grain conductivity as the grain boundary conductivity was higher. Value of grain and total conductivity of GDC was 14.7 mS/cm at ~625 °C. Figure **4-4** shows the Arrhenius plots of total conductivity of NGSB during the heating/cooling cycles. Grain boundary contribution is not typically observed in the impedance spectra of bismuth oxide solid electrolyte due to the high conductivity of the grain boundaries, which was also found to be the case with NGSB. Total conductivity of NGSB at ~625 °C was 56.6 mS/cm, which is about four times higher

than that of GDC. The heating/cooling cycles of NGSB show a hysteresis loop due to the lag in the phase transformation between the low-temperature rhombohedral and high-temperature cubic phases. The symmetric cubic phase shows higher conductivity than the rhombohedral phase resulting in a decrease of conductivity at temperatures below ~625 °C. Conductivity of NGSB phase during the heating and cooling cycle at ~ 575 °C was 8.7 and 33.1 mS/cm, respectively.

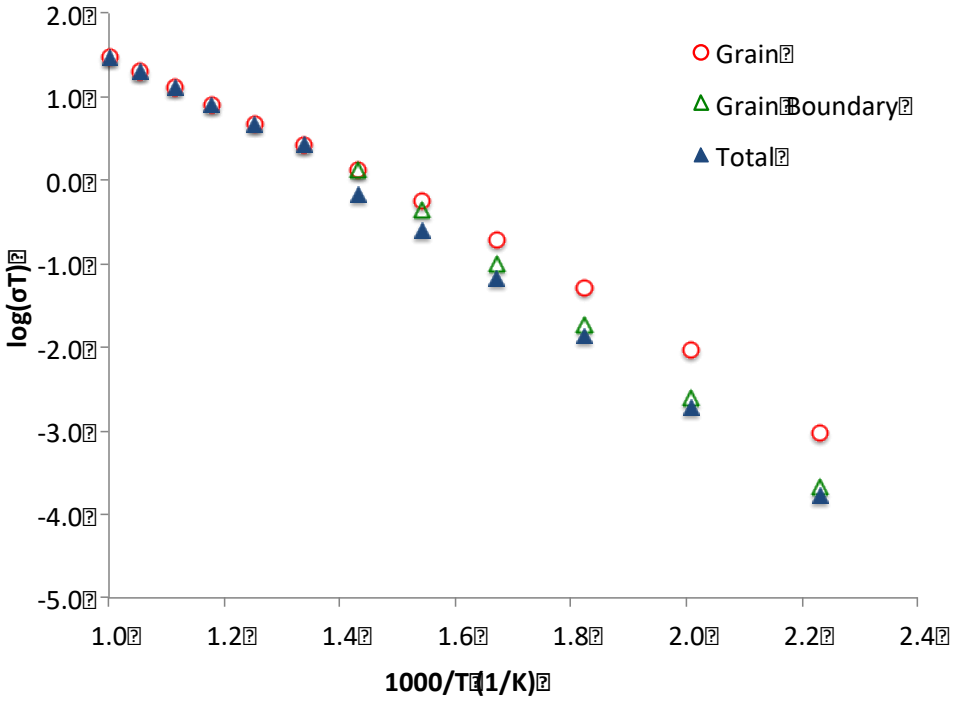


Figure 4-3 Arrhenius plot of grain, grain boundary, and total conductivity of GDC

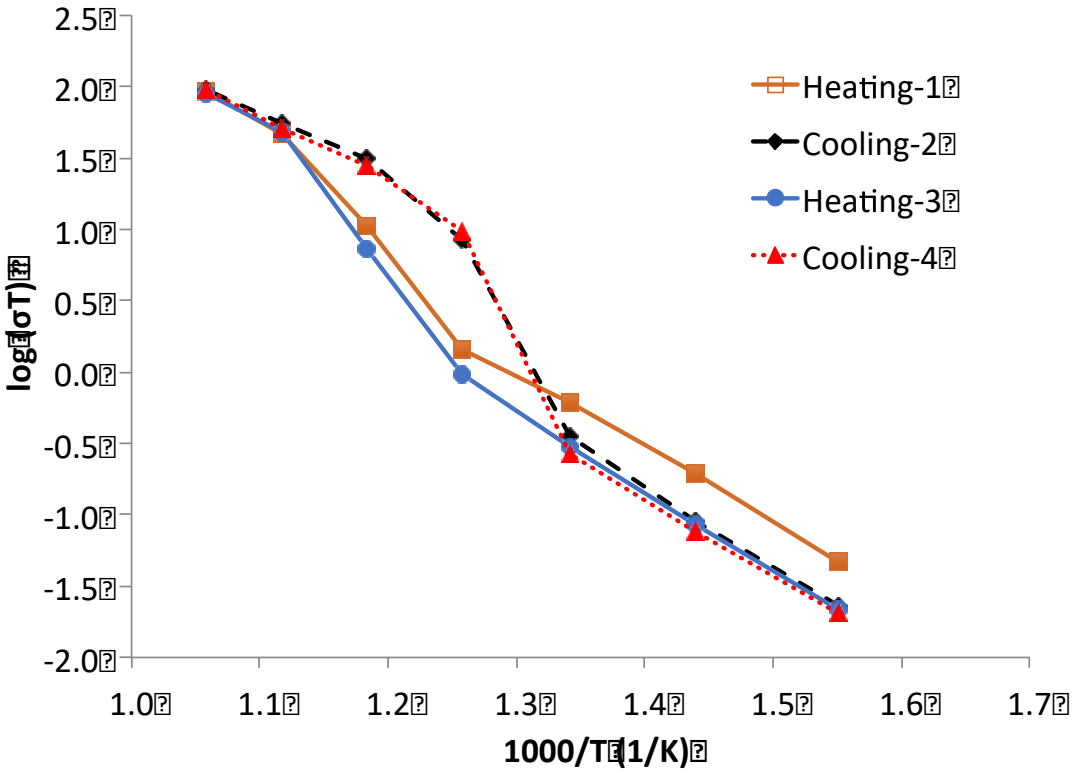


Figure 4-4 Arrhenius plot of total conductivity of NGSB with heating/cooling cycles

4.4 Microstructure of GDC/NGSB Bilayer Electrolyte SOFCs

Figure **4-5** shows the representative SEM micrographs of three GDC/NGSB bilayer samples, after fuel cell testing, with different GDC and NGSB thicknesses at two different magnifications. The left column shows a single layer ~23 μm GDC electrolyte cell with the icnLSM-ESB cathode, while the middle and the right columns show GDC/NGSB bilayer cells with thickness ratio of ~21 μm/ ~3.6 μm and ~39 μm/ ~22.3 μm, respectively. At low magnification, finer microstructure of AFL can be distinguished from the coarser microstructure of ASL. Thickness of AFL was ~20 μm and was kept constant across all samples. The GDC electrolyte layer thickness was varied between 20-70 μm and appears to be quite dense with some closed porosity. On

the other hand, NGSB layer showed asymmetric platelet-type grains due to the rhombohedral phase composition.

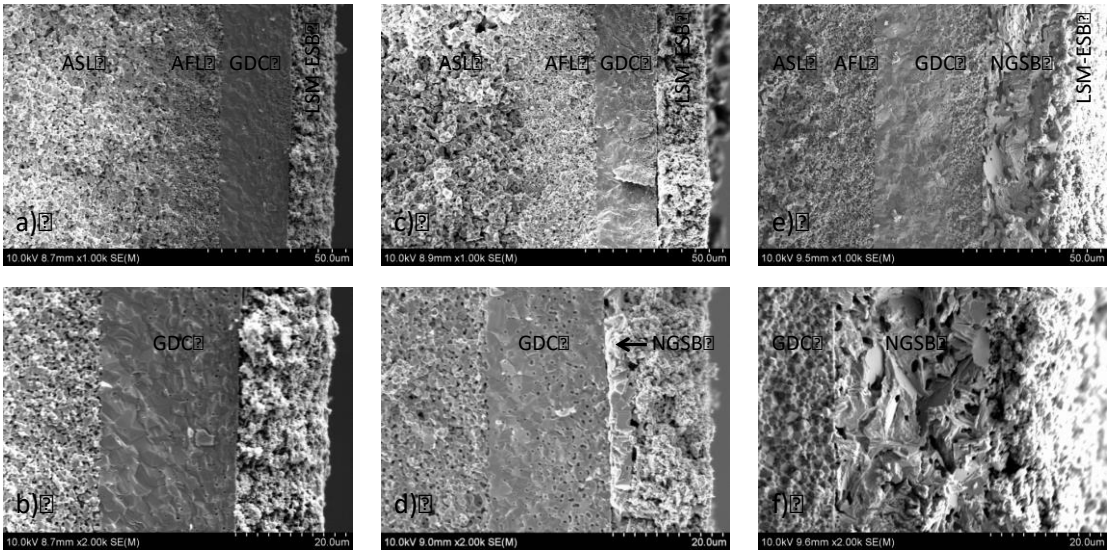


Figure 4-5 Representative SEM micrographs of ASL/AFL/GDC/NGSB/LSM-ESB cells at two different magnifications 1,000x and 2,000x – (a), (b) GDC (~23 μm); (c), (d) GDC (~21 μm) / NGSB (~3.6 μm); (e), (f) GDC (~39 μm) / NGSB (~22.3 μm)

Surface SEM images of the GDC and NGSB layers are shown in Figure **4-6**. The GDC electrolyte showed a dense top surface while the NGSB electrolyte showed some surface porosity. The interface of the GDC/NGSB bilayer was also examined by EDX line-scan which is shown in Figure **4-7**. The signal from Bi M_{α} peak increased, while the signal from Ce L_{α} peak decreased sharply at the GDC/NGSB interface, suggesting that there is no significant inter-diffusion of elements between GDC and NGSB layers. Results also showed that bismuth signal increases sharply at the surface of the cell confirming the deposition of NGSB thin film with a thickness of ~2 μm.

With increase in the PLD deposition temperature from 450 °C to 600 °C, the density and homogeneity of the NGSB thin film improved. The deposited PLD thin films were

examined using SEM and the micrographs of the NGSB film deposited at 600 °C is shown in **Error! Reference source not found.**.

Figure 4-6 Surface SEM micrographs on GDC and NGSB layers

The boundary of the NGSB thin film with GDC and LSM-ESB layers was clearly observable in the cross-section images. EDX elemental map on a thin film NGSB sample deposited at 600 °C are shown in Figure 4-9.

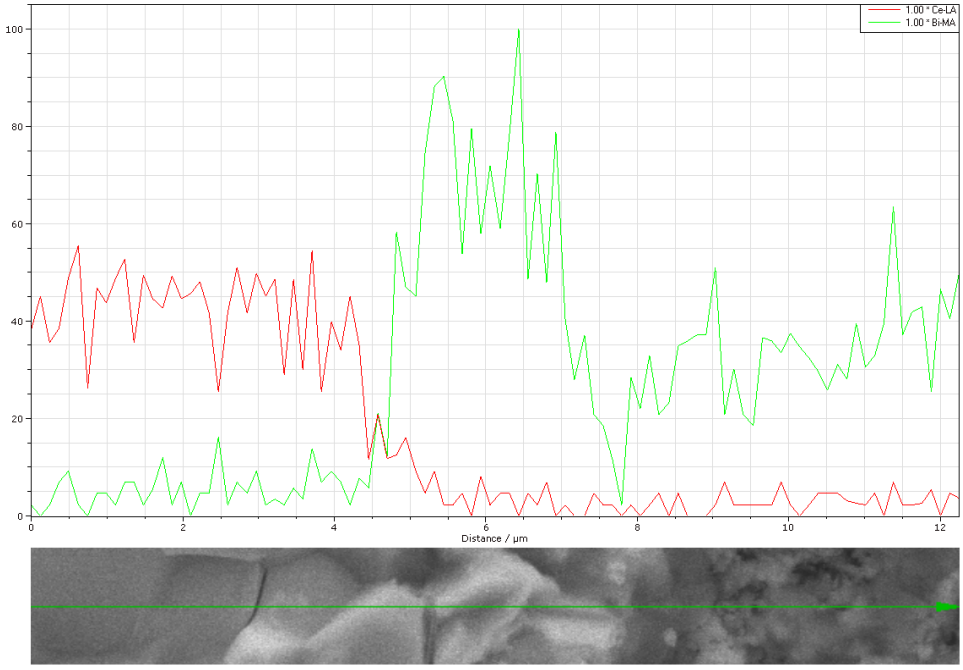


Figure 4-7 EDX line scan for GDC/NGSB interface; NGSB deposited by PLD at 600 ℃

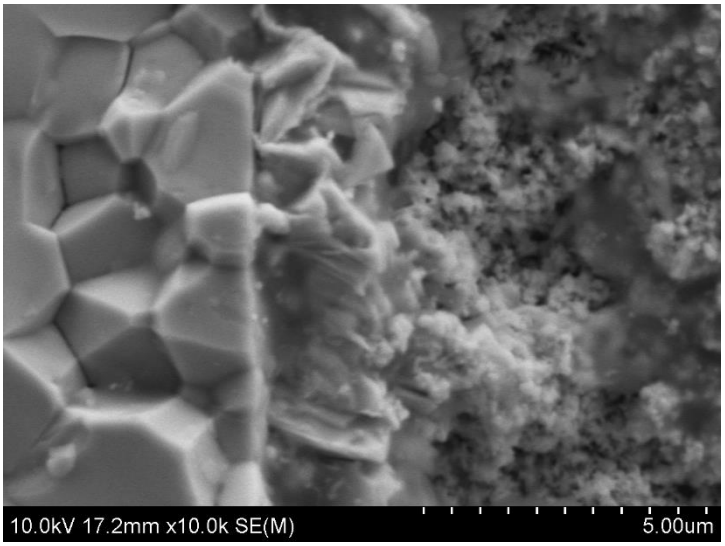


Figure 4-8 SEM micrographs on GDC/NGSB bilayer cells; NGSB deposited by PLD at 600 ℃

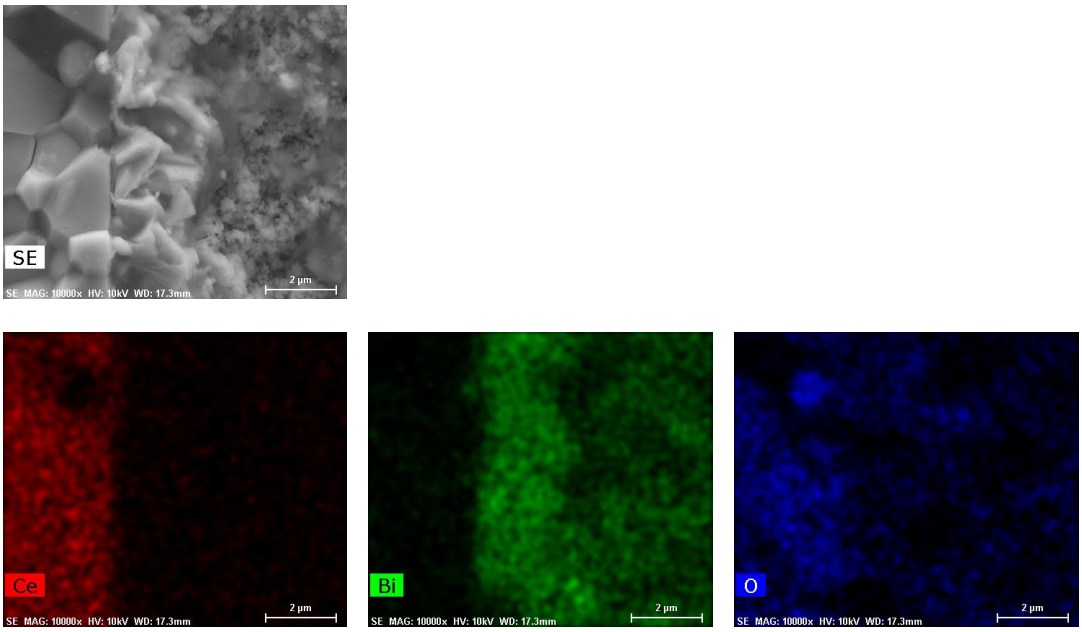


Figure 4-9 EDX elemental mapping scan for GDC/NGSB interface; NGSB deposited by PLD at 600 ℃

4.5 Electrochemical Performance

Electrochemical performance of GDC/NGSB bilayer cells at 500-650 ℃ is presented in Figure **4-10** and **Figure 4-11**. Figure **4-10** shows the effect of NGSB thickness on OCV for three GDC thicknesses – ~23, ~38, and ~78 µm, while Figure **4-11** shows the effect of GDC thickness on OCV for three NGSB thicknesses – 0, 3-9, 12-25 µm. The trend lines in the figures are guide to the eye to show the thickness dependence. The data set shows excellent repeatability between adjoining cells (cells with comparable thickness). Further, the time stability of GDC/NGSB cells, as described later in detail, adds to the quality of the presented data on GDC/NGSB cells.

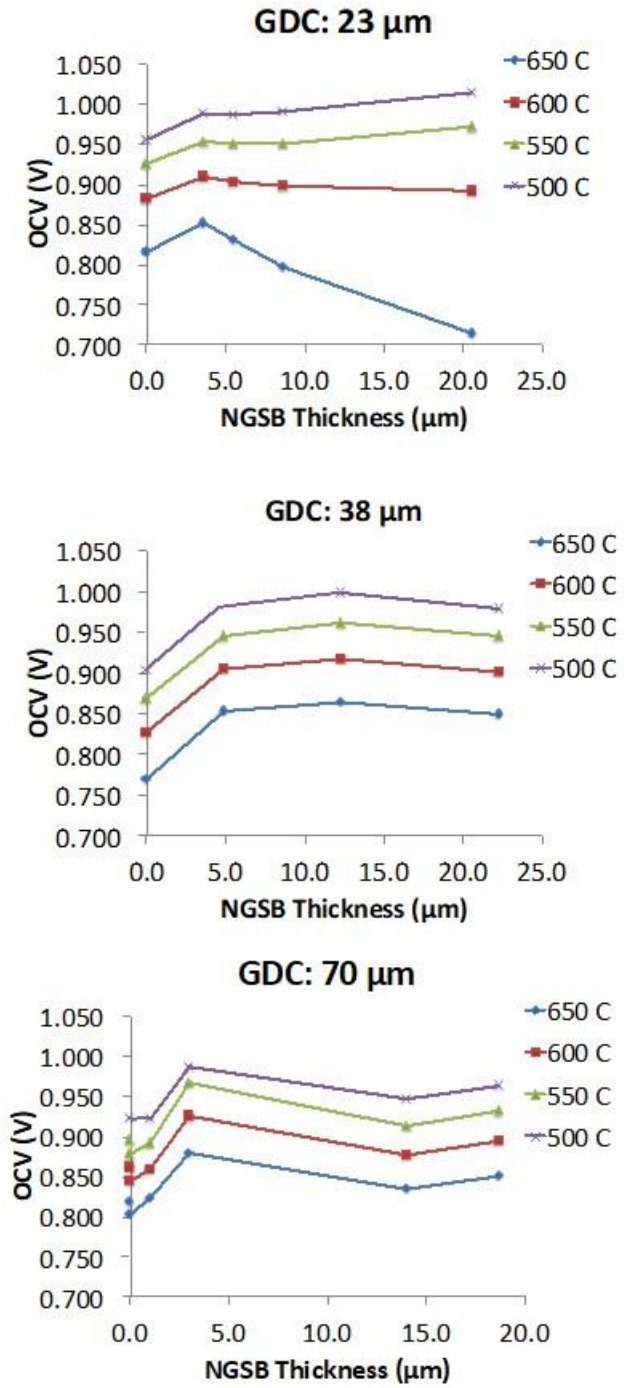


Figure 4-10 Effect of NGSB thickness on OCV for three GDC thicknesses – ~23, ~38, and (c) ~78 µm

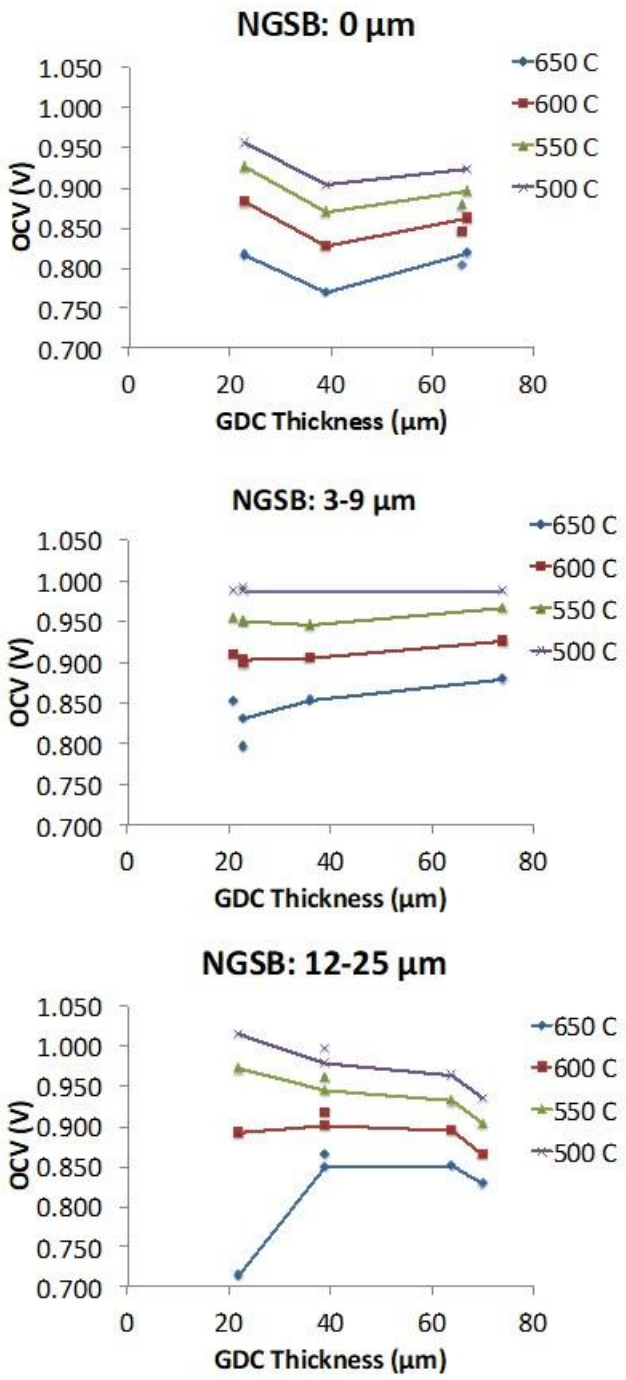


Figure 4-11 Effect of GDC thickness on OCV for three NGSB thicknesses (a) 0, (b) 3-9, (c) 12-25 µm

Figure **4-10** shows that the NGSB layer increased the OCV as compared to the baseline single layer GDC cell in all three cases of GDC electrolyte thicknesses - ~23, ~38, and ~78 µm. The different NGSB thickness dependence for the three cases of GDC suggests

that the OCV is both a function of GDC and NGSB thicknesses. Bilayer cells with low GDC electrolyte thickness (~23 μm) showed an increase in OCV with the addition of NGSB layer at temperatures between 500-550 ℃ and increase in NGSB thickness resulted in further increase in OCV compared to the baseline single layer cell. OCV of ~23 μm GDC cells at 500 ℃ with NGSB thickness of 3.6, 5.5, 8.6, and 20.6 μm, was 0.988, 0.987, 0.991, and 1.014 V, respectively. OCV at 600 ℃ showed an initial increase and then reached a plateau with increase in NGSB thickness. However, at 650 ℃, OCV first increased and then decreased with increase in NGSB thickness, suggesting that high NGSB/GDC thickness ratio may not be optimal at high temperatures. On the other hand, OCV of bilayer cells with ~38 and ~78 μm GDC showed a relatively flat relationship with NGSB thickness, suggesting a stable OCV increase on addition of NGSB layer at all temperatures. OCV of ~38 μm GDC and 12.3 μm NGSB cell was 0.998 V at 500 ℃. It can be further observed that OCV of bilayer cells based on thicker 78 μm GDC cell has a smaller temperature dependence compared to that of the thinner GDC bilayer cells.

OCV of bilayer cells with thin film NGSB deposited by PLD is also shown in Figure **4-10**. As expected, OCV increased on addition of ~2 μm NGSB layer compared to the baseline single layer GDC cell within the thickness range of 60 μm. However, the OCV was lower than that of bilayer cell with >3 μm NGSB layer, suggesting that thin NGSB film may not be optimal. Furthermore, the fabrication cost of thin film NGSB bilayer by PLD is higher than that of the bilayer cell with thicker NGSB made by conventional ceramic processing techniques.

Figure **4-11** shows that OCV of baseline single layer GDC cell; the variability in the dataset likely indicates the variability in the fabrication of the baseline cells and the test methodology. At 3-9 μm thickness range of NGSB, OCV increased with increase in GDC thickness, particularly at 650 ℃, indicating the beneficial effect of GDC layer in the bilayer cell. At higher NGSB thickness (12-25 μm), the cell with lower GDC thickness (~23 μm) showed higher OCV compared to cells with higher GDC thickness at 500-550 ℃. These results indicate that bilayer cells with lower GDC thickness and higher NGSB thickness have the advantage at low temperature operation of both higher OCV and lower ASR (conductivity of NGSB is 2-4 times higher than that of GDC depending on temperature) compared to other bilayer cells.

As mentioned earlier, GDC/NGSB bilayer cells showed OCV performance with promisingly, low degradation rates. Figure **4-12** (a) and (b) show OCV of two bilayer GDC/NGSB cells with thickness ratio of ~23 μm/~9 μm and ~74 μm/~3 μm, respectively. The GDC (~23 μm)/NGSB (~9 μm) cell was tested at 500 ℃ for ~17 hours and then at 600 ℃ for ~47 hours, while the GDC (~74 μm)/NGSB (~3 μm) cell was tested at 600 ℃ for ~140 hours and then at 500 ℃ for ~140 hours. Both cells showed quite low OCV degradation rates at both temperatures with values of < 0.002% per hour at 500 ℃ and between 0.005-0.012% per hour at 600 ℃. The cell degradation rate was lower at 500 ℃ due to slower kinetics of the different degradation mechanisms at lower temperatures. At the end of the test totaling over 420 hours, OCV of the GDC (~74 μm)/NGSB (~3 μm) cell dropped by 2.9% at 500 ℃ and by 2.4 % at 650 ℃, indicating the exceptional electrochemical stability of the anode supported GDC/NGSB bilayer cells.

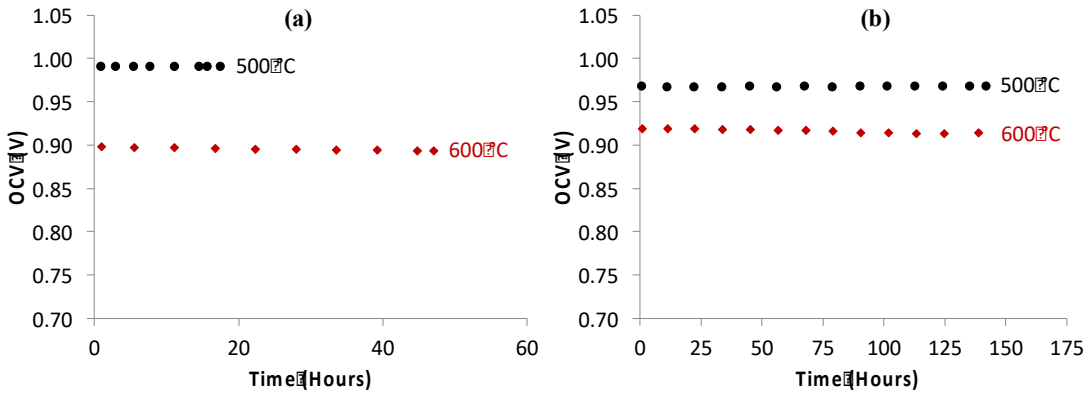


Figure 4-12 Open circuit voltage stability of (a) GDC (~23 µm)/NGSB (~9 µm) and (b) GDC (~74 µm)/NGSB (~3 µm) bilayer cells at 500 ℃ and 600 ℃

I-V and power density curves of a GDC/NGSB bilayer cell with ~20 µm thick GDC layer and ~4 µm thick NGSB layer in the temperature range of 500-650 ℃ are shown in Figure **4-13**. OCV of this cell at 650 ℃ was 0.85 V but decreased significantly on lowering the temperature, possibly due to presence of microcracks or loss of sealing. However, the area specific resistance (ASR) of the cell was not affected significantly with value of 0.191 and 0.173 Ωcm^2 at 600 and 650 ℃, respectively, which resulted in maximum power density of 0.61 and 1.06 W/cm^2 at 600 and 650 ℃, respectively.

To summarize, effect of relative/total thickness of GDC/NGSB bilayers was studied and multiple cells with OCV ~1V at 500 °C were demonstrated.

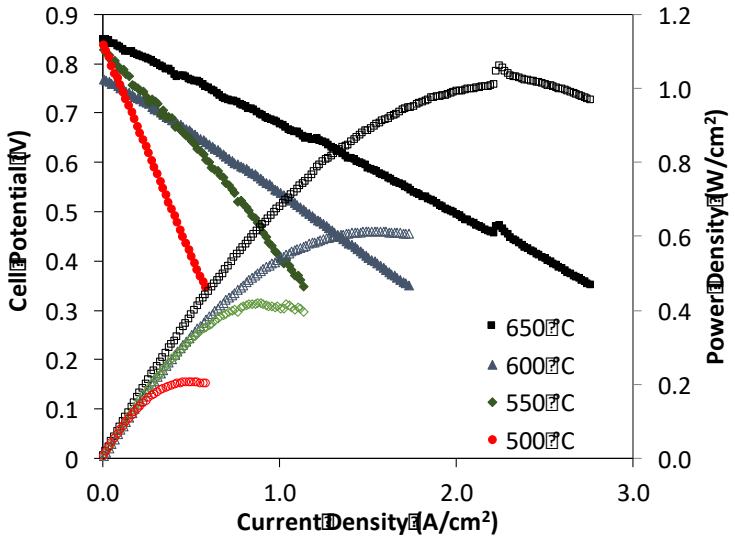


Figure 4-13 . I-V (filled symbols) and power density (open symbols) of GDC (~20 μm)/NGSB (~4 μm) bilayer cell at 500-650 °C

Although improvements in the cell OCV were demonstrated, and effect of thickness ratio on OCV of the cell was studied, since these cells suffered from typically high ASR values, the effect of thickness ratio on power density of GDC/NGSB bilayer electrolyte SOFCs was not explored.

Following a series of developmental works to modify the fabrication process and testing protocol, ASR of the cells was significantly reduced and hence a more thorough investigation on effect of thickness ratio on the performance of the cells became feasible. In addition, YCSB, a cubic bismuth oxide composition which showed superior thermodynamic stability in terms of OCV and electrical conductivity across the temperature range of 650-500 °C was used as the second electrolyte layer. More details regarding this bilayer system will be outlined in the following chapters.

5 Development of a New Ceria/ Yttria-Ceria Double Doped Bismuth Oxide Bilayer Electrolyte Low-Temperature SOFC with high Electrochemical Stability

As mentioned earlier, bilayer electrolytes based on doped ceria/stabilized bismuth oxide have been first demonstrated by Wachsman et al. [37, 44-51] as a measure to block the leakage current through the ceria layer and combine two low-temperature high-conductivity electrolytes which cannot be used individually in an SOFC environemnt efficiently. As outlined by Wachsman et al. [14], relative thickness as well as the transport properties of the two layers have a key effect on the interfacial pO_2 value and, therefore, the electrochemical stability of bilayer electrolyte SOFCs. $(Er_2O_3)_{0.2}(Bi_2O_3)_{0.8}$ (ESB) is the most common bismuth oxide composition used in ceria/bismuth oxide bilayer SOFCs [14, 37, 44, 45, 47, 48, 50, 80, 81, 83, 109, 114]. Other compositions such as $(Y_2O_3)_{0.2}(Bi_2O_3)_{0.8}$ [14, 45, 46, 49, 51, 82] and double doped compositions such as Dy-W stabilized bismuth oxide (DWSB), Dy-Gd stabilized bismuth oxide (DGSB), Dy-Ce stabilized bismuth oxide (DCSB) [84] have been examined. All these compositions stabilize bismuth oxide in the cubic structure. However, these cubic structures, although initially show high ionic conductivity, typically suffer from anion-ordering and their conductivity rapidly decay below 600 ºC. Such conductivity decay has been attributed to the displacement of the oxygen ions from the center of cation tetrahedra (8c-sites) to the faces of the cation tetrahedra (32f-sites) in <111> direction which limits the mobility of oxygen ion vacancies when annealed under 600 ℃ [53, 54]. Since these bismuth oxide compositions are used as both the second electrolyte layer material and the oxygen ion conducting phase in the

cathode structure, conductivity decay increases the ohmic and non-ohmic area specific resistance (ASR) of the cell and results in major power density degradation.

The objective of this chapter is to develop a new ceria/bismuth oxide bilayer electrolyte SOFC whith an alternative bismuth oxide composition that does not suffer from conductivity decay and evaluate its thermodynamic (as the second electrolyte) and conductivity (ohmic and non-ohmic ASR) stability at the cell level.

Huang et al. [56, 57] developed a bismuth oxide composition co-doped with Y_2O_3 and CeO_2, i.e., $(Bi_{0.75}Y_{0.25})_{1.86}Ce_{0.14}O_{3\pm\delta}$ (YCSB) that showed a stable ionic conductivity of 0.1 $S.cm^{-1}$ upon annealing at 600 ℃ for over 300 hours. Anode-supported half-cells with gadolinium doped ceria (GDC) / bismuth oxide (YCSB) bilayer electrolytes were fabricated and the performance and stability of the cells in terms of both ohmic ASR and OCV was compared to the bilayer cell using the traditional ESB. Additionally, YCSB was also used as the ionic conductor phase in the cathode structure and the non-ohmic ASR stability of the cell was evaluated and compared to the cell using ESB. Electrochemical stability of the cells was tested at the order-disorder transition temperature of ESB (600 ℃) and also a temperature above the ordering temprature (625 ℃).

5.1 Experimental

Powder synthesis - NiO (Alfa Aesar, 99%) and $Ce_{0.9}Gd_{0.1}O_{1.95-\delta}$ (GDC10-HP, Fuel Cell Materials) were used as received. YCSB powder was synthesized using both solid-state and sol-gel methods as outlined in section **3.1.1** and section **3.1.2** respectively. ESB was synthesized using solid-state route and calcined at 800 ℃ for 2 hours. For

cathode either $Bi_2Ru_2O_7$ (BRO) [76, 133] or LSM (Fuel Cell Materials) was used as the electronic conductor phase. BRO7 was synthesized using solid-state route. Stoichiometric amounts of bismuth oxide (Alfa Aesar 99.9995%) and ruthenium oxide (Alfa Aesar 99.99 %) were mixed in a mortar and pestle for 30 minutes and then calcined at 900 ℃ for 10 hours. After calcination, BRO7 powder was leached with dilute nitric acid and rinsed with deionized water and dried at 100 ℃ overnight.

Conductivity measurement – The electrical conductivity of YCSB was measured by impedance method (**section 3.3.3**) on symmetrical cells consisting of YCSB pellet sandwiched between gold electrodes (**section 3.3.1**). The obtained conductivity for YCSB was compared to other bismuth oxide compositions such as ESB and DWSB.

Anode-supported cell fabrication and testing- A typical anode-supported bilayer SOFCs consisted of ~600 μm NiO-GDC (60:40) anode support layer (ASL), ~20 μm NiO-GDC anode functional layer (AFL), 20 μm GDC first electrolyte layer, ~10 μm stabilized bismuth oxide second electrolyte layer, and 20-40 μm cathode layer. Experimental details on fabrication of anode-supported half-cells are given in **section 3.4.1.**

The second electrolyte layer was deposited using blade coating method. YCSB and ESB pastes were synthesized following the procedure outlined in **section 3.4.2**. The obtained paste was then blade-coated on the electrolyte side of the half-cell, oven-dried for 5 hours, and then sintered at 775 ℃ for 2 hours.

Three composite cathode systems were examined in this work: (a) LSM-ESB, (b) LSM-YCSB, and (c) BRO7-YCSB. All cathodes had the same weight ratio of the electronic conductor phase to ionic conductor phase (40:60). Cathode pastes w

ere fabricated using the same procedure as the electrolyte paste and deposited on the second electrolyte layer by blade-coating, oven-dried for 5 hours and sintered at 775 ℃ for 2 hours.

Fabricated cells were tested using the apparatus and methods described in **section 3.5**. Initially anode of the cell was reduced at 650 ℃. After full reduction of NiO, open circuit voltage (OCV), impedance, and power density of the cell across the temperature range of 650 to 500 ℃ were measured. Following that, long-term stability studies of the cell were done under primarily open circuit condition with periodic impedance and I-V measurements for 50 hours at 600 ℃ and 50 hours at 625 ℃. As summarized in Table **5-1**, three button cells with different bismuth oxide compositions in both the electrolyte and cathode structure were fabricated and tested for electrochemical performance and stability.

Table 5-1 Compositions of the anode, electrolytes, and cathode for three tested cells

Cell	Anode	Electrolyte 1	Electrolyte 2	Cathode
A (Baseline)	Ni-GDC (60:40)	GDC	ESB	LSM-ESB (40:60)
B	Ni-GDC (60:40)	GDC	YCSB	LSM-YCSB (40:60)
C	Ni-GDC (60:40)	GDC	YCSB	BRO-YCSB (40:60)

Characterization- Phase purity of the different compositions was analyzed using XRD (Bruker D8). Microstructure of the cells, including thickness of individual layers, adherence of electrolytes to the adjacent electrodes, and sinterability of the bismuth oxide pastes was examined using SEM (Hitachi SU-70 FEG).

5.2 Results and Discussion

5.2.1 Phase Purity

Figure **5-1** shows the XRD patterns for YCSB powder made by solid-state and calcination at 900 and 950 ºC and sol-gel powder calcined at 600 and 800 ºC. XRD patterns for solid-state powder showed shoulder peaks (marked with red marker lines), adjacent to cubic bismuth oxide peaks, which matched with yttrium cerium oxide reference pattern ($Y_{0.1}Ce_{0.9}O_{1.95}$, PDF 75-0174). The impurity phase was attributed to the incomplete reaction between the dopant oxide and bismuth oxide. As shown in Figure **5-1**, YCSB powder made by sol-gel method and calcined at 800 ℃ showed a pure cubic phase without any cerium oxide impurity. On the other hand, sol-gel YCSB powder calcined at 600 ℃ showed a tetragonal bismuth oxide phase.

The reactivity between LSM and YCSB as well as BRO7 and YCSB was studied using XRD. LSM and YCSB (sol-gel 800 ℃) in the weight ratio of 1:1 were mixed in the mortar and pestle and fired at 800 ℃ and 850 ºC for 10 hours. Figure **5-2** shows the XRD patterns for the mixture after annealing at 800 and 850 ℃ for 10 hours. No reaction between LSM and YCSB was observed at both temperatures which suggests LSM/YCSB could be used as the cathode for GDC/YCSB bilayer SOFCs in the temperature range of 650-500 ℃. Reactivity between BRO7 and YCSB is shown in Figure **5-3**. At 800 ℃ no reaction between BRO7 and YCSB was observed. However, at 850 ℃, formation of a tertiary cerium oxide impurity phase with peaks adjacent to the YCSB cubic peaks was observed. This indicates that BRO7 and YCSB composite electrode cannot be made by sintering at temperature higher than 800 ℃.

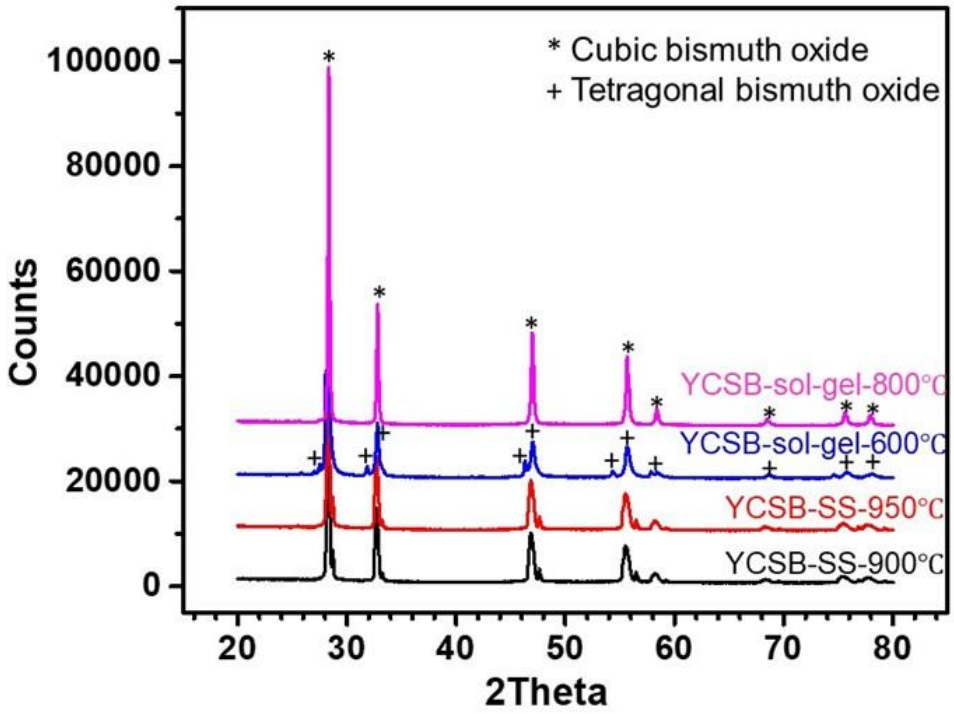


Figure 5-1 XRD patterns for YCSB powder synthesized by solid-state (SS) route calcined at 900 and 950 ℃, and sol-gel route calcined at 600 and 800 ℃

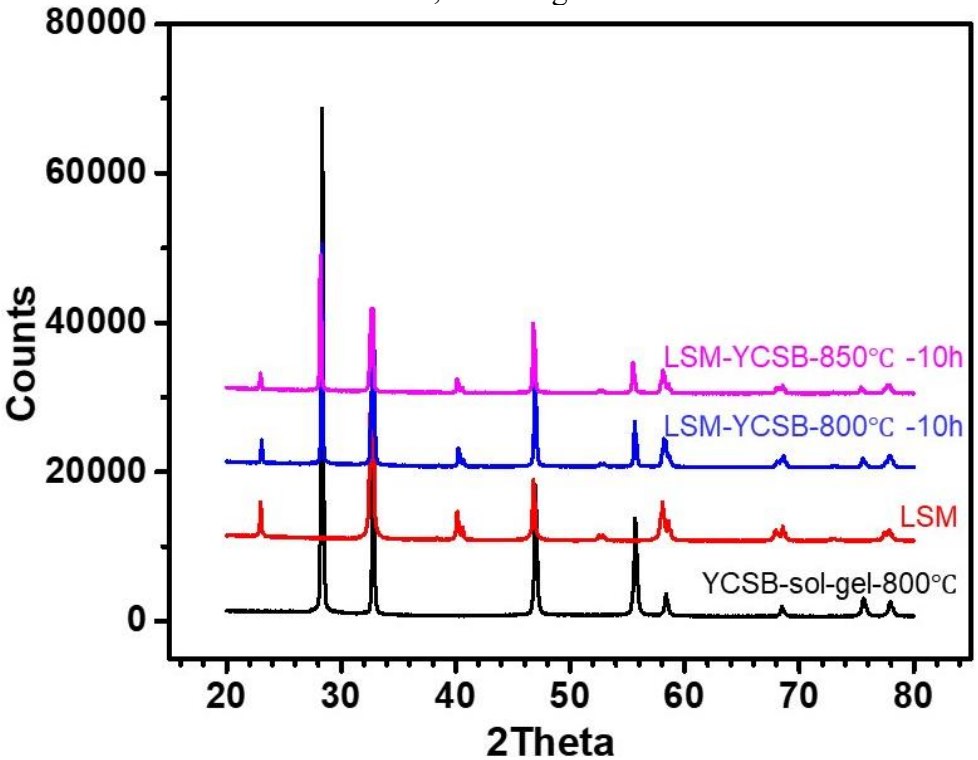


Figure 5-2 XRD patterns for LSM-YCSB mixture annealed at 800 ℃ and 850 ℃ for 10 hours

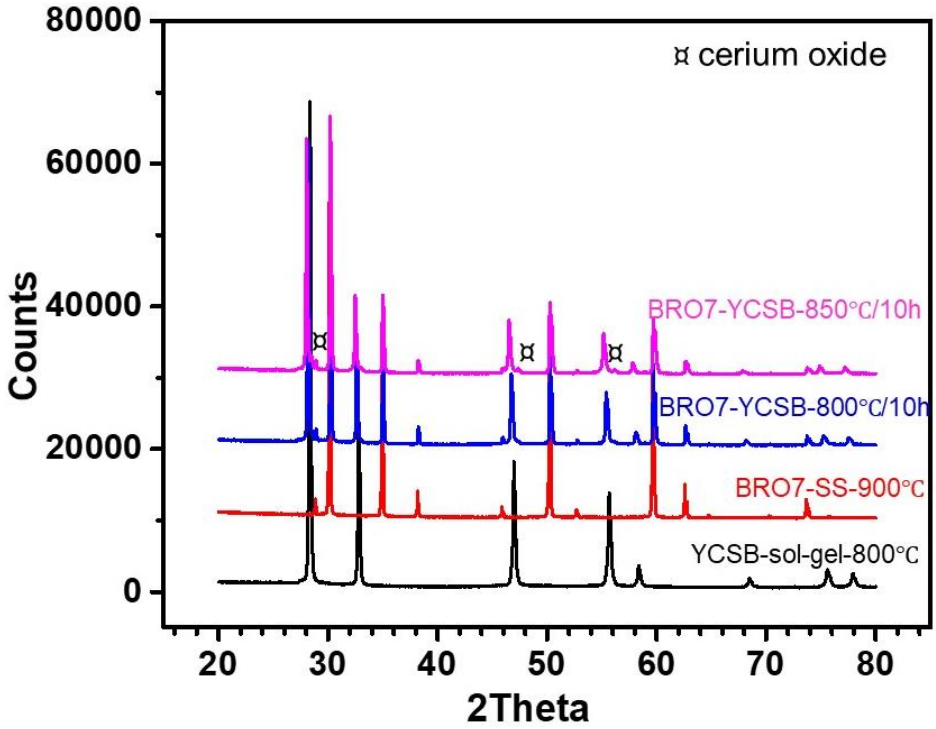


Figure 5-3 XRD patterns for BRO7-YCSB mixture annealed at 800 ℃ and 850 ℃ for 10 hours

5.2.2 Electrical Conductivity

Electrical conductivity of YCSB was measured across the temperature range 650-350 ℃. Similar to other bismuth oxide compositions, no grain boundary contribution was identified in the impedance spectra of YCSB. Due to the high conductivity of bismuth oxide grain boundaries. As shown by the Arrhenius plot in Figure **5-4**, YCSB conductivity did not show any change of slope, which indicates the absence of the ordering phenomenon typically observed for other cubic compositions such as ESB or DWSB [84]. Electrical conductivity of YCSB at 650, 600, 550, and 500 ℃, was 0.083, 0.054, 0.03, 0.011 $S.cm^{-1}$ respectively. The activation energy of YCSB over the temperature range of 650-350 ℃ was ~1.06 eV which was close to the value reported by Zhang and Huang (~1.05 eV), [57]. The stability of conductivity at 500, 600, and 650 ℃ was measured and compared against ESB and DWSB. As shown in Figure **5-5**,

at 500 ℃ YCSB showed a minor degradation of conductivity. In comparison, ESB and DWSB conductivity deceased by almost two orders of magnitude within the first 100 hours. The stability of conductivity at other temperatures are shown in Figure **5-6**. As can be seen, at higher temperatures, i.e. 600 and 650 ℃, no sign of conductivity decay was observed, suggesting the high stability of this bismuth oxide composition across the temperature range of 650-500 ℃.

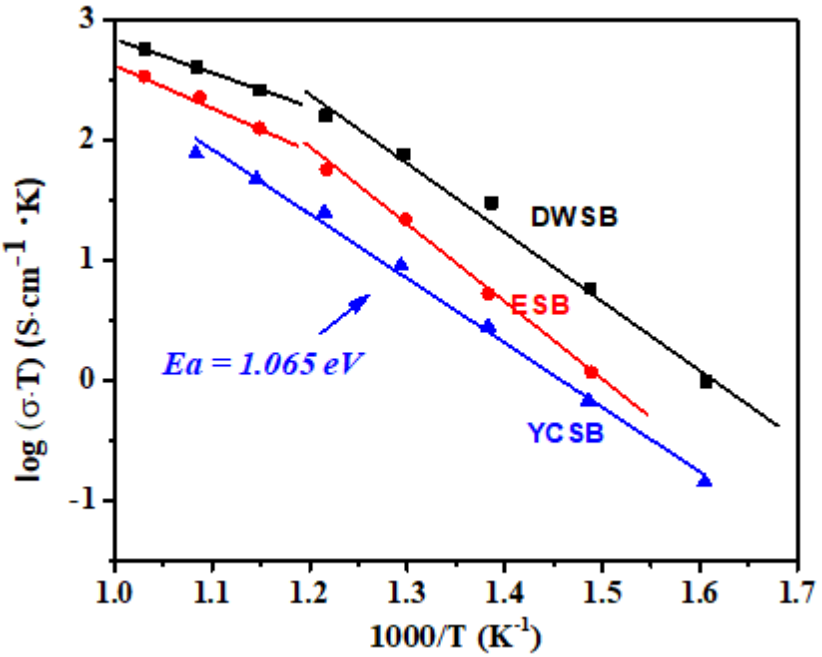


Figure 5-4 Arrhenius plot of ESB, DWSB, and YCSB electrical conductivity measured in air and under OCV condition across the temperature range of 650-350 ℃ using gold and silver mesh as current collector

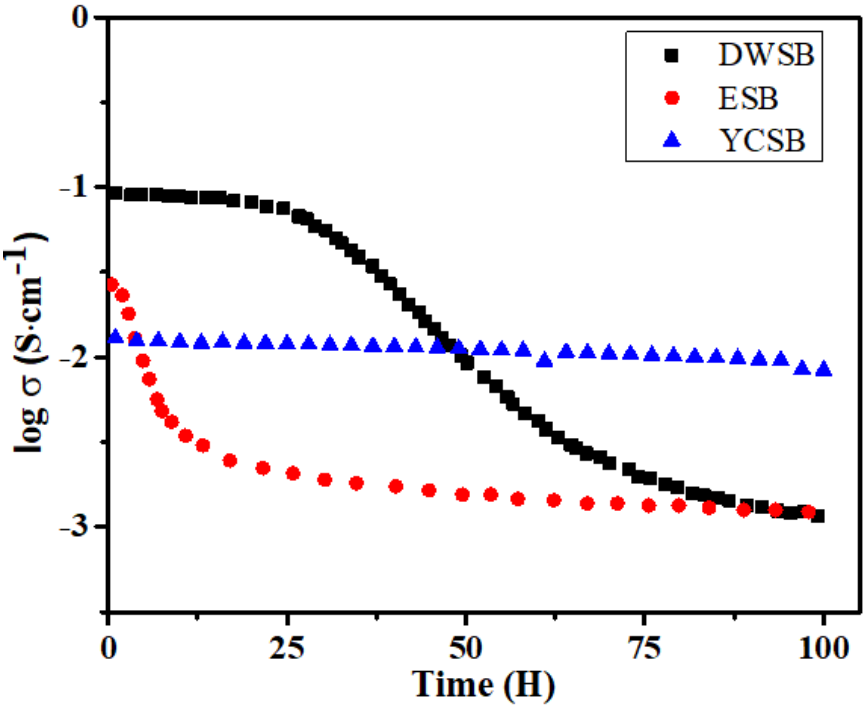


Figure 5-5 Stability of electrical conductivity of YCSB, ESB, and DWSB at 500 ℃

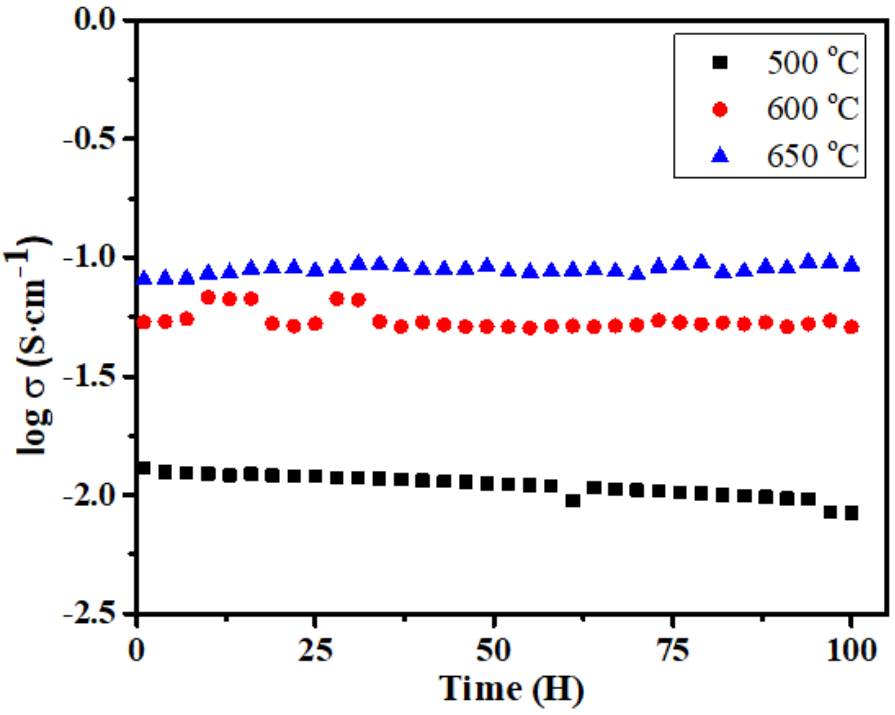


Figure 5-6 stability of electrical conductivity of YCSB at 500, 600, and 650 ℃

5.2.3 Microstructure

SEM micrographs for the interface of GDC/YCSB bilayer electrolyte samples are shown in Figure **5-7**. The top row shows the interface of the bilayer samples made by the YCSB powder synthesized from sol-gel route and sintered at 775, 825, and 875 ℃ for two hours. The bottom row shows the interface of the bilayer samples made by the YCSB powder synthesized from solid-state route and sintered at 775, 900, and 1000 ℃ for two hours. Increasing the sintering temperature, increased the density of the YCSB film for both the sol-gel and solid-state powders. On the other hand, due to the smaller particle size of the sol-gel powder compared to solid-state powder, denser YCSB layers were obtained at relatively lower temperatures. For instance, the bilayer sample with sol-gel YCSB powder sintered at 875 ℃ was denser than the sample made by solid-state YCSB sintered at 900 ℃. A similar density can only be achieved for solid-state YCSB by sintering at higher temperatures, e.g., 1000 ºC. However, increasing the sintering temperature induced significant intergranular fracture in the GDC layer, which would indicate an instability of the cell during long term operation. Therefore, 775 ℃ was chosen as the sintering temperature for preparing the YCSB layer using sol-gel powder.

The interface of the bilayer electrolyte sample sintered at 1000 ℃ for 2 hours was studied using EDX. The line-scan and elemental mapping of the interface are shown in Figure **5-8**. As indicated by the line-scan profiles, the signal from Bi Mα peak increased, while the signal from Ce Lα peak decreased and which implies no detectable inter-diffusion of elements between YCSB and GDC was observed which, in turn,

assures the absence of reaction between YCSB and GDC at lower sintering temperatures.

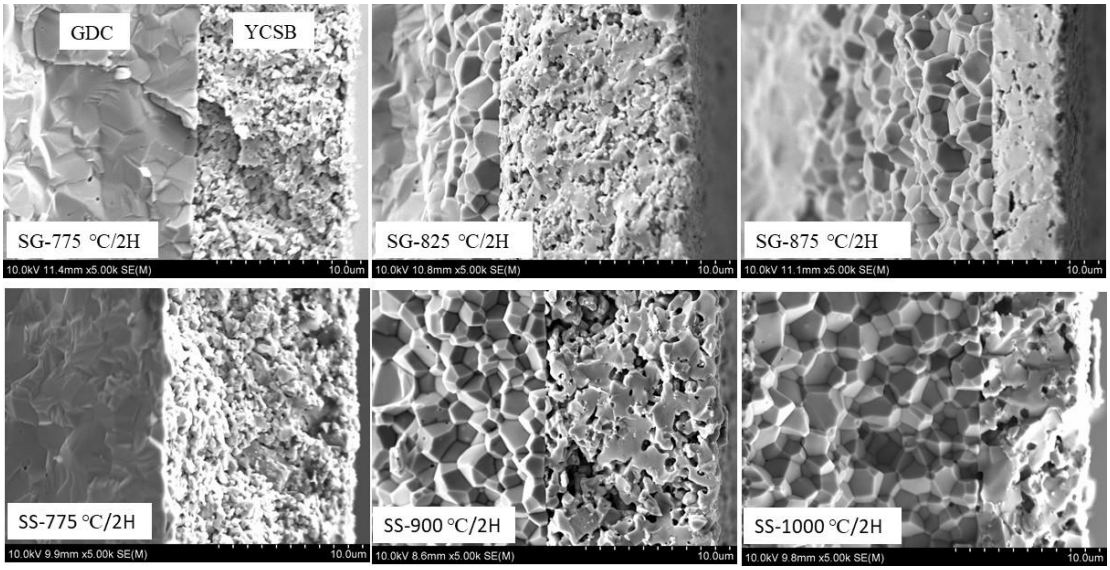


Figure 5-7 SEM micrographs of GDC/ YCSB (Sol-Gel) bilayers sintered at 775, 825, and 875 ℃ for 2 hours (upper row) and GDC/ YCSB(Solid-state) bilayers sintered at 775, 900, and 1000 ℃ for 2 hours (bottom row).

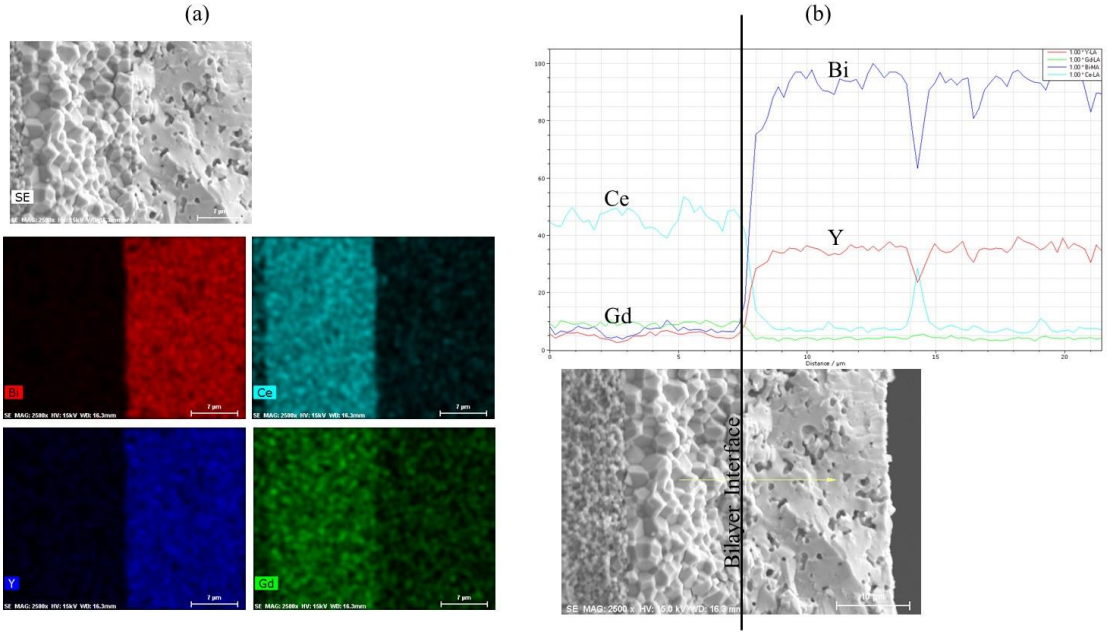


Figure 5-8 (a) EDX elemental mapping, and (b) line scan of GDC/YCSB bilayer interface sintered at 1000 ℃ for 2 hours

Figure **5-9** shows the microstructure of the NiO-GDC/GDC/ESB/LSM-ESB and NiO-GDC/GDC/YCSB/LSM-YCSB cells at three different magnifications after testing. Thickness of the GDC and bismuth oxide layers for both cells were ~ 20 μm and ~ 10-12 μm respectively. GDC layer was quite dense with no cracks or pinholes and adhered properly to the adjacent anode functional layer and secondary electrolyte (bismuth oxide layer). ESB electrolyte for the baseline cell was quite dense. However, YCSB electrolyte showed some porosity. The thickness of the AFL was constant for both cells and was approximately 20 μm. The finer grains of the AFL can be differentiated from the coarser grains of the ASL.

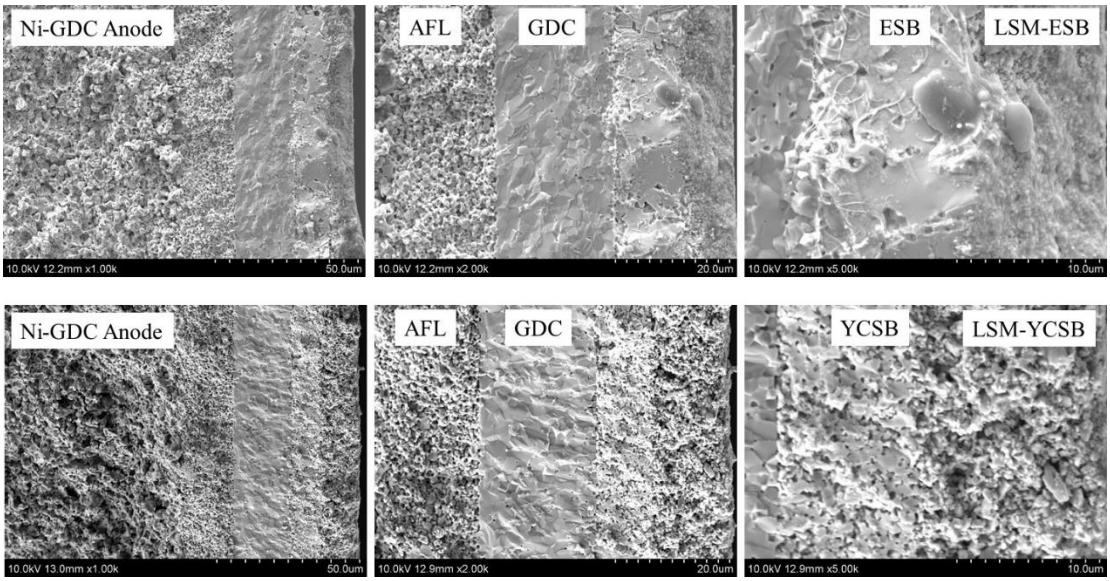


Figure 5-9 SEM micrographs of NiO-GDC/GDC/ESB/LSM-ESB baseline cell (top row) and NiO-GDC/GDC/YCSB/LSM-YCSB cell (bottom row)

5.2.4 Electrochemical Performance

Due to the voltage instability of Cell A at 650 ℃, anode reduction time was reduced to 30 minutes. Whereas, cells B and C were reduced at 650 ℃ for 2 hours. Following the initial reduction of the anode, impedance and power density of each cell were measured

across the temperature range of 650-500 ℃. I-V and power density curves for all three cells are shown in Figure **5-10**, Figure **5-11** and Figure **5-12**. Nyquist plots for all three cells across the temperature range of 650-500 ℃ are shown in Figure **5-13**.

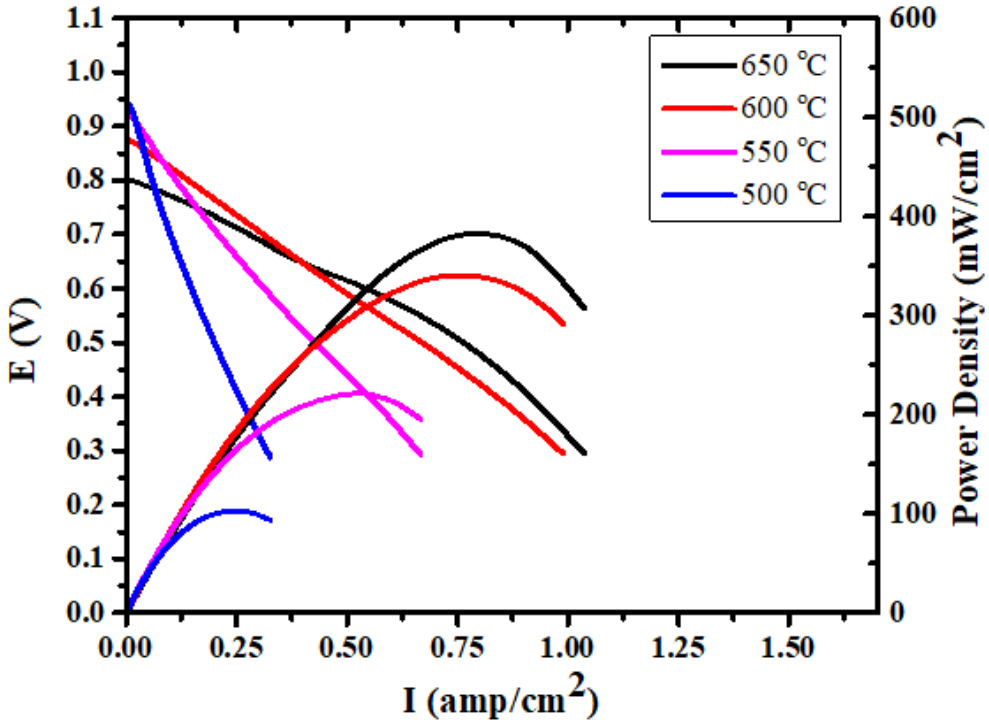


Figure 5-10 I-V and power density curves for cell A

At 650 ℃, both cells B and C with YCSB showed higher OCV compare to Cell A with ESB. OCV of cells A, B, and C at 650 ℃ reached 0.808, 0.833, and 0.853 V. As the temperature was reduced to 500 ℃, OCV of both cells with GDC/YCSB bilayer electrolyte reached over 1 V, higher than that of GDC/ESB cell (0.941 V). OCV of the cells with GDC/YCSB bilayer electrolyte was lower than that of values typically obtained with YSZ electrolyte (~ 1.1 v). However, due to the reduction of ohmic losses across the electrolyte, maximum power density (MPD) of cell B at 650 ℃ increased by 70 % compare to the cell with a 30-35 μm ScSZ electrolyte and same cathode (LSM-YCSB) [57].

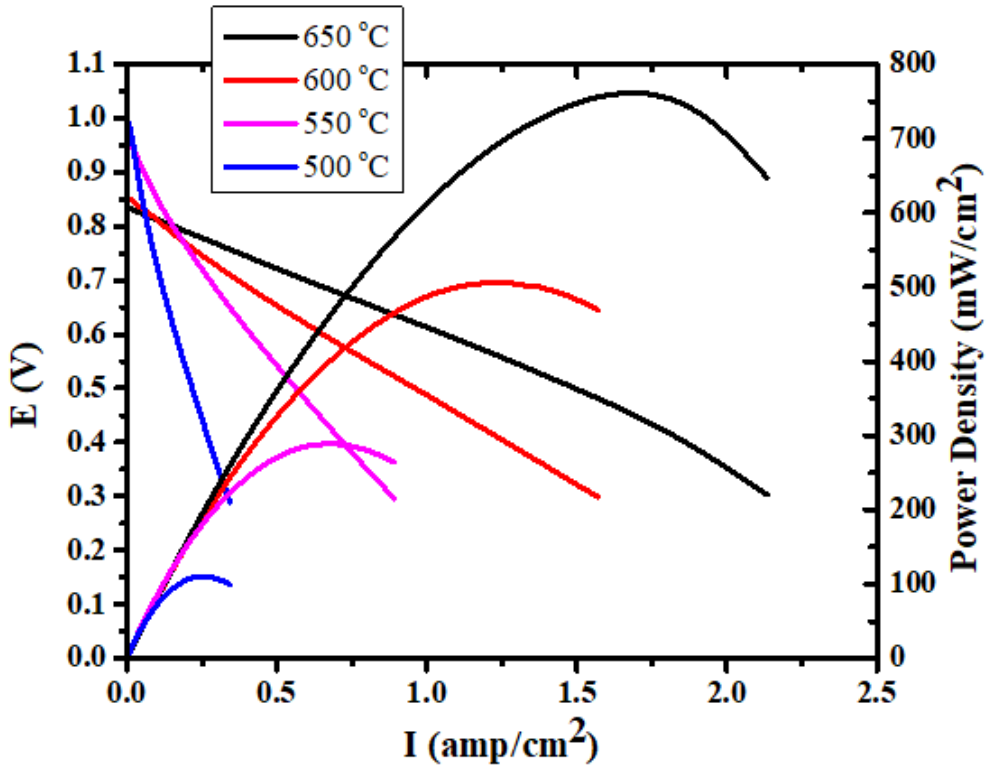


Figure 5-11 I-V and power density curves for cell B

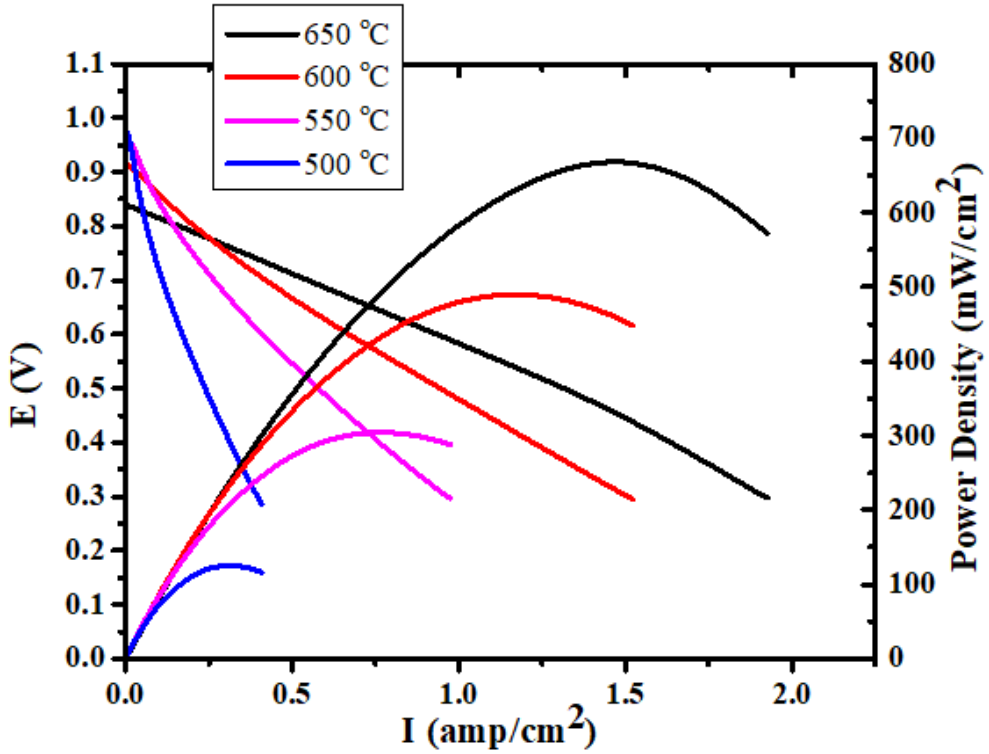


Figure 5-12 I-V and power density curves for cell C

Maximum power density of cells A, B, and C at 650 ℃ reached 380, 760, and 670 mW/cm^2. MPD of cell B at 650, 600, 550, and 500 ℃ was 760, 510, 290, and 110 mW/cm^2 respectively. Using an alternative cathode material (cell C, BRO7-YCSB) power density of the cell across the temperature range of 650-500 ℃ did not change significantly. However, cell A with GDC/ESB bilayer electrolyte showed significantly lower power densities across temperature range of 650-550 ℃. This is caused by the combined effect of lower OCV (Figure **5-10**), and higher non-ohmic ASR (Figure **5-13**) of cell A comparing to cells B, and C. The non-ohmic ASR of cell A at 650 ℃ (0.23 Ω.cm^2) was almost two times higher than cells B, and C (~ 0.11 Ω.cm^2). This is attributed to the inadequate reduction of NiO (30 minutes) comparing to the standard NiO reduction time for cells B, and C (2 hours). At 650 ℃, all three cells showed similar ohmic ASR of 0.1 Ω.cm^2. However, at lower temperatures (500 and 550 ℃) cell A with GDC/ESB bilayer electrolyte showed lower ohmic ASR comparing to cells B and C with GDC/YCSB bilayer electrolyte. This is mainly caused by the higher initial conductivity of ESB comparing to YCSB. At 500 ℃. All bilayer cells suffered from large non-ohmic ASR of ~ 4 Ω.cm^2 at 500 ℃, which resulted in low power density values. By optimizing the thickness ratio to balance between the higher OCV and lower ohmic losses, power density of the cell can be further enhanced. Additionally, nano-tailoring the cathode structure can reduce the non-ohmic ASR of the cell particularly at lower temperatures and boost the performance of the cell. The results of such efforts will be discussed in future chapters. OCV, MPD and ASR of the three tested cells across the temperature range of 650-500 ℃ are summarized in Table **5-2**.

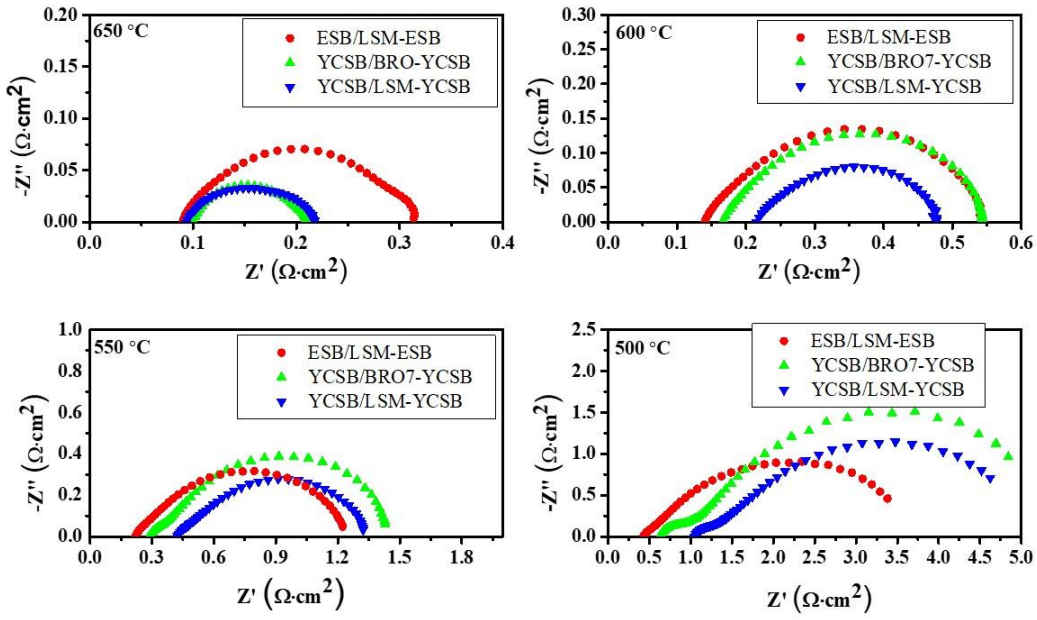


Figure 5-13 Nyquist plots for cells A, B, and C across the temperature range of 500-650 ℃

Table 5-2 Electrochemical performance of cells A, B, and C across the temperature range of 650-500 ℃

T (℃)	OCV(V)	MPD (w/cm^2)	Ohmic ASR (Ω.cm^2)	non-ohmic ASR (Ω.cm^2)	Total ASR (Ω.cm^2)
NiO-GDC/GDC/ESB/LSM-ESB (cell A)					
650	0.808	0.38	0.09	0.23	0.31
600	0.880	0.34	0.14	0.40	0.54
550	0.922	0.22	0.23	1.02	1.24
500	0.941	0.11	0.52	3.75	4.27
NiO-GDC/GDC/YCSB/LSM-YCB (cell B)					
650	0.833	0.76	0.10	0.11	0.21
600	0.861	0.51	0.21	0.27	0.48
550	0.973	0.29	0.42	0.90	1.32
500	1.034	0.11	1.057	4.71	5.77
NiO-GDC/GDC/YCSB/BRO7-YCB (cell C)					
650	0.853	0.67	0.08	0.12	0.20
600	0.919	0.49	0.17	0.37	0.54
550	0.982	0.30	0.29	1.14	1.43
500	1.018	0.12	0.63	4.98	5.61

5.2.5 Electrochemical Stability

Following the initial 650-500 ℃ measurement of performance, electrochemical stability of each cell in terms of OCV, and ohmic/non-ohmic ASR at 600 ℃ (order-disorder transition temperature of ESB), and 625 ℃ (above the ordering temperature) for approximately 50 hours (100 hours in total) was evaluated. Stability of OCV at 600 and 625 ℃ is shown in Figure **5-14**. At 600 ℃ OCV of cell A with GDC/ESB bilayer electrolyte decreased from 0.894 to 0.638 V within the first 25 hours of operation and then partially recovered to yield an average hourly degradation rate of -0.55 %/h. In contrast, cells B and C with GDC/YCSB bilayer electrolyte showed a much more stable OCV. Cell B with GDC/YCSB bilayer electrolyte and LSM-YCSB cathode showed absolutely no degradation (+0.1 %/h) and cell C showed minor degradation of OCV at 600 ℃ (-0.15%/h) possibly caused by the reactivity between BRO7 and YCSB as observed by the XRD patterns (Figure **5-3**). At the end of 50 hours, OCV for cells A, B and C at 600 ℃ were 0.658, 0.914, and 0.853 V respectively. At 625 ℃ cell A with GDC/YCSB bilayer electrolyte showed an initial degradation of OCV and subsequent increase that resulted in an hourly rate of +0.09%/ h change of OCV. Similar to 600 ℃, at 625 ℃, cell B with GDC/YCSB bilayer showed excellent OCV stability with zero degradation. OCV of cell C at 625 ℃ showed a degradation rate of approximately -0.09 %/h. OCV of cells A, B and C at the end of 50 hours annealing at 625 ℃ reached 0.643, 878, and 0.771 V respectively. Although both GDC/ESB and GDC/YCSB bilayer cells have same bismuth oxide to ceria thickness ratio, YCSB appeared to be much more stable and effective in blocking the leakage current through the ceria electrolyte.

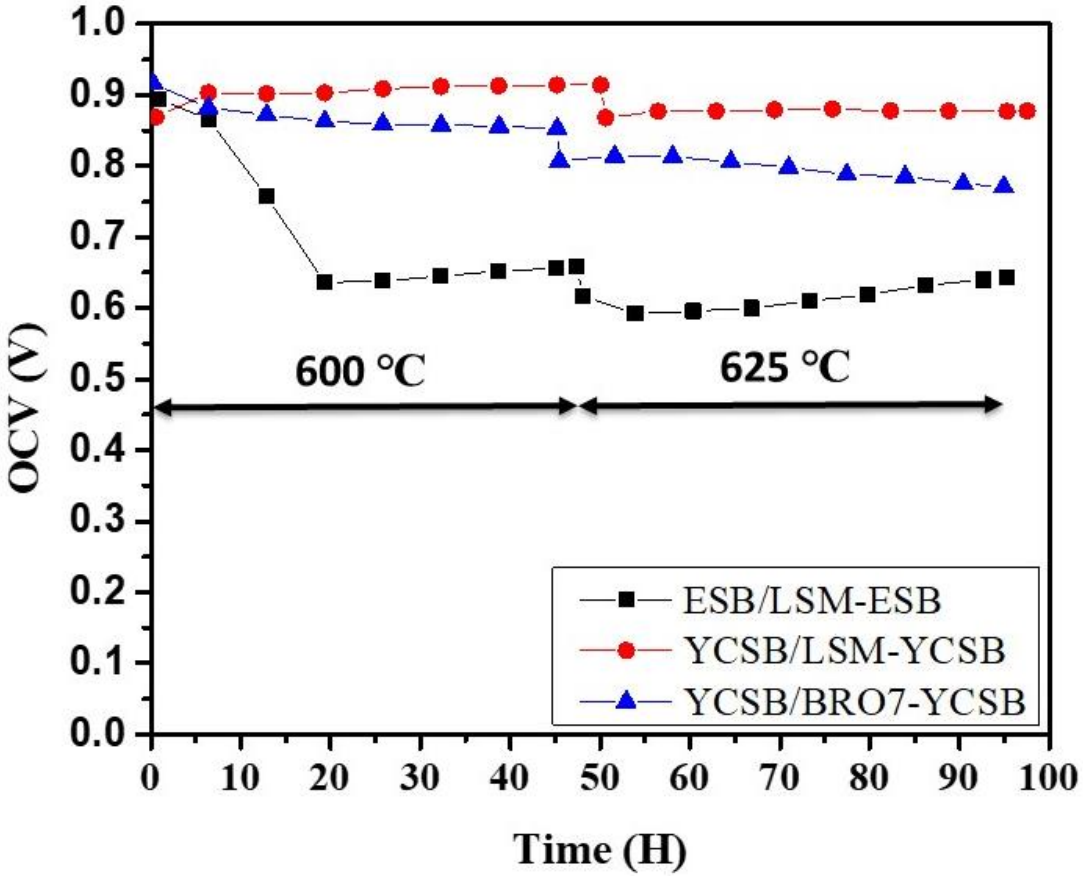


Figure 5-14 stability of NiO/GDC/ESB/LSM-ESB (Cell A), NiO-GDC/GDC/YCSB/LSM-YCSB (Cell B), and NiO-GDC/GDC/YCSB/BRO7-YCSB (Cell C) at 600 ℃, and 625 ℃

Ohmic and non-ohmic ASR stability of the cells A.B, and C at 600 and 625 ℃ are shown in Figure **5-15**, Figure **5-16**, and Figure **5-17** respectively. For cell A with GDC/ESB bilayer electrolyte and LSM-ESB cathode, both ohmic and non-ohmic ASR increased by almost 5 times over the first 50 hours of operation at 600 ℃. This is largely due to the ordering of ESB occurring at ~ 600 ℃ [53, 54]. By replacing ESB with YCSB (cell B) as both the secondary electrolyte material and also oxygen ion conducting phase within the cathode structure, ohmic and non-ohmic ASR stability of the cell was enhanced significantly. The ohmic ASR of cell B did not show any sign of degradation at 600 ℃ and non-ohmic ASR increased from 0.33 $\Omega.cm^2$ to 0.41 $\Omega.cm^2$

over the first 25 hours and then stabilized. Similarly, cell C with GDC/YCSB bilayer electrolyte and BRO-YCSB cathode showed very stable ohmic and non-ohmic ASR at 600 ℃. After approximately 50 hours of operation at 600 ℃ ohmic ASR of cells A, B, and C were 0.854, 0.198, and 0.191 $\Omega.cm^2$ respectively and non-ohmic ASR of the cells reached 0.682, 431, and 0.389 $\Omega.cm^2$, respectively. At 625 ℃ (above the order-disorder transition temperature of ESB) cell A still showed slight increase in ohmic and non-ohmic ASR while cells B and C did not show any sign of increase in the ohmic and non-ohmic ASR. Noticeably, implementing a bismuth oxide composition such as YCSB which does not suffer from ordering phenomena enhanced both ohmic and non-ohmic ASR stability of the ceria/bismuth oxide bilayer electrolyte cell.

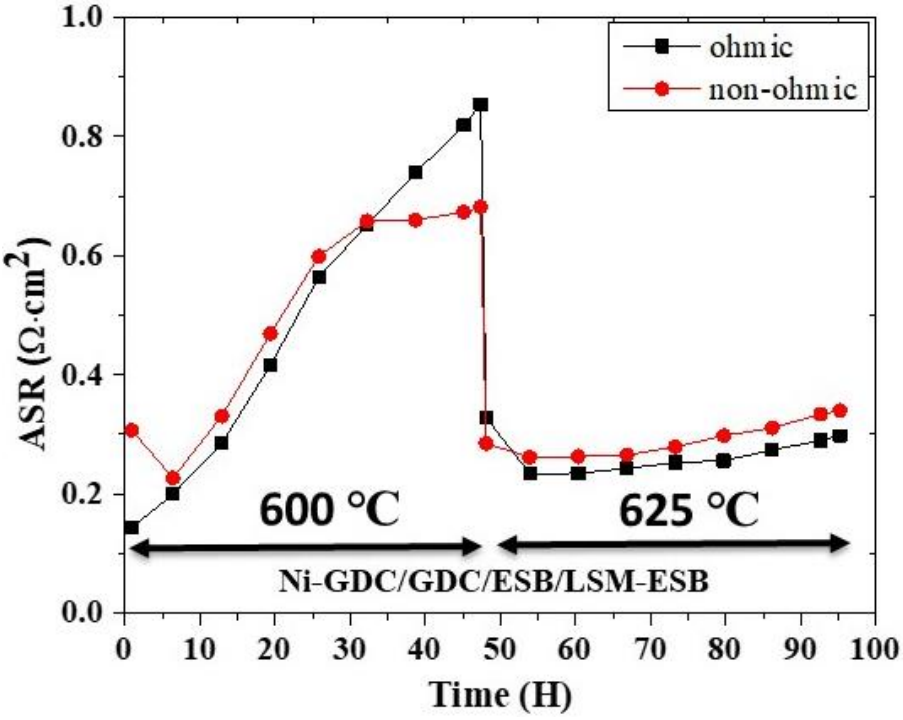


Figure 5-15 ohmic and non-ohmic ASR stability of NiO/GDC/ESB/LSM-ESB (Cell A) at 600 and 625 ℃

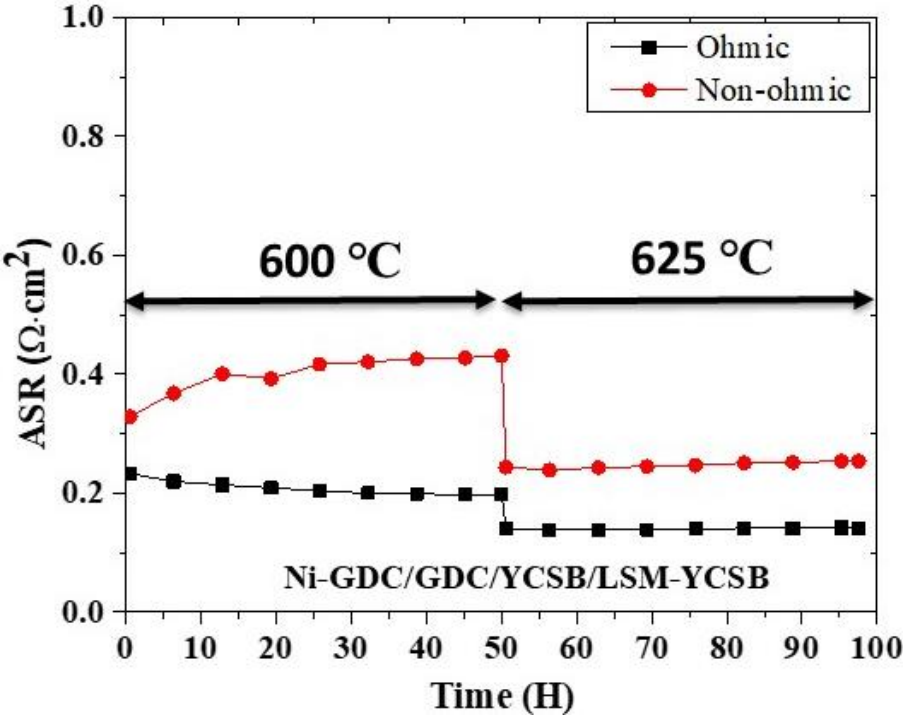


Figure 5-16 ohmic and non-ohmic ASR stability of NiO/GDC/YCSB/LSM-YCSB (Cell B) at 600 and 625 ℃

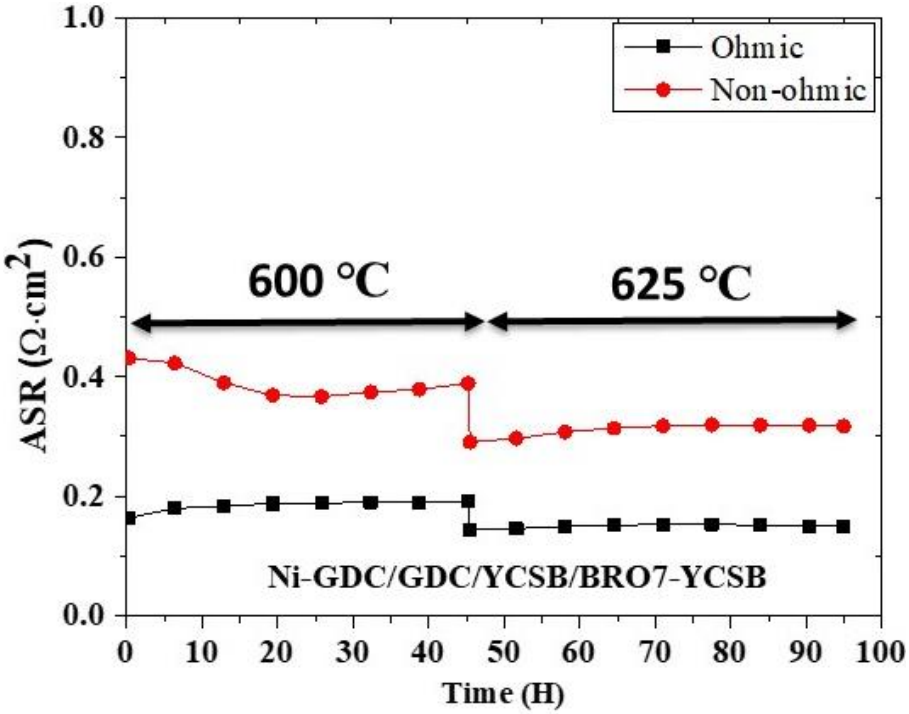


Figure 5-17 ohmic and non-ohmic ASR stability of NiO/GDC/YCSB/BRO7-YCSB (Cell C) at 600 and 625 ℃

The newly developed bilayer electrolyte SOFC showed an exceptional stability in terms of OCV, ohmic and non-ohmic ASR at 600 and 625 ℃ over 100 h, as comparing to the baseline cell with GDC/ESB bilayer electrolyte. As such, this newly developed bilayer electrolyte system will be used in future chapters of this work to study (a) the effect of ceria/bismuth oxide thickness ratio on the performance of the SOFC at different temperatures, and (b) developing high-performance SOFC for temperatures below 600 ℃.

6 Optimizing Bilayer Electrolyte Thickness Ratios for High Performing Low-Temperature Solid Oxide Fuel Cells

As mentioned earlier, the primary approach to reduce the operating temperature of SOFC is to reduce the ohmic loss across the electrolyte either by reducing the thickness of the electrolyte layer or using alternative electrolyte materials with higher ionic conductivity e.g. GDC, stabilized Bi_2O_3 etc.[14]. Conductivity of $Er_{0.2}Bi_{0.8}O_{1.5}$ (ESB) and GDC is 1-2 orders of magnitude higher than traditional YSZ electrolyte at 500°C, i.e., oxide ion conductivity of YSZ, GDC, and ESB is 0.0009, 0.0064, and 0.0242 S/cm, respectively [34]. GDC electrolyte based SOFCs under low pO_2 conditions at the anode side suffer from ceria reduction, which induces n-type electronic conductivity in the electrolyte, leading to electronic leakage current resulting in lower OCV and overall power output. On the other hand, a novel concept of ceria/bismuth oxide bilayer electrolyte, combining two low-temperature fast oxide-ion conductive electrolytes is beneficial for overall performance improvement of SOFCs to a new level. It was suggested that the partial electronic conduction in ceria layer was blocked by the bismuth oxide layer, while the ceria layer increased the oxygen partial pressure at the interface above the decomposition pO_2 of bismuth oxide. A critical factor determining the OCV and ohmic ASR of the ceria/bismuth oxide bilayer SOFCs is the ceria/bismuth oxide thickness ratio. Although few studies show the effect of ceria/bismuth oxide thickness ratio on OCV and transference number [14] [44] [48] [85], the primary focus of these works was concentrated on studying the effect of relative thickness ratio, ceria thickness and anode gas pO_2 on the OCV of the cell. Therefore, a systematic study relating the changes of ohmic ASR, OCV and power output of the SOFCs as a function

of thickness ratio of bilayer electrolyte needs significant attention for further technological advancements.

Primary objective of this chapter is concentrated on studying the effect of GDC thickness and GDC /bismuth oxide thickness ratio on the OCV and ohmic loss of anode-supported bilayer SOFCs. The well-known bismuth based electrolyte (ESB) undergoes ordering phenomena at tempertures ≤600°C, causing rapid decay in conductivity, and inturn the power output. As an alternative, GDC/YCSB bilayer electrolyte anode-supported SOFCs developed in the previous chapter which showed stable OCV and ohmic and non-ohmic ASR, was chosen for this study. Anode supported bilayer SOFCs with three different GDC thicknesses i.e. 10, 20, 40 μm and various YCSB/GDC thickness ratios for each GDC thickness were fabricated and tested across the temperature range of 650-500 °C using humidfied hydrogen and air as fuel and oxidant, respectively.

6.1 Experimental Details

Anode-supported GDC/YCSB bilayer electrolyte SOFCs were fabricated as described in **section 4.1**. The thickness of the GDC electrolyte was varied between 10 μm to 40 μm by adjusting the thickness of the green GDC tape during the tape casting process. To understand the effect of thickness ratio and total thickness of the two electrolyte layers on the performance of the cell i.e. MPD, OCV and ohmic losses across the electrolytes, over 15 cells with three different thicknesses of GDC electrolyte (10, 20, and 40 μm) and various YCSB/GDC thickness ratios ranging from zero (single electrolyte) to near 1 were fabricated and tested across the temperature range of 650-

500 ℃. Anode-supported GDC/YCSB bilayer electrolyte SOFC is schematically shown in **Figure 6-1**.

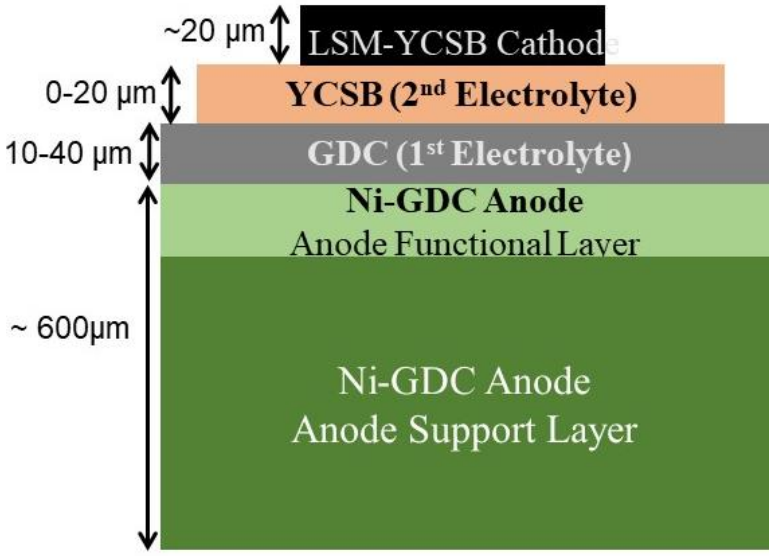


Figure 6-1 Schematic of anode-supported GDC/YCSB bilayer electrolyte SOFCs

All samples were sealed on an in-house built fuel cell test reactor using ceramic cements (Aremco 571). Gold paste (Electro-Science Laboratories) was used to attach silver-mesh current collector on both the anode and cathode sides. All SOFCs (anode) tested in this study were first reduced at 650 ℃ for 2 hours followed by open circuit voltage (OCV), impedance, and I-V measurements of the cell across the temperature range of 650 to 500 ℃. Ohmic and non-ohmic ASR of all the cells were measured using electrochemical impedance spectroscopy (EIS) with oscillation voltage of 50 mV in frequency range of 0.1Hz - 10 MHz across the temperature range of 650-500 ℃.

6.2 Results and Discussion

Electrolytic domain of GDC and thermodynamic stability of bismuth oxide is determined by partial pressure of oxygen in that layer. As shown in **Figure 6-2**, and

outlined by Wachsman et al [14], bismuth oxide/ceria thickness ratio controls the average partial pressure of oxygen in both electrolyte layers, and thus can affect both the OCV and ohmic ASR of an SOFC. For SOFCs with single MIEC electrolyte (**Figure 6-2** (a)) such as GDC the OCV depends on the thickness of electrolyte, as the ionic transference number of GDC increases with thickness [134, 135]. However, increasing the thickness of GDC increases the electrolyte ohmic resistance, affecting the power output significantly. A second electrolyte layer on GDC (**Figure 6-2** (b)) facilitates enhancement of the OCV without compromising the ohmic resistance, due to its ionic transference number close to unity (almost purely ionic conducting in nature) and much higher oxide-ion conductivity compared to MIEC type GDC. Ionic conductivity of stabilized bismuth oxide is approximately one order of magnitude higher than GDC (e.g., at 500 °C, ionic conductivity of YCSB and GDC is 0.011 and 0.0064 S/cm, respectively). Further, optimizing the bismuth oxide/GDC thickness ratio influences the ohmic losses across the electrolyte, hence, an optimum GDC electrolyte thickness and bismuth/GDC thickness ratio is a tradeoff between minimum ohmic losses (thinner electrolyte) and enhanced OCV (thicker electrolyte) which can enhance the power output of the cell considerably.

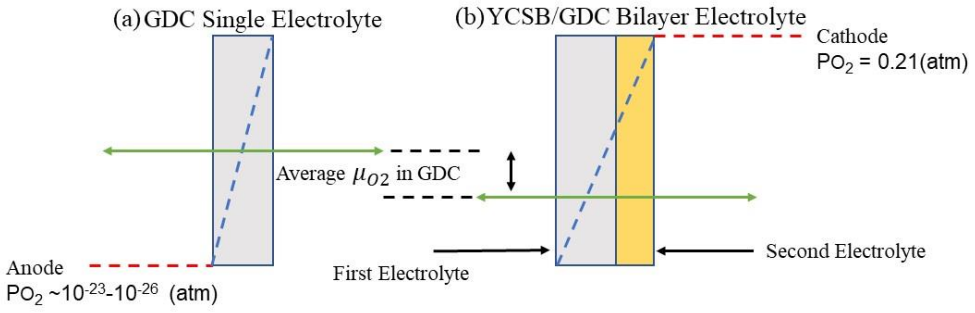


Figure 6-2 Schematic of a YCSB/GDC bilayer electrolyte SOFC showing the effect of bilayer electrolyte in reducing the average $\boldsymbol{\mu_{O2}}$ inside GDC electrolyte

6.2.1 Effect of the YCSB/GDC thickness ratio and GDC thickness on power output

Maximum power density (MPD) of 10 μm GDC cells with different thickness ratios of YCSB/GDC across the temperature range of 650-500 ℃ are shown in **Figure 6-3** (a). All bilayer electrolyte cells showed higher MPD comparing to the single electrolyte cell (thickness ratio zero) across the temperature range of 650-500 ℃. At 650, and 600 ℃ increasing the thickness ratio from 0 to ~ 1.1 increased the MPD of the cell. However, at 550 and 500 ℃, increasing the thickness ratio from 0 to 1 increased the MPD of the cell and then increasing the thickness ratio beyond 1 decreased the MPD of the cell. Noticeably, the effect of implementing a YCSB/GDC bilayer electrolyte on enhancement of the power density at higher temperatures i.e. 650 and 600 ℃ is more pronounced compared to 550 and 500 ℃. This is largely due to the fact that GDC reduction under low pO_2 condition is more severe at higher temperatures and OCV of the cell deviates farther from theoretical values. Hence, effect of using a secondary electrolyte to block the internal leakage current is more noticeable at higher temperatures. I-V and I-P curves of three different 10 μm GDC cells with three different YCSB/GDC thickness ratios at 650 ℃ are shown in **Figure 6-3** (b). As can be seen, compared to the single GDC electrolyte cell, MPD of the SOFC with thickness ratios of 1.1 increased by 46% from 0.547, to 0.801 W/cm^2 at 650 ℃. At 500 ℃, MPD of the cell increased by 32% from 0.147 to 0.195 W/cm^2. As shown in **Figure 6-3** (b), increase of power density can be partially ascribed to the OCV enhancement of bilayer electrolyte cells (0.642V for single GDC cell and 0.825V for bilayer cell with thickness ratio of ~ 1.1). A more detailed analysis of the OCV of tested cells will be provided in the later sections. **Figure 6-3** (c)-(e) show representative SEM micrographs of the 10

μm GDC cells with three different thickness ratios (0, 0.33, and 1.1). All three cells had identical anode layer thickness and a 10 μm GDC electrolyte layer. The GDC electrolyte layer is very dense, pin-hole free and adhered well to the adjacent layers. The bilayer cells with thickness ratio of 0.33 and 1.1 had 4 and 13 μm YCSB layers, respectively. The YCSB layer sintered at 775 ℃ for 2 hours appeared to be reasonably dense with minor closed pores, but not as dense as GDC layer.

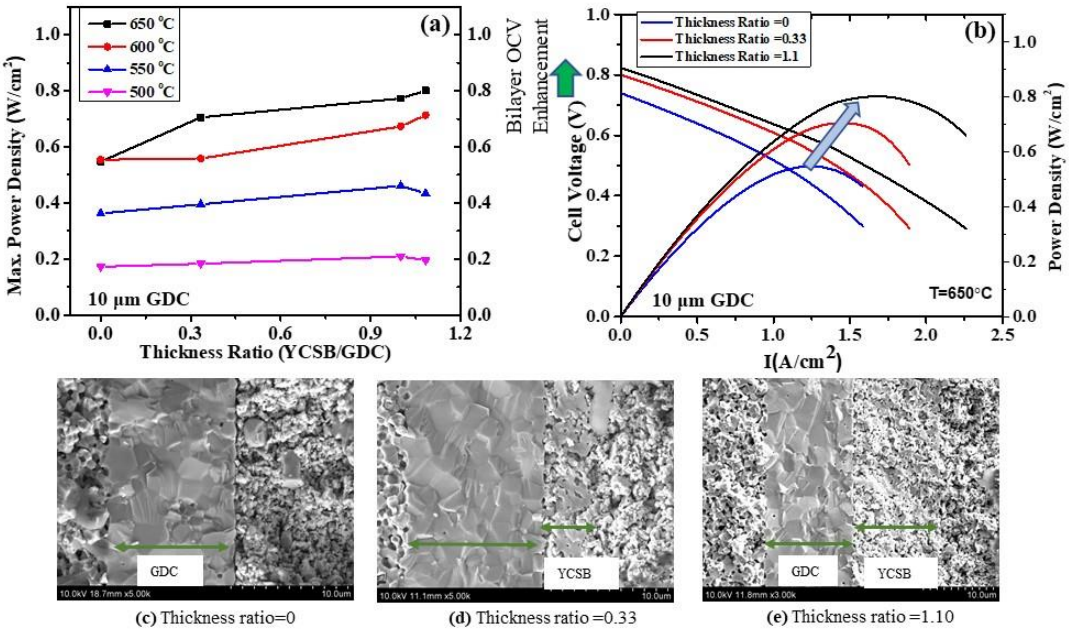
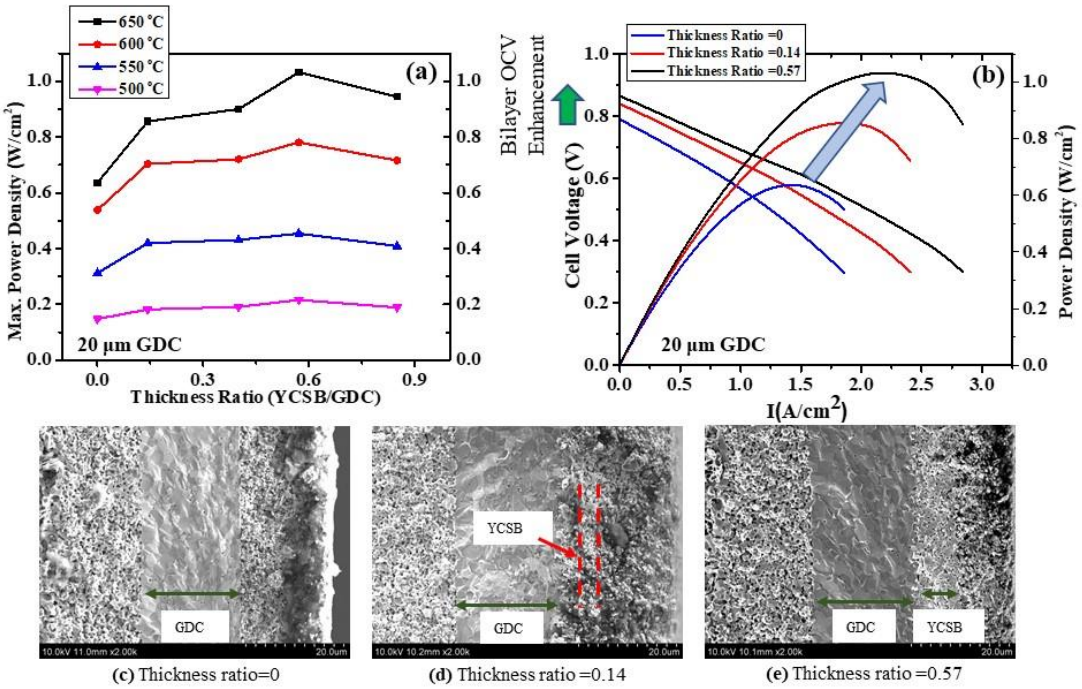


Figure 6-3 (a) MPD (W/cm^2) of 10 μm single electrolyte GDC (thickness ratio 0) and YCSB/GDC bilayer electrolyte SOFCs as a function of thickness ratio across the temperature range of 650-50 ℃, (b) Voltage-current curves (left axis) and power-current curves (right axis) for 10 μm GDC electrolytes with three different YCSB/GDC thickness ratios (0, 0.33 , and 1.1) at 650 ℃, and SEM micrographs of 10 μm GDC cells with YCSB/GDC thickness ratios of (c) 0, (d) 0.33, and (e) 1.1

MPD of the 20 μm GDC cells with different thickness ratios across the temperature range of 650-500℃ are shown in **Figure 6-4** (a).



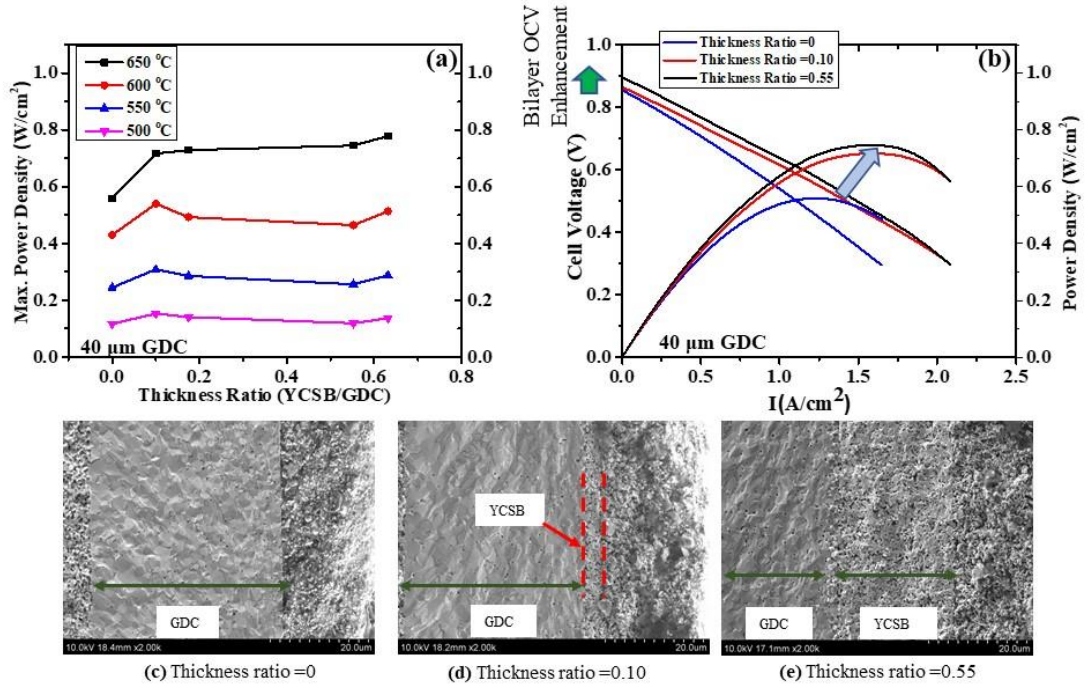
(c) Thickness ratio=0 (d) Thickness ratio =0.14 (e) Thickness ratio =0.57

Figure 6-4 (a) MPD (W/cm^2) of 20 µm single electrolyte GDC (thickness ratio 0) and YCSB/GDC bilayer electrolyte SOFCs as a function of thickness ratio across the temperature range of 650-50 °C, (b) Voltage-current curves (left axis) and power-current curves (right axis) for 20 µm GDC electrolytes with three different YCSB/GDC thickness ratios (0, 0.14 , and 0.57) at 650 °C, and SEM micrographs of 20 µm GDC cells with YCSB/GDC thickness ratios of (c) 0, (d) 0.14, and (e) 0.57

Similar to the 10 µm GDC based SOFCs discussed above, all bilayer samples showed higher power density compared to the 20 µm single electrolyte GDC cell. Between 650 and 500 °C, the bilayer cell with the thickness ratio of 0.57 showed the highest MPD and further increasing the thickness ratio to ~ 0.85 decreased the MPD of the cell. As observed for the 10 µm GDC cells, effect of using a bilayer electrolyte was less pronounced at lower temperatures. At 650 °C, as shown by the I-V and I-P curves in **Figure 6-4** (b), MPD of the SOFCs with thickness ratios of 0, 0.14, and 0.57 reached 0.636, 0.856, and 1.032 W/cm^2, respectively (62% increase for thickness ratio of 0.57 compared to the single GDC cell). Increase of MPD can be partially attributed to the enhancement of the OCV as illustrated by the I-V curves in **Figure 6-4** (b) (0.791V for

single GDC cell and 0.865 for bilayer cell with thickness ratio of ~ 0.57). **Figure 6-4** (c)-(e) show the representative SEM micrographs of 20 μm GDC cells with thickness ratios of 0, 0.14, and 0.57. The finer microstructure of the AFL can be distinguished from the coarser microstructure of the ASL layer. All cells had a dense 20 μm GDC electrolyte layer and thickness of the YCSB layer was varied from 0 (single electrolyte cell) to 12 μm (thickness ratio of 0.57).

MPD of the 40 μm GDC cells with different thickness ratios across the temperature range of 650-500 ℃ are shown in **Figure 6-5** (a). Unlike 10 and 20 μm GDC cells, increasing the thickness of the YCSB layer beyond 4 μm did not show dramatic improvement in MPD of the cell. This is mainly due to the fact that a thicker GDC electrolyte is less susceptible to reduction and hence a less sensitive thickness-ratio dependence behavior was observed. The I-V and I-P curves at 650 ℃ for three 40μm GDC cells with thickness ratios of 0, 0.1, and 0.55 are shown in **Figure 6-5** (b). MPD of the cells with thickness ratios of 0, 0.1, and 0.55 reached 0.559, 0.717, and 0.745 W/cm^2 respectively (~ 33% increase). Representative SEM micrographs of the 40 μm GDC cells with thickness ratios of 0, 0.1, and 0.55 are shown in **Figure 6-5** (c)-(e). All cells had a dense 40 μm GDC electrolyte layer and thickness of the YCSB layer was varied from 0 (single electrolyte cell) to 21 μm (thickness ratio of 0.55).



(c) Thickness ratio =0 (d) Thickness ratio =0.10 (e) Thickness ratio =0.55

Figure 6-5 (a) MPD (W/cm^2) of 40 μm single electrolyte GDC (thickness ratio 0) and YCSB/GDC bilayer electrolyte SOFCs as a function of thickness ratio across the temperature range of 650-50 ℃, (b) Voltage-current curves (left axis) and power-current curves (right axis) for 40 μm GDC electrolytes with three different YCSB/GDC thickness ratios (0, 0.10 , and 0.55) at 650 ℃, and SEM micrographs of 40 μm GDC cells with YCSB/GDC thickness ratios of (c) 0, (d) 0.10, and (e) 0.55

6.2.2 Effect of YCSB/GDC thickness ratio and GDC thickness on OCV

As shown previously in I-V curves, bilayer electrolyte cells had higher OCV than single electrolyte cells. Figure **6-6** compares the OCV of 10, 20, and 40 μm GDC cells as a function of YCSB/GDC thickness ratio across the temperature range of 650-500 ℃. For the single GDC electrolyte cells (i.e., thickness ratio of 0.0) increasing the thickness of the GDC layer increased the OCV of the cell. At 650 ℃ OCV of 10, 20, and 40 μm single GDC electrolyte cells were 0.740, 0791, and 0.856 V, respectively.

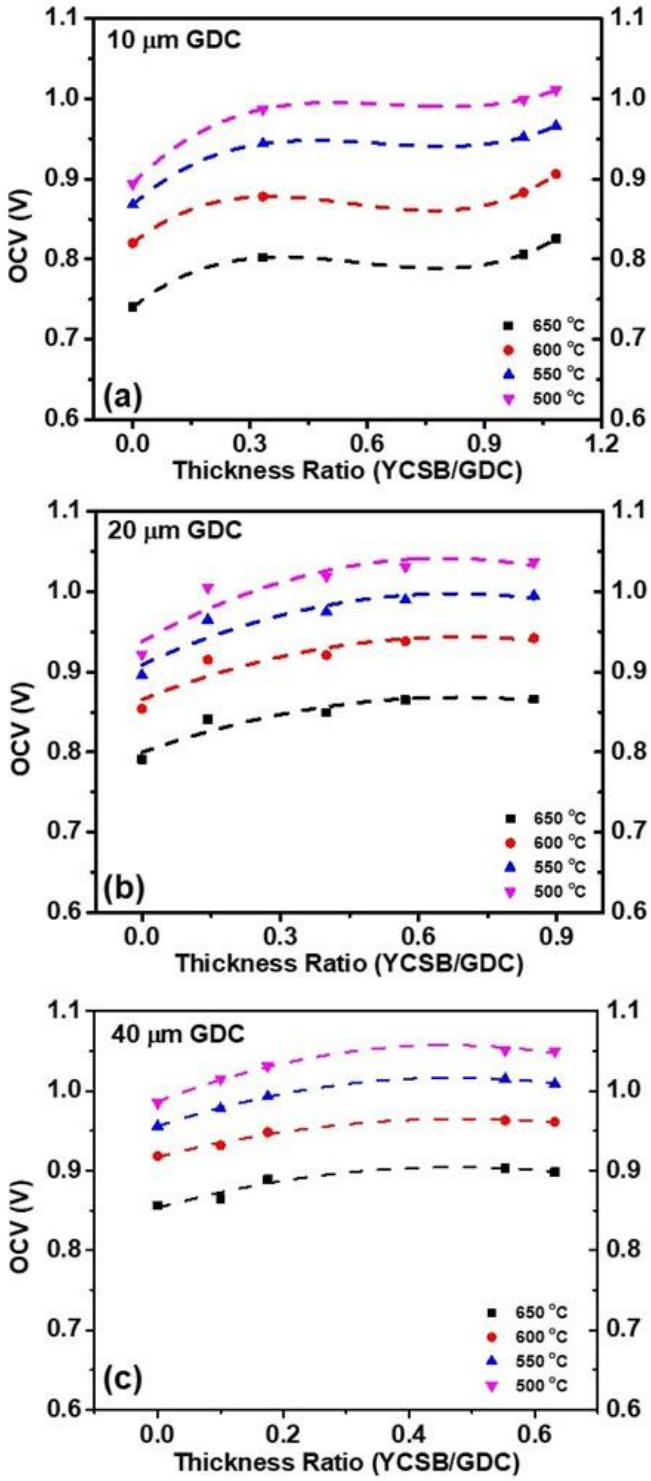


Figure 6-6 Effect of YCSB/GDC thickness ratio on the OCV of (a) 10 μm GDC cells, (b) 20 μm GDC cells, and (c) 40 μm GDC cells across the temperature range of 650-500 °C. Thickness ratio zero refers to single electrolyte GDC cell with no YCSB layer.

For 10 μm GDC cells (Figure **6-6** (a)), increasing the thickness of the YCSB layer from zero (thickness ratio 0) to 13 μm (thickness ratio 1.1) increased the OCV of the cell between 650 and 500 ℃. At 650 ℃, OCV of 10 μm GDC cells with thickness ratios of 0.0, 0.33, 1.0, 1.1 were 0.74, 0.802, 0.806,0.825 V respectively. Increasing the thickness ratio to 2.3 does not yield a stable OCV, and hence not reported here.

For 20 μm GDC cells (Figure **6-6** (b)), increasing the thickness ratio from 0 to 0.57 increased the OCV of the cell and further increasing the thickness of the YCSB layer had negligible influence on OCV. At 650 ℃, OCV of the 20 μm GDC cells with thickness ratios of 0, 0.14, 0.4, 0.57, and 0.85 were 0.791, 0.841, 0.849, 0.865, 0.866 V, respectively. Same trend was observed for the 40 μm GDC cells (Figure **6-6** (c)) and a less sensitive thickness ratio-dependent behavior (plateaued at the lower thickness ratio of 0.17) was observed. At 650 ℃, OCV of 40 μm GDC cells with thickness ratios of 0, 0.1, 0.17, 0.55, 0.63 were 0.856, 0.865, 0.889, 0.903, 0.898 V, respectively. This clearly indicates that as the thickness of the GDC layer increases, the effect of having an electron blocking layer becomes less significant, and essentially for a very large electrolyte thickness (e.g. ≥40 μm) no blocking layer is required. However, a very thick GDC electrolyte layer imposes a large ohmic loss across the electrolyte layer and thus fails to deliver a reasonable power output. As shown in Figure **6-6**, OCV enhancement as a result of depositing a ~ 3-4 μm YCSB layer was less significant for thicker GDC electrolytes. For 10, 20, 40 μm GDC electrolytes, OCV of the cell at 650 ℃ was increased by 62, 50, and 9 mV respectively. As mentioned earlier, this is due to the fact that thicker GDC electrolytes are less prone to reduction and hence deviates from theoretical OCV values to a lesser extent. It is also worth mentioning that similar

thickness ratios yielded different OCV values for different GDC electrolyte thicknesses. For instance, at 650 ℃, YCSB/GDC bilayer electrolyte cells with thickness ratio of ~ 0.56 and GDC thicknesses of 20 and 40 μm yielded OCV of 0.865 and 0.903 V, respectively. The above results suggest that OCV of bismuth oxide/ceria bilayer electrolyte SOFCs is a function of both GDC thickness and total thickness of the electrolytes. Additionally, variation of OCV with temperature is more discernible for a thinner GDC electrolyte cell. For instance, while the OCV of the 10 μm GDC single electrolyte cell increased from 0.740 V to 0.894 V (154 mV) as temperature was decreased from 650 ℃ to 500 ℃, OCV of the 40 μm GDC single electrolyte cell increased from 0.856 V to 0.985 V (129 mV) over the same range of temperature decrease. Table **6-1** compares the OCV values of representative cells from this work with values reported in literature for bismuth oxide/ceria bilayer electrolyte SOFCs. YCSB/GDC bilayer electrolyte SOFCs shown in this work yielded higher OCV values compared to the values reported in literature with similar GDC electrolyte thickness and bismuth oxide/ceria thickness ratio. Higher OCV values obtained in this work using YCSB as the blocking layer (2^{nd} electrolyte) illustrates that YCSB/GDC is a promising bilayer electrolyte for advanced high performing LT-SOFCs and showed significant advantage over previous composition of bismuth oxide, i.e., ESB.

At higher temperatures (650 and 600 ℃), MPD of 10 μm GDC cells (Figure **6-3** (a)) and OCV (Figure **6-6** (a)) showed similar trends as a function of thickness ratio. However, at lower temperatures, for all GDC thicknesses, MPD and OCV of the tested cells did not peak at the same thickness ratio. This can be attributed to the effect

of bilayer electrolyte configuration on altering the ohmic losses of the cells as discussed in the next section.

Table 6-1 OCV of ceria/bismuth oxide bilayer electrolyte SOFCs as a function of Ceria thickness and bismuth oxide/ceria thickness ratio across the temperature range of 650-500 ℃

Ceria Thickness (μm)	Bismuth oxide Thickness (μm)	Thickness Ratio	OCV (V) 650℃	600℃	550℃	500℃	Reference
10[1]	0	0.00	0.68	--	--	--	[47]
10[1]	***0***	***0.00***	***0.740***	***0.820***	***0.868***	***0.894***	***This work***
10[1]	4[4]	0.40	0.77	--	--	--	[47]
10[1]	5[4]	0.50	0.778	0.815	0.840	0.852	[48]
12[1]	***4[5]***	***0.33***	***0.802***	***0.878***	***0.944***	***0.987***	***This work***
12[1]	***13[5]***	***1.08***	***0.825***	***0.906***	***0.966***	***1.011***	***This work***
16[1]	6[4]	0.38	0.835	0.849	0.866	0.874	[48]
20[1]	2[4]	0.10	0.74	0.78	0.82	0.84	[81]
20[1]	***3[5]***	***0.14***	***0.841***	***0.915***	***0.965***	***1.005***	***This work***
20[1]	***8[5]***	***0.40***	***0.849***	***0.921***	***0.975***	***1.019***	***This work***
20[1]	***17[5]***	***0.85***	***0.866***	***0.942***	***0.995***	***1.037***	***This work***
20[2]	20[4]	1.00	0.800	0.855	0.902	0.943	[50]
22[2]	20[4]	0.91	0.801	0.853	0.911	0.945	[83]
26[3]	6[6]	0.23	0.852	0.897	0.929		[46]
38[1]	***21[5]***	***0.55***	***0.903***	***0.963***	***1.015***	***1.051***	***This work***
48[1]	4[4]	0.08	0.876	0.913	0.937	0.946	[48]
50[1]	20[4]	0.40	0.87	--	--	--	[47]
84[1]	16[6]	0.19	0.855	0.885	0.91	0.94	[110]

[1]GDC, [2]SDC, [3] SNDC,[4] ESB, [5] YSB, [6] YCSB

6.2.3 Effect of YCSB/GDC thickness ratio and GDC thickness on ohmic and non-ohmic losses

Representative Nyquist plots for 10 μm, 20 μm, and 40 μm GDC with different YCSB/GDC thickness ratios at 650 ℃ are shown in Figure **6-7**. As illustrated in Figure **6-7**, intercept of the impedance spectra at higher frequencies with the real axis shifts towards higher ASR values as the thickness of the GDC electrolyte was increased from 10 μm (Figure **6-7** (a)) to 40 μm (Figure **6-7** (c)). Intuitively, it is anticipated that adding a 2nd electrolyte layer would increase the ohmic losses across the electrolyte. However, as shown by the impedance spectra in Figure **6-7**, all bilayer electrolyte cells had lower ohmic ASR compared to the single GDC electrolyte with identical GDC thickness. Impedance spectra were modeled using the equivalent circuit shown as inset of Figure **6-7**(a).

Ohmic ASR of each cell was normalized to that of single GDC electrolyte cell with the same GDC thickness across the temperature range of 650-500 ℃ and are shown in Figure **6-8**. The lines are for eye-guidance. At 650 and 600 ℃, regardless of the GDC electrolyte thickness, all bilayer cells show lower ohmic ASR compared to the single GDC electrolyte cell with identical GDC thickness. At 550 ℃, 10 and 20 μm GDC cells showed lower ohmic ASR for all thickness ratios and 40 μm GDC cells showed slightly higher (10%) ASR only at thickness ratio of 0.55. As temperature decreased to 500℃, ohmic ASR of bilayer electrolyte cells showed an increasing trend with thickness ratio as the thickness of the YCSB layer was increased. Ohmic ASR of the bilayer electrolyte cells compared to the same thickness single GDC electrolyte cell was lower, particularly at higher temperatures.

We believe that this behavior is attributed to the change of average PO_2 in the GDC layer as schematically shown in Figure **6-2**.

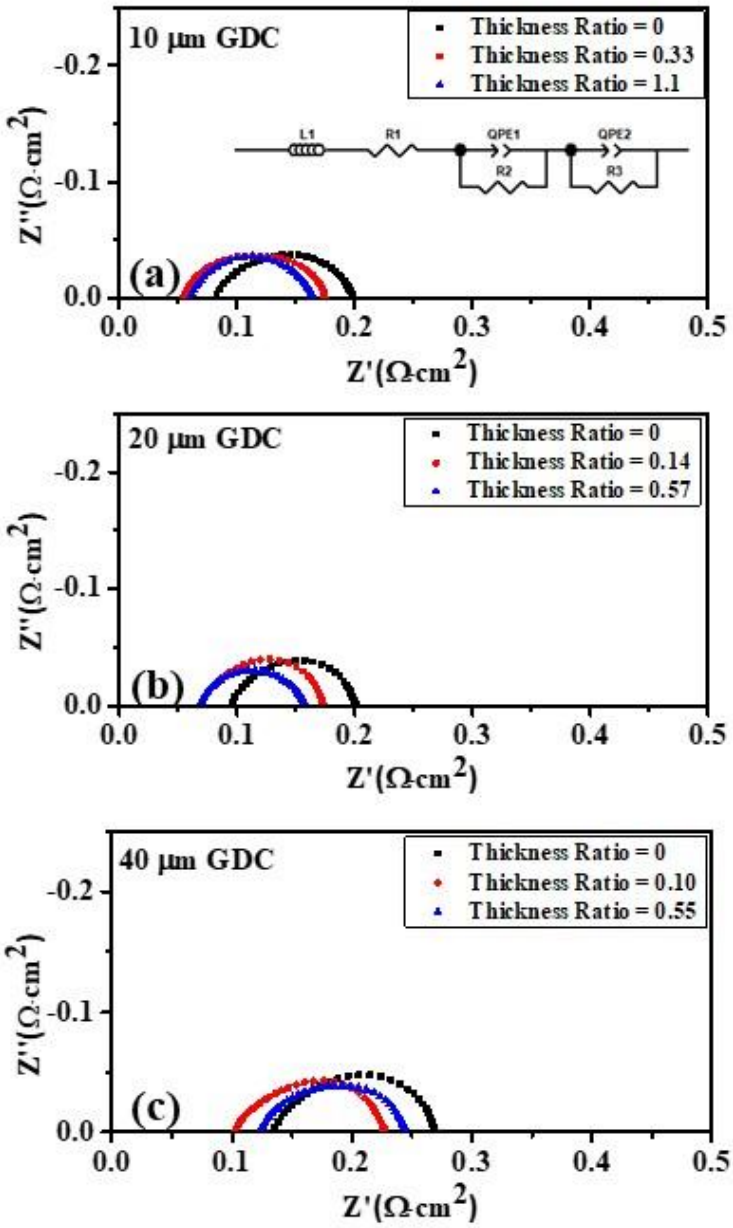


Figure 6-7 Representative Nyquist plots for (a)10 μm GDC- inset: equivalent circuit to model the impedance spectra, (b)20 μm GDC, and (c) 40 μm GDC bilayer cells with different YCSB/GDC thickness ratios at 650 °C

Assuming constant pO_2 values at cathode and anode sides of the cell, inserting the YCSB layer decreases the average pO_2 in the GDC electrolyte and hence electronic conductivity of GDC increases (Figure **6-9**) [136].

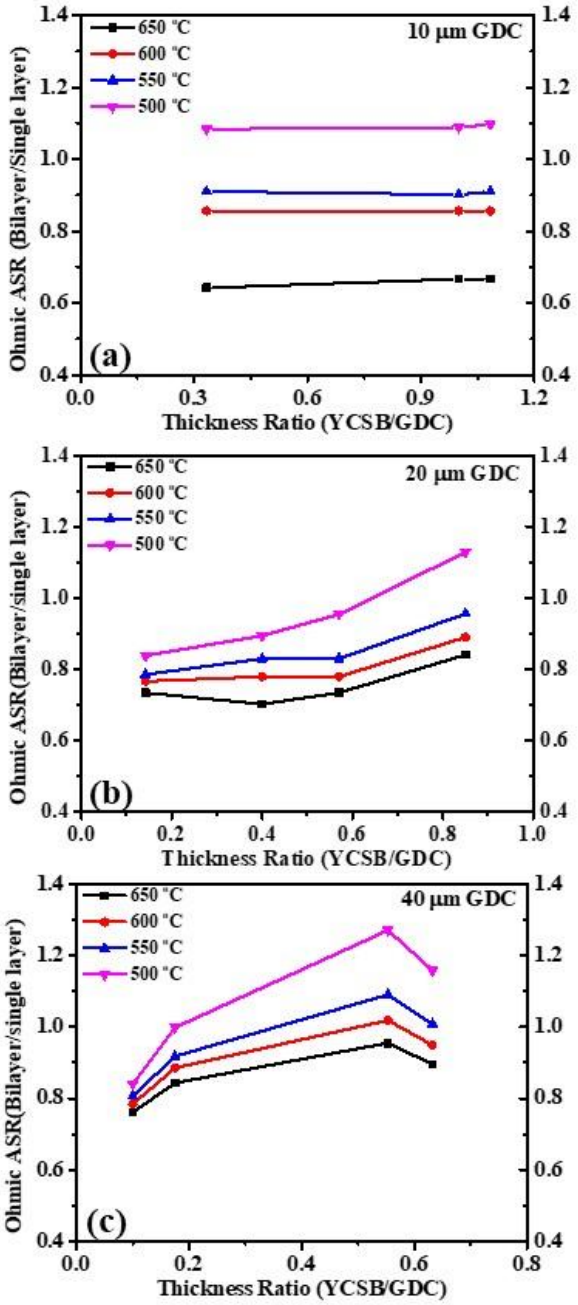


Figure 6-8 Ohmic ASR of the YCSB/GDC bilayer SOFCs normalized to the single GDC electrolyte cell for (a)10 μm, (b)20 μm, and (c) 40 μm GDC cells across the temperature range of 650-500 °C

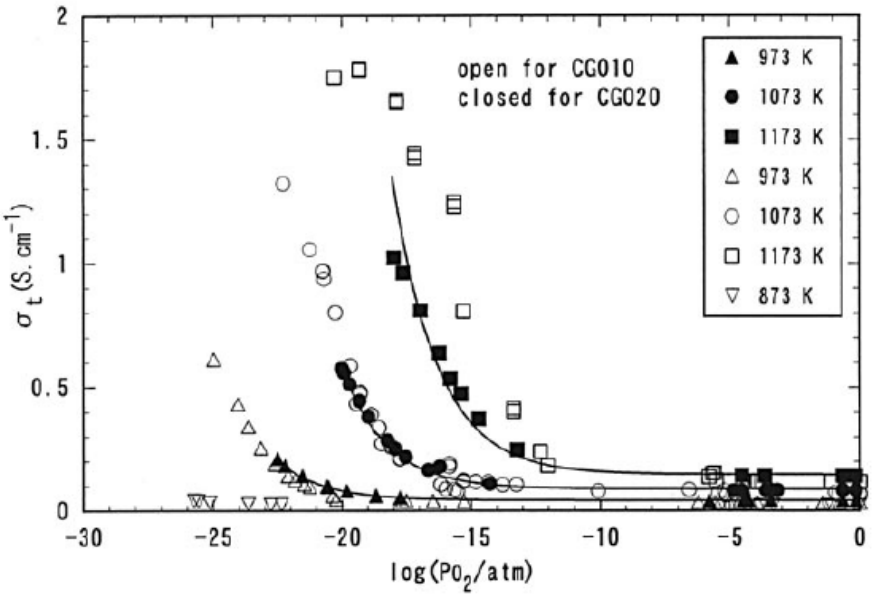


Figure 6-9 Effect of pO2 on the electrical conductivity of 10GDC and 20GDC [136]

As shown in **Figure 6-8**, at 650 ℃ where GDC reduction is more severe, decrease of ohmic ASR for the bilayer cell from the respective single GDC electrolyte cell intensifies as the thickness of the GDC electrolyte decreases. For example, at an arbitrary thickness ratio of 0.6, normalized ohmic ASR of 10, 20, and 40 μm GDC cells were, 0.64, 0.73, and 0.89, respectively. This behavior is likely due to the fact that a thinner GDC is more prone to reduction [134], resulting in lower average pO_2 and increased leakage current associated with MIEC type GDC electrolyte. This is in agreement with measured OCV values shown in **Figure 6-6**, where thinner GDC cells deviates more from theoretical OCV values. At 500 ℃, where GDC reduction is relatively small and electronic leakage of GDC is less, normalized ASR of the bilayer electrolyte cells were more thickness ratio sensitive with increasing GDC thicknesses due to addition of YCSB layer resistance (**Figure 6-8** (b) and (c)). Consequently, under the conditions where GDC reduction is more severe, i.e., at higher temperatures ($T \geq$ 600 ℃) or thinner GDC electrolyte thickness (~ 10 μm), ohmic ASR reduction is

significant. However, when GDC reduction is less predominant, i.e., at lower temperatures (500 ℃ ≤T≤ 550 ℃) or thicker GDC electrolyte (~ 40 μm), increasing the YCSB thickness can impose additional ohmic ASR across the bilayer electrolyte, which will further reduce the power output of the cell. Therefore, a thickness ratio that increases the OCV of the cell without significant increase of ohmic ASR should be considered for the SOFC design. Absolute ohmic ASR values of the 20 μm GDC cells with different YCSB/GDC thickness ratios are shown in **Figure 6-10**. Dotted lines in **Figure 6-10** represent the theoretical ohmic ASR of the electrolyte(s) calculated using the conductivity of GDC and YCSB in air. As can be seen, between 650 ℃ and 550 ℃, all bilayer samples showed lower ohmic ASR compared to the single electrolyte cell. At 500 ℃, only the bilayer sample with the thickness ratio of 0.85 showed a slightly higher ohmic ASR value compared to the single electrolyte cell. Ohmic ASR of the bilayer electrolyte cells increased as the thickness of the YCSB layer was increased. It is worth mentioning that at lower temperatures i.e. 500 ℃, effect of thickness ratio was more significant and a steeper increase of ohmic ASR as a function of thickness ratio was observed. This is due to the fact that conductivity of YCSB decreases at 500 ℃ and effect of a thicker YCSB layer becomes more discernible. All bilayer electrolyte cells showed lower ohmic ASR values comparing to the theoretical values (dot lines). As discussed previously, disruption of P_{O_2} profile across the GDC layer, as a result of the bilayer electrolyte configuration, lowers the average P_{O_2} in the ceria layer and increases the electrical conductivity of ceria. Hence, measured ohmic ASR values were lower than theoretical values calculated using conductivity of GDC in air (P_{O_2} ~ 0.21).

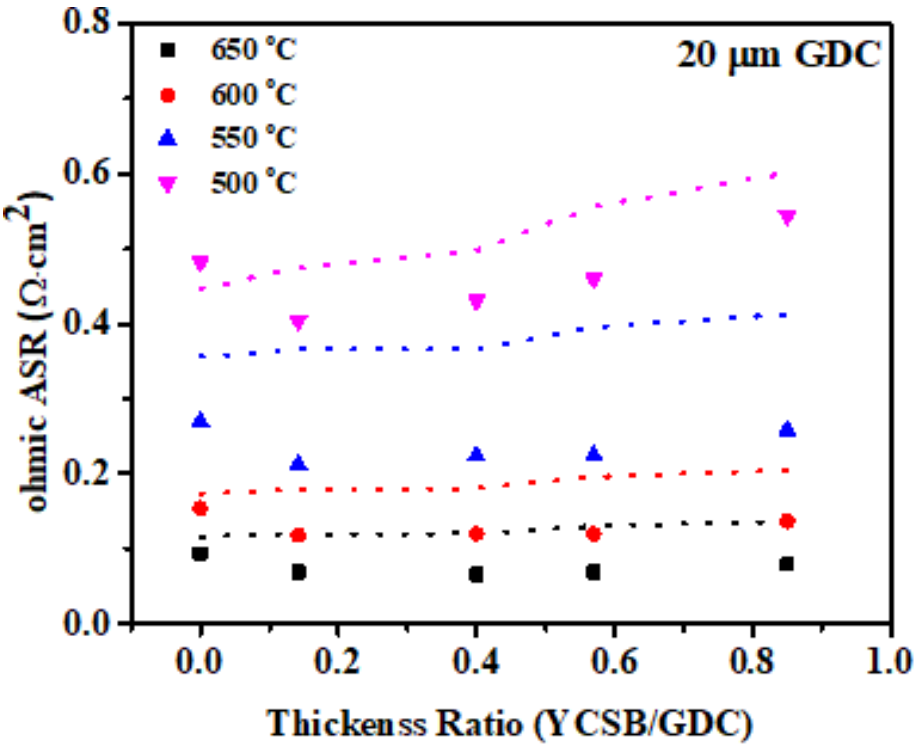


Figure 6-10 Ohmic ASR (Ω.cm2) of 20 µm GDC cells as a function on YCSB/GDC thickness ratio across the temperature range of 650-500 ℃. Dot lines represent theoretical ohmic ASR of the electrolyte(s) using their conductivity in air

The main focus of this study was investigating the effect of GDC thickness and YCSB/GDC thickness ratio on the OCV and ohmic ASR of the bilayer electrolyte SOFCs between 650 and 500 ℃ and hence non-ohmic ASR contributions were of less significant. However, to avoid complexities same standard electrodes, NiO-GDC (60:40) as anode and LSM-YCSB (40:60) as cathode, were used for all the cells that have been investigated in this study. Non-ohmic ASR of the 10,20, and 40µm cells at 650℃ normalized to the respective single electrolyte cell values are shown in Figure **6-11**. No relationship between thickness ratio and the normalized non-ohmic ASR of the bilayer electrolyte cells was observed. The variation of the non-ohmic ASR with thickness ratio can be attributed to the batch-to-batch variability of the NiO-GDC anode support tapes.

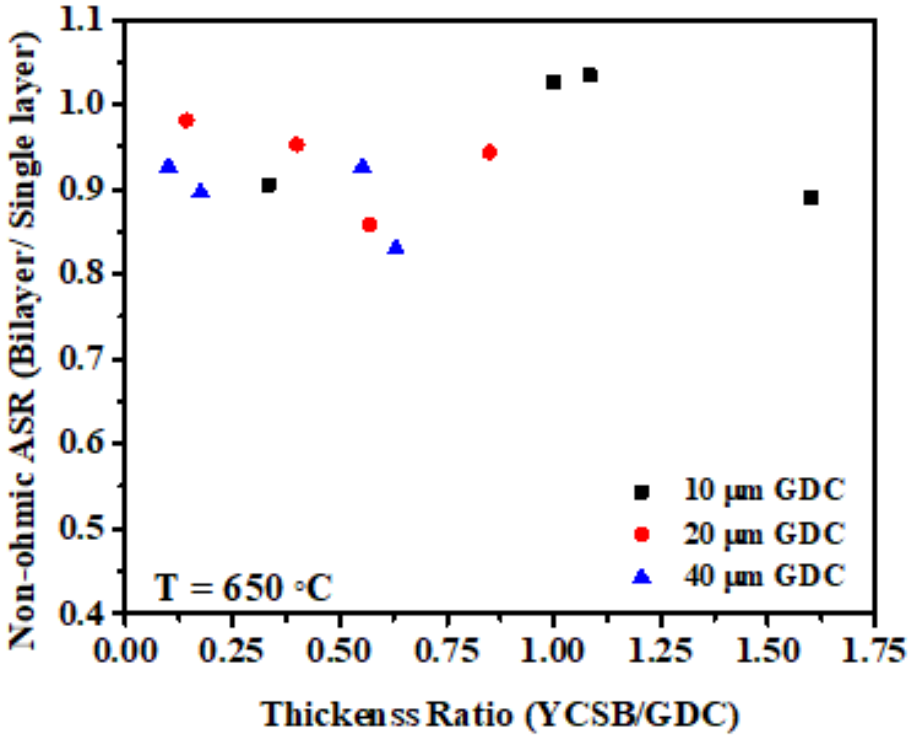


Figure 6-11 Normalized non-ohmic ASR of 10, 20, and 40 µm GDC cells with different YCSB/GDC thickness ratio at 650 ℃

As discussed above, at lower temperatures, i.e., 500-550 ℃, using a thin GDC electrolyte ~ 10 µm with an intermediate ceria/bismuth oxide thickness ratio can maximize the power density of the cell. Following this logic, high-performance low-temperature (LT)-SOFCs will be developed. In addition to the bilayer electrolyte configuration to enhance the OCV of the cell, non-ohmic ASR of the cell was reduced by means of anode and cathode infiltration. More details regarding this approach will be discussed in next chapter.

7 High-Performance Low-Temperature Solid Oxide Fuel Cell Using Bilayer Electrolyte and Nanostructured Electrodes

As temperature decreases below 600 ℃, electrode polarization resistance increases rapidly, playing a major role in determining the performance of SOFCs. With respect to SOFC anode, pure LSM has negligible oxygen ion conductivity and low oxygen surface exchange coefficient [137-139] and hence its catalytic activity is limited to the electrode/electrolyte interface. However, composite cathodes consisting of an electronically conductive phase mixed with an oxygen ion conducting phase such as YSZ, GDC or ESB have the advantage of extending the triple phase boundary (TPB) length into the bulk of electrolyte and decreasing the polarization resistance significantly. An extensively pursued approach to further enhance the TPB length of the electrode entails using nanoscale electrode microstructure using facile infiltration approach [139-147]. Infiltration facilitates enhanced electrocatalytic activity on cathode surfaces by incorporating various nanoparticles such as doped ceria [144, 148-151], LSM [152-156], LSC[157-161], LSF [162-164], SSC [165, 166], and Pd [167]. Similarly, anode infiltration helps enhance the catalytic activity (thereby improving the cell performance), improve anode material compatibility with hydrocarbon-based fuels and create tolerance to fuel impurities, e.g., sulfur. Anode side of SOFCs is typically infiltrated with various electrocatalysts such as doped ceria and zirconia [147, 149, 168-173], copper [174-176], iron[177], nickel[178-181], precious metals (such as Ru and Pd) [105, 182-185], LSCM [186, 187], and LST[188].

The primary focus of this chapter is to develop a high-performance anode-supported SOFC at temperatures ≤ 600 ℃. Towards this goal, ohmic loss of the cell was

minimized by using a thin bismuth oxide/ceria bilayer electrolyte. Since the traditional stabilized bismuth oxide composition, i.e. $(Bi_{0.8}Er_{0.2})_2O_{3\pm\delta}$ (ESB) suffers from conductivity decay due to ordering phenomena at temperatures ≤ 600 ℃, a stable bismuth-based electrolyte was needed. A heavily doped bismuth oxide composition (Y and Ce co-dopants) with stable ionic conductivity $(Bi_{0.75}Y_{0.25})_{1.86}Ce_{0.14}O_{3\pm\delta}$ (YCSB) [56] was used in this study. Additionally, to enhance the catalytic activity of electrodes, both anode and cathode sides of the cell were infiltrated with nanostructured LSM and Ni-GDC particles, respectively.

7.1 Experimental

7.1.1 Symmetrical Cell fabrication

To study the effect of infiltration on the polarization resistance of LSM-YCSB cathode, two identical symmetrical cells i.e. LSM-YCSB/YCSB/LSM-YCSB, with and without infiltration were fabricated and tested across the temperature range of 650-500 ℃ and different partial pressure of oxygen (p_{O2}). Cathode paste was made following the procedure outlined in **section 3.3.2**. 1.5/12µm (1:1) PMMA (soken) mixed pore formers were added (23 wt.% to that of paste) to introduce porosity in the cathode. One of the symmetrical cells was infiltrated with LSM ($La_{0.8}Sr_{0.2}MnO_{3-\delta}$) precursor solution. Following the procedure outlined elsewhere [189], 1 M LSM solution was prepared by dissolving stoichiometric nitrates of lanthanum, strontium, and manganese in water. A few drops of the precursor solution were then placed on top of the LSM-YCSB cathode (both sides of the symmetrical cell) and the cells were kept under vacuum for 10 minutes. The infiltrated cells were then heat-treated at 400 ℃ (1 hour)

to form the LSM nanoparticles. Infiltration process was repeated three times to obtain a final loading of 0.8%.

7.1.2 Anode-supported button Cell fabrication

Anode-supported half-cells consisted of ~600 μm NiO-GDC (60:40) anode support layer (ASL) (with 3 wt.% 10 μm PMMA pore former), ~20 μm NiO-GDC (50:50) anode functional layer (AFL) and a 5-10 μm GDC electrolyte layer were fabricated by tape casting as outlined in **section 3.4.1**. To form bilayer electrolyte, GDC electrolyte layer was fabricated by tape-casting and the dense thin YCSB layer was deposited using pulsed laser deposition (PLD). YCSB target for PLD was fabricated by pressing 8 grams of YCSB powder in a 28.6 mm cylindrical die and sintering at 1100 ℃ for 5 hours. YCSB film deposited by PLD was fabricated under an oxygen environment with a pressure of 30 mTorr. During the deposition process, the spot size of the laser beam on the target was about 0.06 cm^2, the ablation energy was 20 mJ, and the pulse frequency was 20 Hz. Under such deposition conditions, a deposition rate of 0.5 Å/sec was achieved.

For deposition of bismuth oxide materials using PLD the substrate temperature was kept at 600 ℃. After deposition, one sample was further annealed at 775 ℃ for 2 hours and the quality of the resultant bismuth oxide thin film was examined.

After depositing the YCSB electrolyte, LSM-YCSB (40:60) cathode paste was deposited as described in **section 3.4.3**. Following the completion of cell fabrication, the anode side of the cell was infiltrated with Ni and GDC ($Gd_{0.1}Ce_{0.9}O_{2-\delta}$) precursor solution. Stoichiometric amounts of cerium, gadolinium and nickel nitrates (Alfa Aesar) was dissolved in water. A few drops of the precursor solution were then placed

on top of the porous anode using a pipette and vell was then kept under vacuum for 10 minutes. The infiltrated cell was then heat-treated at 400 ℃/1hr [190]. The infiltration process was repeated three times. Infiltration loading was determined by monitoring the weight change before and after heat treatment. Final infiltration loading was ~ 2 wt. % of the total cell weight.

7.2 Results and Discussion

7.2.1 GDC/YCSB Bilayer fabrication using PLD

Cross-section and surface micrographs of both as-deposited and annealed bilayer samples are shown in Figure **7-1**. The as-deposited sample yielded a dense ~ 2 μm YCSB layer. The surface of the YCSB layer deposited at 600 ℃ without any additional annealing appeared to be dense without any surface cracks, pinholes or defects. However, as the bilayer sample was further annealed at 775 ℃ for 2 hours, cracks on the surface of the YCSB layer were observed. Although such cracks and defects appeared to be surface phenomenon generated during the annealing process, since the as-deposited sample resulted in a dense YCSB layer, no further post-deposition annealing was done during the button-cell fabrication process.

The interface of the GDC/NGSB bilayer sample annealed at 775 ℃ for 2 hours was also examined by EDX line-scan and elemental mapping and shown in Figure **7-2**. The signal from Bi Mα peak increased, while the signal from Ce Lα peak decreased sharply at the GDC/YCSB interface, suggesting that there is no significant inter-diffusion of elements between GDC and YCSB layers Figure **7-2** (a). EDX elemental mapping across the GDC/YCSB interface, Figure **7-2** (b) also confirmed the absence of inter-diffusion between PLD deposited YCSB and GDC substrate.

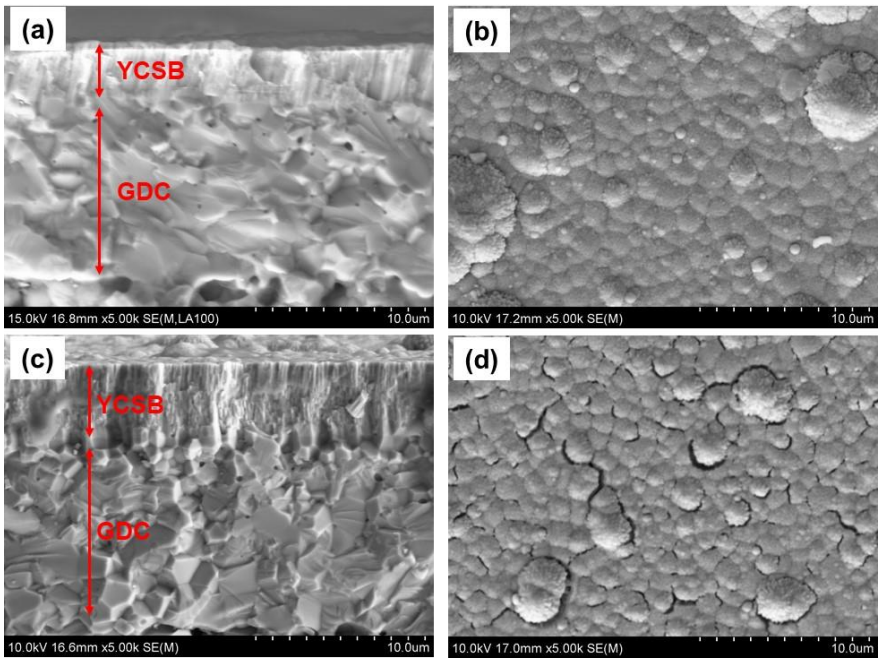


Figure 7-1 SEM micrographs of YCSB/GDC bilayer samples; YCSB was deposited by PLD at 600 °C. (a)the cross-section, and (b)surface of the as-deposited sample, (c) cross-section, and (d) surface of the sample annealed at 775 °C for 2 hours.

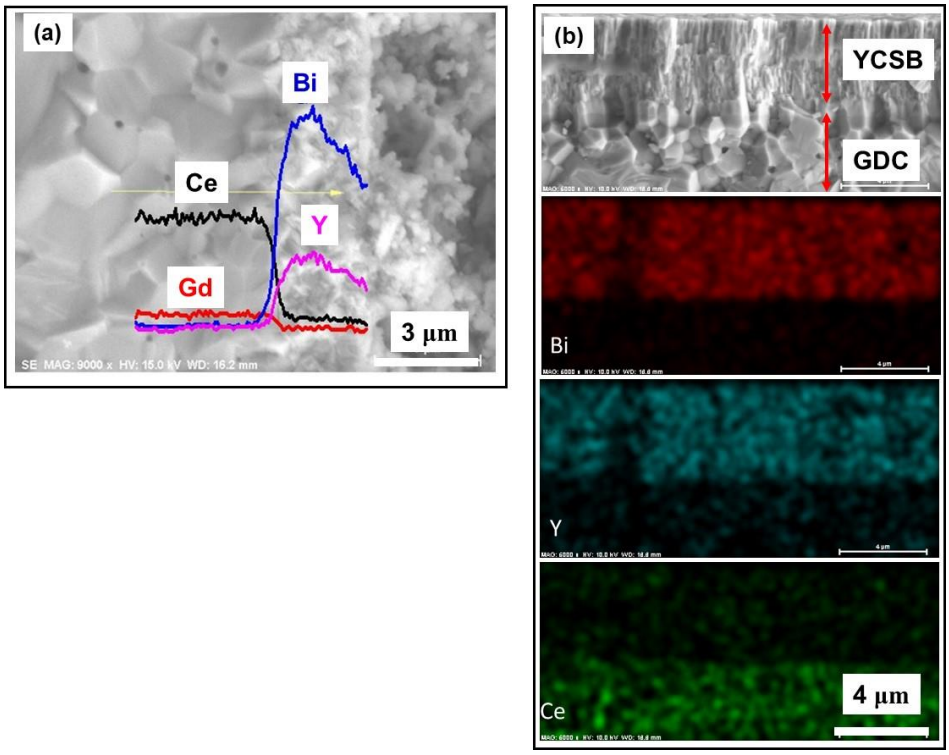


Figure 7-2 (a) EDX line scan for GDC/YCSB interface, and (b) EDX elemental mapping scan for GDC/YCSB interface; YCSB deposited by PLD at 600 °C and annealed at 775 °C for 2 hours

7.2.2 SOFC Testing and Analyses

Two anode-supported button cells: Cell (A) Ni-GDC(60:40)|GDC (20 μm)|LSM-YCSB(40:60), and Cell (B) Ni-GDC(60:40)|GDC(7-8 μm)|YCSB (2 μm)| LSM-YCSB (with infiltration) were fabricated and tested under identical testing conditions. Current-voltage-power (I-V-P) curves and Nyquist plots for both cells across the temperature range of 650-500 ℃ are shown in Figure **7-3**.

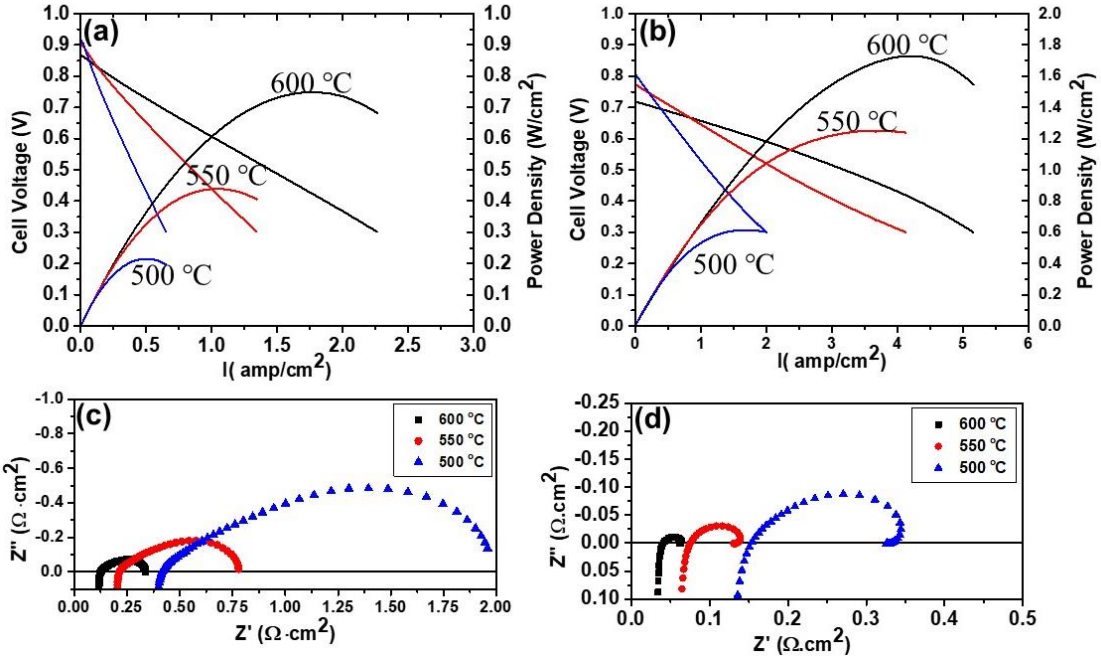


Figure 7-3 I-V and power density curves for (a) Cell (A), (b) Cell (B); Nyquist plot for (c) Cell (A), (d) Cell (B) at 500-600 °C

As shown in Figure **7-3** (a) and (b), Cell (A) with a 20 μm GDC electrolyte yielded higher OCV values compared to Cell (B) with GDC (7-8 μm)/YCSB (2 μm) bilayer electrolyte. This is mainly caused by the fact that a thin GDC layer (7-8 μm) is more prone to reduction, yielding a lower OCV value. At 600, 550, and 500 ℃, OCV of Cell (A) and (B) reached 0.866V, 0.901V, 0.914V and 0.721V, 0.776V, 0.810V, respectively. However, the infiltrated cell (Cell B) delivered significantly higher power

density values. At 600, 550, and 500 ℃, maximum power density (MPD) of Cell B reached 1.729, 1.250, and 0.614 W/cm^2, respectively, while MPD of Cell (A) was 0.748, 0.439, and 0.215 W/cm^2. The substantial improvement of the power density was attributed to the reduction of ohmic and non-ohmic ASR of Cell (B) compared to Cell (A). As indicated by the Nyquist plots in Figure **7-3** (c) and (d), both ohmic (intercept of the real axis at high frequencies) and non-ohmic (distance between the low and high-frequency intercepts) of Cell (B) decreased significantly compared to Cell (A). The ohmic ASR of Cell (B) with a GDC (7-8 μm)/YCSB (2 μm) bilayer electrolyte (total thickness of ~10 μm) was 0.041, 0.075, and 0.154 Ω.cm^2 at 600, 500, and 500 ℃, respectively. For Cell (A) ohmic ASR of the cell at 600, 550, and 500 ℃ was 0.126, 0.213, and 0.417 Ω.cm^2, respectively. Reduction of non-ohmic ASR was even more drastic. At 600, 550, and 500 ℃ non-ohmic ASR decreased from 0.214, 0.599, and 1.672 Ω.cm^2 for Cell (A) to 0.022, 0.058, 0.177 Ω.cm^2 for Cell (B), respectively. Considering the identical electrode materials for both cells, the one-order of magnitude reduction in non-ohmic ASR of the Cell (B) is ascribed to deposition of nano LSM and Ni particles at the cathode and anode, respectively. The infiltrated particles provide a higher TPB length and facilitate the ORR and hydrogen oxidation at cathode and anode, respectively.

Table **7-1** compares the MPD and cell structure of selected literature reported data and our results. A remarkably high MPD value obtained in this work suggests that a thin GDC/YCSB bilayer electrolyte along with nano-structured electrodes helps lower the operating temperature range of SOFCs down to 600-500℃. Although the MPD reported in this work is higher than all non-cobalt based cathodes, it should be noted

Table 7-1 Comparison of Cell structure, materials, and MPD in the temperature range of 500-600 ℃

Anode	EL1(μm)	EL2(μm)	Cathode	MPD (mW/cm^2)			Ref
				500℃	550℃	600℃	
Ni-GDC(60:40)	GDC(8)	YCSB(2)	LSM-YCSB	614	1250	1729	This work
Non-cobalt cathode							
Ni-GDC	GDC(25)	ESB(2)	LSM-ESB	184	350	675	[81]
Ni-SDC (60:40)	SDC(26)	YSB(6)	LSM-YSB (50:50)	-	153	266	[46]
Ni-GDC	GDC(20)	YSB(10)	LSM-YSB	136	288	440	[82]
Ni-BCZYYb(60:40)	BCZYYb(20)		BCZY63	455	500	650	[191]
Ni-SNDC	SNDC(20)	ESB(20)	$La_{0.74}Bi_{0.1}Sr_{0.16}MnO_{3-\delta}$	292	515	788	[50]
Ni-GDC	GDC(20)	ESB(20)	$La_{0.74}Bi_{0.1}Sr_{0.16}MnO_{3-\delta}$	197	390	653	[109]
Ni-SDC	SDC(26)	YSB(6)	Ag-YSB(60:40)	223	380	571	[49]
Ni-YSZ (65:35)	YSZ(7)	ESB(5)	LSM-ESB (50:50)	-	310	750	[106]
Ni-SNDC (60:40)	SNDC(22)	ESB(20)	Pr0.5Ba0.5MnO3d-ESB (50:50)	231	476	782	[83]
Cobalt-containing cathode							
Ni-GDC(65:35)	GDC (10)		$Ba_{0.5}Sr_{0.5}Co_{0.8}Fe_{0.2}O_{3-\delta}$(BSCF)	454	863	1329	[192]
Ni-GDC(65:35)	GDC(20)		SSC-GDC	145	270	400	[193]
NiO-Fe_3O_4/SDC	LSGM(5)	SDC(0.4)	$Sm_{0.6}Sr_{0.4}CoO_{3-\delta}$	610	-	908	[194]
Ni-GDC	LSGM(2)	GDC(0.25)	$La_{0.6}Sr_{0.4}CoO_{3-\delta}$	573	-	1100	[195]
Ni-GDC(60:40)	GDC(7.33)		$La_{0.6}Sr_{0.4}Co_{0.2}Fe_{0.8}O_3$-GDC (50:50)	589	836	987	[196]
NiO-YSZ	YSZ(1)	GDC(0.20)	$La_{0.6}Sr_{0.4}CoO_{3-\delta}$-GDC	529	1084	1480	[197]
Ni-SDC	SDC(20)		SSC-SDC(75:25)	253	457	750	[198]
Ni-GDC	GDC(20)		$NdBa_{0.5}Sr_{0.5}Co_2O_{5+\delta}$-GDC (60:40)	300	500	1086	[199]
Ni-SDC(60:40)	SDC(20)		$Ba_{0.5}Sr_{0.5}Co_{0.8}Fe_{0.2}O_{3-\delta}$(BSCF)	402	651	1010	[200]
Ni-SDC(50:50)	SDC(20)		$SrNb_{0.1}Co_{0.9}O_{3-\delta}$	561	838	1008	[201]
Ni-GDC	GDC(15)		$NdBa_{0.75}Ca_{0.25}Co_2O_{5+\delta}$-GDC	660	1250	2114	[202]
Ni-SzSZ	ScSZ(2)	SDC(4)	$Sm_{0.5}Sr_{0.5}CoO_3$ (SSC)	-	127	281	[65]
Ni-SDC(47:53)	ScSZ(1)	SDC(6)	SSC-SDC (75:25)	216	500	937	[66]
Ni-YSZ (60:40)	YSZ(2)	SDC(6)	SSC-SDC (70:30)	-	420	700	[69]

that comparatively high MPDS (e.g. of 2114 mW/cm^2 at 600 ℃ [202]) was reported using an advanced cobalt-containing cathode.

7.2.3 SOFC Electrochemical Stability

The stability of anode-supported ceria/bismuth oxide bilayer electrolyte SOFCs has not been thoroughly addressed in literature. Thus, stability of ceria/bismuth oxide bilayer electrolyte based SOFCs is critical for long-term operation of SOFCs. As presented in Figure **7-4** (a), cell voltage decreased at the rate of 0.37%/h over the first 30 hours of operation and then the rate of degradation decreased to an average of 0.03%/h, which is much lower than the initial degradation. To understand the underlying reason for voltage degradation, OCV, impedance, and I-V-P curve of the cell was measured periodically (every 5 hours). As demonstrated in Figure **7-4** (b), despite the thin GDC/YCSB bilayer electrolyte, OCV of the cell did not suffer from major degradation, suggesting that the thin electrolyte maintained its mechanical integrity and 2 μm PLD-deposited YCSB layer partially blocked the leakage current through ceria layer. Ohmic and non-ohmic ASR stability of the cell at 550 ℃ is shown in Figure **7-4** (c). The ohmic ASR of the cell rapidly increased over the first 30 hours of operation at the average rate of 0.145%/h and then plateaued for the remaining 70 hours and non-ohmic ASR of the cell remained stable without any observable degradation. I-V-P curves of the cell were also measured every 5 hours and MPD stability of the cell is shown in Figure **7-4** (d). Following the same trend as the ohmic ASR degradation, MPD of the cell decreased at the average rate of 1.08%/h over the first 30 hours of operation and decreased from the initial value of 1.20 W/cm^2 to ~ 0.8 W/cm^2 and then stabilized.

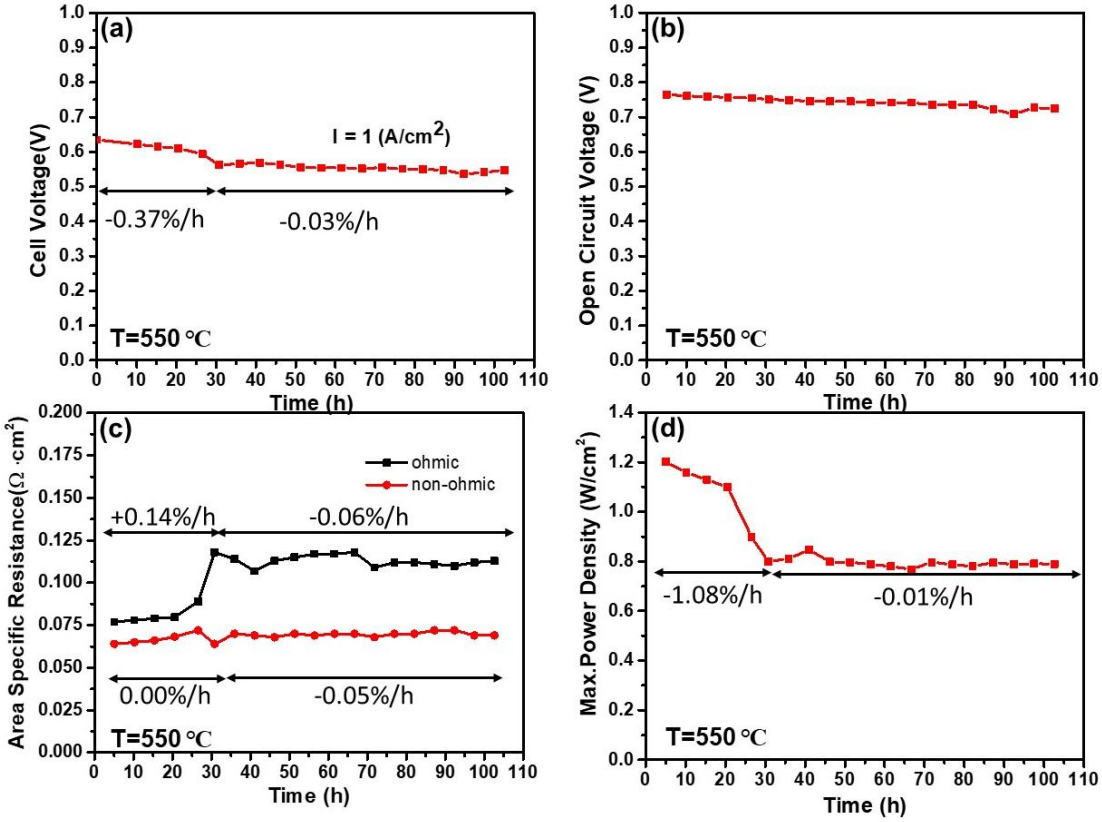


Figure 7-4 Electrochemical stability of Cell (B) at 550 ℃ ;(a) Cell voltage under the constant current density of I=1 A/cm2, (b) OCV, (C) ohmic and non-ohmic ASR of the Cell (B), and (d) MPD

7.2.4 Microstructure

After electrochemical testing, cells were fractured, and cross-section of the cells was carefully examined. Figure **7-5** shows the microstructure of Cell (B) at three different magnifications. The thickness of the GDC and PLD deposited YCSB layers were ~ 7 μm and ~ 2 μm, respectively. The GDC layer was dense with no cracks or pinholes and adhered properly to the adjacent AFL and YCSB electrolyte layer. The thickness of the AFL was approximately 20 μm and the finer grains of the AFL can be differentiated from the coarser grains of the ASL. The microstructure of anode and cathode at a higher magnification, near the electrolyte interface is shown in Figure **7-6**. Relatively large

pores, as result of using pore former in the cathode paste, were observed as shown in Figure **7-6** (a). Presence of infiltrated LSM nanoparticles was also confirmed as shown in Figure **7-6** (a). Size of infiltrated LSM particles after electrochemical testing across the temperature range of 650-500 ℃ followed by 100 hours of operation at 550 ℃ remained in the nano-regime (300-500 nm). It is also worth mentioning that LSM particles were preferentially deposited on the YCSB particles, which could be associated with the wetting properties of the surface. Anode microstructure near the GDC electrolyte is shown in Figure **7-6** (b). Size of infiltrated Ni particles, after electrochemical measurements, was in the range of 30-50 nm. Also, as shown in Figure **7-6** (b), Ni particles were surrounded by the GDC nano clouds, which are helpful to enhance the TPB, leading to high performance.

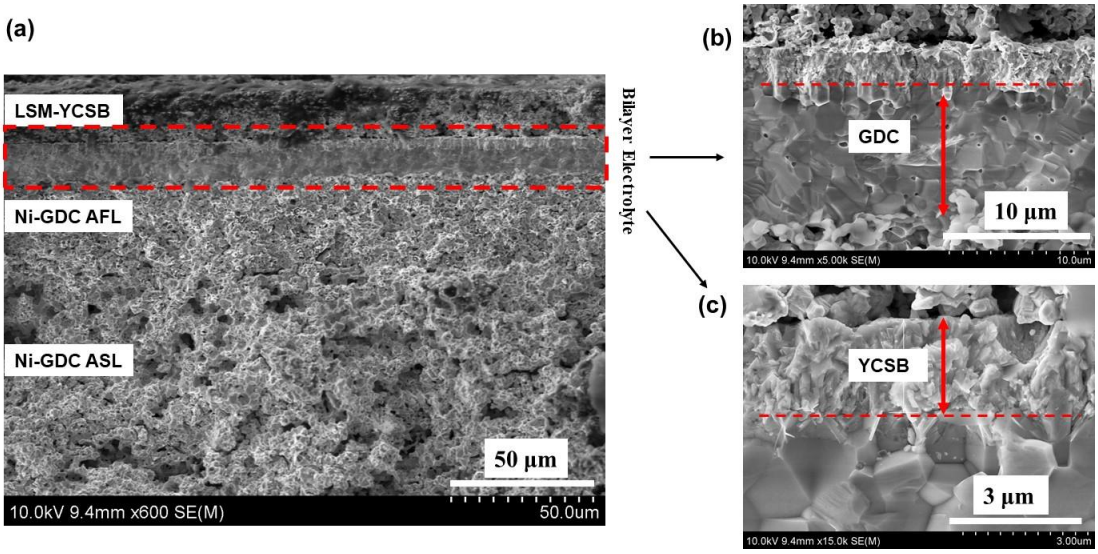


Figure 7-5 SEM micrographs of (a) Ni-GDC/GDC/YCSB/LSM-YCSB cell and GDC/YCSB bilayer electrolyte at (b) 5.00k and (c) 15.00 k magnifications after electrochemical testing

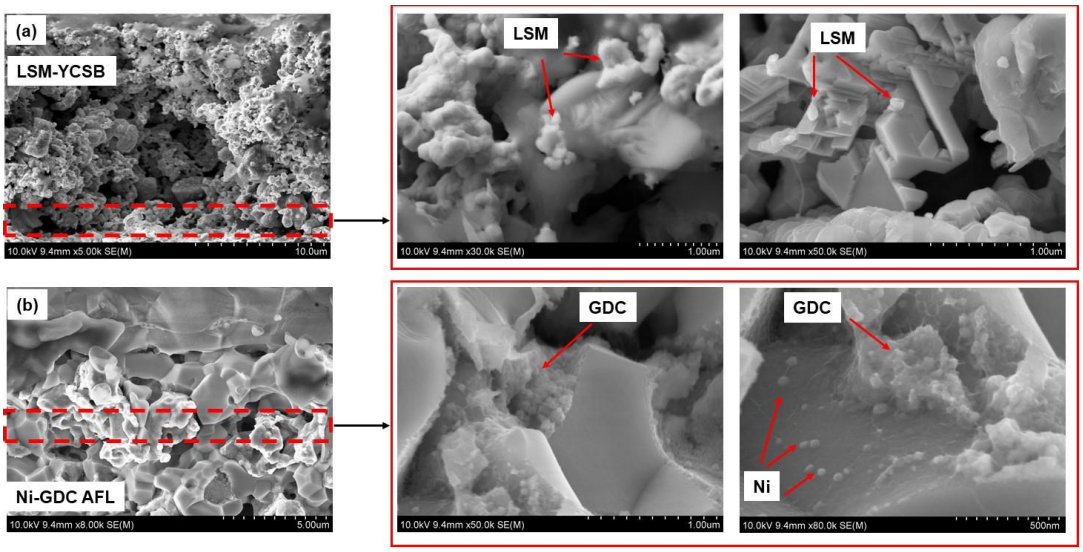


Figure 7-6 SEM micrographs of (a) LSM infiltrated LSM-YCSB cathode near the YCSB electrolyte interface, and (b) Ni-GDC infiltrated AFL near GDC electrolyte interface after electrochemical testing

7.2.5 Symmetrical cells

As discussed in the previous section, infiltration of electrodes reduced the non-ohmic ASR of the cells almost by one order of magnitude. To understand the effect of LSM surface modification on LSM-CYSB cathode, LSM-YCSB/YCSB/LSM-YCSB symmetrical cells were also fabricated and tested. Impedance spectra of two symmetrical cells LSM-YCSB/YCSB/LSM-YCSB with and without LSM infiltration were measured in the temperature range of 650-500 °C. The impedance spectra for the reference and infiltrated cells are shown in Figure **7-7** (a) and (b), respectively. To better compare the effect of infiltration on electrode ASR, the ohmic portions were subtracted from spectra. As can be seen in Figure **7-7** (b), at all tested temperatures, LSM infiltration decreased the impedance of the electrodes significantly.

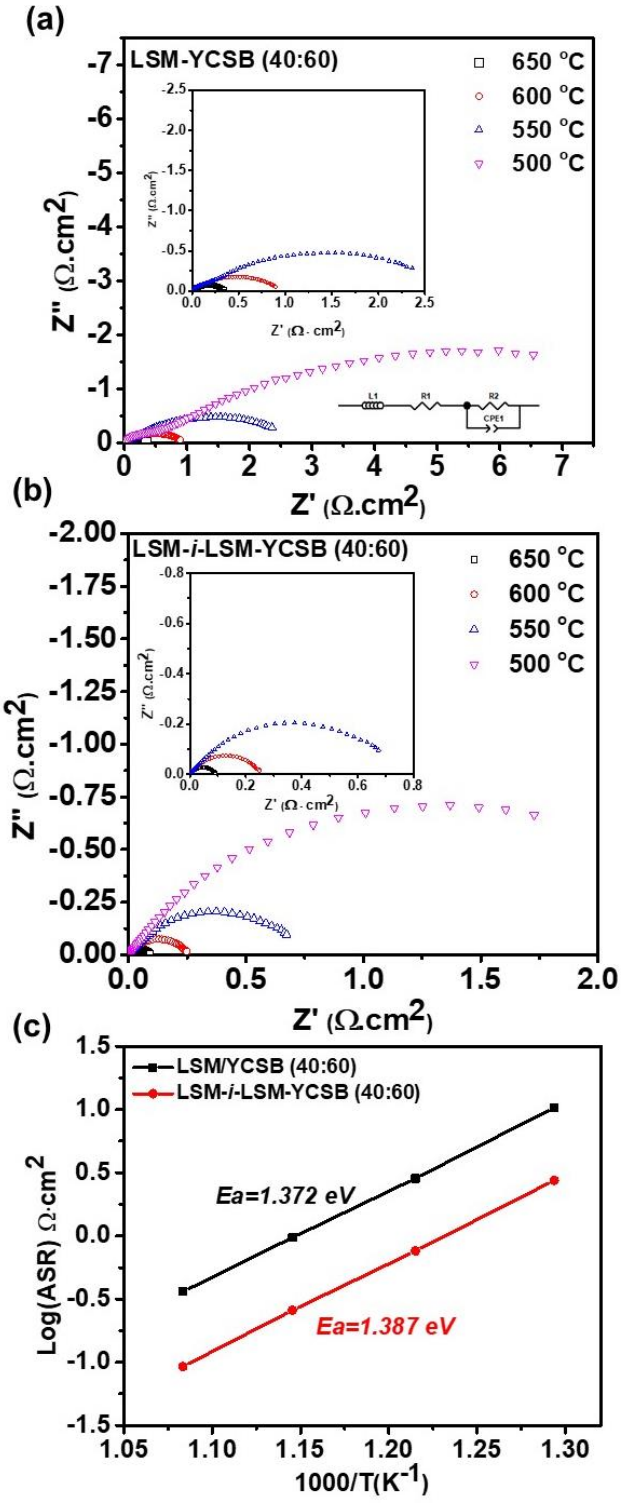


Figure 7-7 Impedance spectra of (a) LSM-YCSB and (b) LSM infiltrated LSM-YCSB across the temperature range of 650-500 ℃ measured at OCV in air, and (c) Arrhenius plot of non-ohmic ASR of LSM-YCSB and LSM infiltrated LSM-YCSB in air

Impedance spectra of both cells were modeled using the equivalent circuit (shown as inset of Figure **7-7** (a)) $LR_0(R_1Q_1)$ where L, R_0, and R_1 are an inductor, ohmic resistance, and polarization resistance, respectively. Arrhenius plot of non-ohmic ASR of both symmetrical cells are shown in Figure **7-7** (c). Non-ohmic ASR of the infiltrated sample was approximately one order of magnitude lower than that of the cell with no infiltration. This is in agreement with the results presented in Figure **7-3** (c) and (d) where the LSM infiltrated cell showed approximately one order of magnitude lower non-ohmic ASR compared to the cell with no electrode infiltration. At 650, 600, 550, and 500 ℃, non-ohmic ASR of the LSM infiltrated LSM-YCSB was 0.09, 0.25, 0.76, and 2.76 $\Omega.cm^2$, respectively. Both samples showed similar activation energy ~ 1.37-1.38 eV which is close to the value reported by Zhang and Huang (1.34 ev) [57] and LSM-ESB cathode developed by Lee et al. (1.23 ev) [81].

Impedance spectra of both samples in the p_{O2} range of (0.02-1) atm were measured at 600 and 550 ℃. Representative impedance spectra at 550 ℃ are shown in Figure **7-8** (a). At both 0.5 and 0.1 atm, LSM infiltration decreased the arc significantly. The shrinkage of the arc was more evident at lower frequencies, suggesting a rapid oxygen reduction reaction (ORR) kinetics through enhancement of dissociative oxygen adsorption process as a result of LSM nano-particle deposition and increase of TPB sites. Unfortunately, the semi-circles associated with different electrode processes overlapped and hence the equivalent circuit shown as inset in Figure **7-7** (a) was used to model the non-ohmic ASR of the cells. Figure **7-8** (b) shows the non-ohmic ASR of both samples as a function of temperature and p_{O2}. Evidently, the infiltrated sample showed lower non-ohmic ASR across the entire p_{O2} range at 550 and 600 ℃.

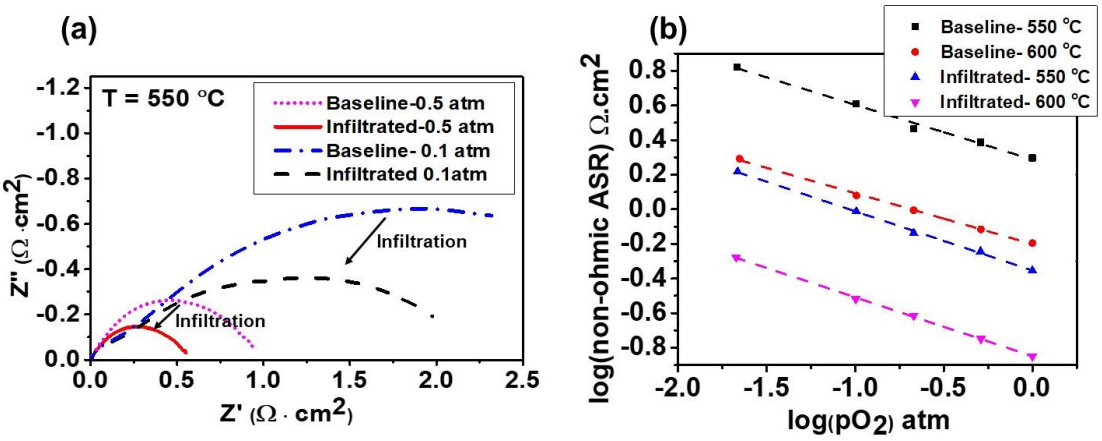


Figure 7-8 (a) impedance spectra of LSM-YCSB and LSM infiltrated LSM-YCSB at 0.5 and 0.1 atm at 550 ℃, and (b) pO2 dependence of non-ohmic ASR for both LSM-YCSB and LSM infiltrated LSM-YCSB at 550 and 600 ℃

After the completion of the temperature and p_{O2} measurement, LSM infiltrated sample was aged at 550 ℃ for 500 hours. Non-ohmic ASR stability of infiltrated LSM-YCSB symmetrical cell is shown in Figure **7-9**. During 500 hours of aging at 550 ℃, non-ohmic ASR of the LSM infiltrated LSM/YCSB electrode showed absolutely no sign of degradation and remained at the stable value of ~ 0.73-0.71 Ω.cm^2, demonstrating exceptional stability. ASR stability of LSM-ESB cathode at 550 ℃ [203] is also shown in Figure **7-9**. LSM-ESB showed a higher initial ASR value of 1.03 Ω.cm^2 and rapidly increased to ~ 2.7 Ω.cm^2 within 150 hours of aging corresponding to the ASR degradation of 1.1%/h. The exceptional stability of the LSM infiltrated LSM-YCSB cathode can be attributed to: (a) stable ohmic ASR (shown in Figure **7-10**) as the oxygen ion conductor phase, and (b) stability of infiltrated LSM nanoparticles formed at the low temperature of 400 ℃ and lack of particles agglomeration during 500 hours of aging test at 550 ℃.

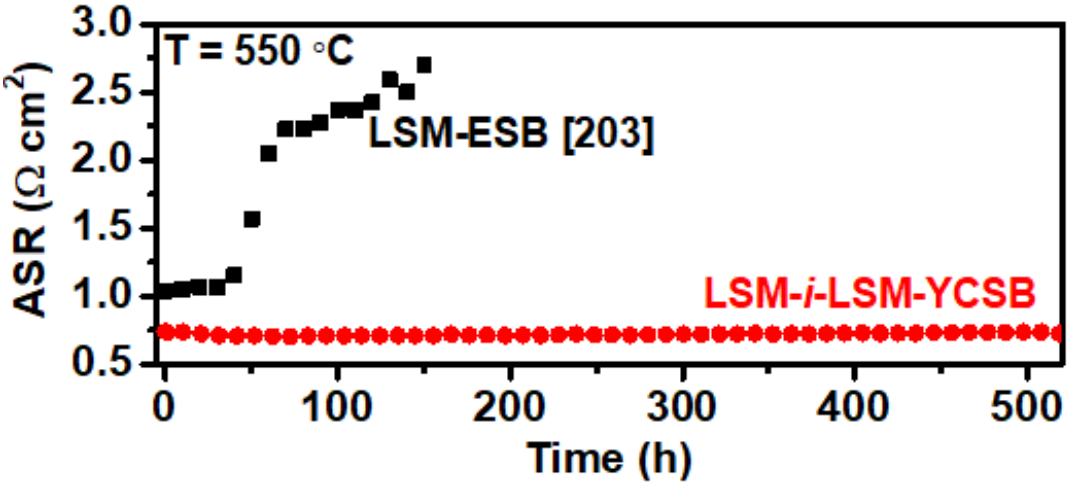


Figure 7-9 Non-ohmic ASR stability of LSM infiltrated LSM-YCSB and LSM-ESB [203] at 550 ℃

Ohmic ASR stability of the infiltrated LSM-YCSB/YCSB/LSM-YCSB symmetrical cell at 550 ℃ was calculated using the $LR_0(R_1Q_1)$ equivalent circuit where L, R_0, and R_1 are an inductor, ohmic resistance, and polarization resistance, respectively. As shown in Figure **7-10**, at 550 ℃, ohmic ASR of the symmetrical cell remained stable at ~ 2.96 $\Omega.cm^2$ with zero degradation over 500 hours of operation suggesting the stable ionic conductivity of YCSB at this temperature.

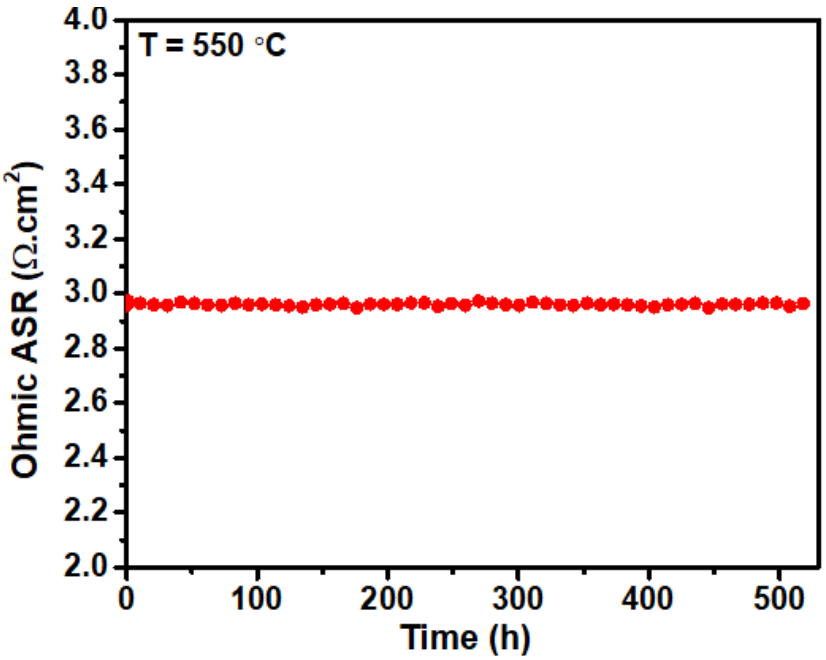


Figure 7-10 Stability of total ohmic ASR of the LSM infiltrated LSM-YCSB symmetrical cell at 550 ℃

8 Conclusions and Future Works

- As outlined in the literature review chapter, lowering the operating temperature of the solid oxide fuel cell below 650 ºC reduces the manufacturing cost, decreases the performance degradation rate, and increases efficiency and hence can promote the commercialization of SOFC technology. Two major approaches to reduce the operating temperature are typically pursued: (a) Using alternative electrolyte materials with higher ionic conductivity such as doped ceria instead of the traditional YSZ, and (b) few microns or sub-micron electrolyte SOFCs. Sub-micron electrolyte SOFCs show reasonable power density at lower temperatures. However, fabrication requires more expensive semi-conductor processing such as advanced lithography, ALD, or sputtering and hence may not be cost effective for large scale power generation potential and so were not reviewed in detail in this work. Doped ceria such as GDC and SDC have ionic conductivity orders of magnitude higher than YSZ and hence have been explored extensively. However, ceria reduces under fuel condition of the SOFC which causes an internal leakage current and power dissipation. Stabilized bismuth oxide compositions such as ESB, YSB and DWSB have been shown to be capable of blocking the leakage current and increasing the OCV of the cell. Although many scholars have investigated the potential of using a thin zirconia layer to block the leakage current, ceria/bismuth oxide bilayer SOFCs showed higher power density values due to the much higher ionic conductivity of stabilized bismuth oxide compared to YSZ. Ceria/bismuth oxide thickness ratio controls the interfacial PO_2 and thus thermodynamic stability of bismuth oxide layer and hence is of great importance and must be tuned carefully. Bilayer electrolyte SOFCs can serve other functions (other

than blocking the leakage current) such as a diffusion barrier layer between electrolyte and adjacent electrodes or enhancing the catalytic activity of the cathode as a fast oxygen ion conductor.

- Gadolinium doped ceria (GDC) and neodymium gadolinium stabilized bismuth oxide (NGSB) bilayer electrolyte based SOFCs were developed for low temperature operation. Anode supported cells with varying thicknesses of GDC and NGSB layers were fabricated by tape casting and blade coating and unit-cells were tested under fuel cell configuration. The electrochemical tests showed that the NGSB layer was able to block the electronic conduction in the GDC layer and increased OCV compared to the baseline single layer GDC cell. For bilayer cells with ~23 μm GDC layer, OCV at 500-550 °C increased with increase in NGSB thickness. At 650 °C, OCV first increased and then decreased with increase in NGSB thickness, suggesting that the thickness ratio was not optimal at high temperatures. For cells with ~38 μm and ~78 μm GDC layer, OCV showed a relatively flat relationship with NGSB thickness. Overall multiple cells were demonstrated with OCV ~1V at 500 °C and the results indicated that the best cell performance in terms of OCV and power density can be achieved with bilayer cells with low GDC/NGSB thickness ratio. Long term stability tests showed low OCV degradation rates with values of <0.002% per hour and <0.012% per hour at 500 and 600 °C, respectively, indicating the exceptional electrochemical stability of GDC/NGSB bilayers.
- Due to the stable ionic conductivity of YCSB, a new anode supported ceria/bismuth oxide bilayer electrolyte LT-SOFC was developed with YCSB as the bismuth oxide layer and oxygen ion conducting phase in the composite cathode. YCSB

was more effective in blocking the leakage current through ceria electrolyte and yielded higher cell OCV comparing to the traditional ESB. Due to the good stability of electrical conductivity of YCSB over annealing across the temperature range of 650-500 ℃, the newly developed bilayer electrolyte SOFC showed an exceptional stability in terms of OCV, ohmic and non-ohmic ASR at 600 and 625 ℃ over 100 h, as compared to SOFCs with GDC/ESB bilayer electrolyte.

- Effect of bismuth oxide/ceria thickness ratio on the performance of the SOFCs was comprehensively examined. All YCSB/GDC bilayer electrolyte SOFCs showed higher power density compared to the single GDC electrolyte cells. Enhancement of power density of the bilayer electrolyte cells was shown to be the result of combined higher OCV and lower ohmic ASR. At 650 ℃, MPD of single electrolyte GDC (20 μm) and GDC (20 μm)/ YCSB (12 μm) bilayer electrolyte cells were 0.64, and 1W/cm^2 respectively. The enhancement of the power density was due to the increase of OCV by 74 mV and reduction of ohmic ASR by 36%. It was demonstrated that all bilayer electrolyte cells showed higher OCV values compared to the respective single GDC electrolyte cell. OCV values reported in this work were higher than all previous ceria/bismuth oxide bilayer electrolyte SOFCs with similar thickness of ceria electrolyte. Interestingly, it was shown that under conditions where GDC reduction is severe, adding the YCSB layer, decreased the ohmic ASR of the cell and does not increase significantly as the thickness of the YCSB layer was increased. However, at lower temperatures (550-500℃) and thicker GDC electrolytes, where GDC reduction is less, a more thickness ratio-dependent behavior was observed. Consequently, we suggest that while at higher temperatures (650-600℃) a thickness ratio that maximizes

the OCV results in highest MPD output, whereas at lower temperatures, a proper thickness ratio considering both OCV enhancement and ohmic ASR of the cell should be considered for advanced high-performing LT-SOFCs.

- To achieve a high power density cell at the low-temperature range of 600-500 ℃, both ohmic and non-ohmic ASR of the cell was minimized using a thin GDC (7-8 μm)/YCSB (2μm) bilayer electrolyte and infiltrated electrodes (LSM at cathode and Ni at anode side), respectively. At 600 and 550 ℃, the power density of the cell reached an exceptionally high value of 1.73 and 1.25 W/cm^2, respectively. The achieved power densities were significantly higher than all previously reported values using non-cobalt cathode materials. Electrochemical stability of the bilayer electrolyte cell with infiltrated electrodes was tested at 550 ℃ over a period of 100 hours. Further, it was shown that OCV and non-ohmic ASR of the cell remained stable. Non-ohmic ASR of LSM-YCSB infiltrated with LSM nano-particles was shown to be one-order of magnitude lower than that of the symmetrical cell without any infiltration. Based on Po_2-dependence studies, it was suggested that LSM nano-particles enhances the ORR kinetics by accelerating the oxygen dissociative adsorption process. The infiltrated symmetrical cell was aged at 550 ℃ for 500 hours with absolutely no sign of degradation of ohmic as well as non-ohmic ASR, suggesting the exceptional stability of infiltrated cathode at 550 ℃.

8.1 Future Works

As discussed in Chapter 5, compared to the traditional bismuth oxide compositions (e.g. ESB), YCSB showed stable OCV and ohmic/non-ohmic ASR. The exact reason behind such behavior is not exactly known at this point. As shown by SEM

micrographs, YCSB has less sinterability compared to ESB which yields to minor porosity in the bismuth oxide layer which and hence could potentially alter the pO_2 at the ceria/bismuth oxide interface. Consequently, effect of bismuth oxide density and fabrication route (i.e. PLD, screen printing, blade coating etc.) on OCV and stability of the cell needs to be studied in more details. In addition, measuring the ionic transference number of YCSB and ESB at different temperatures and pO_2 values, could augment our perception about superior stability of YCSB/GDC bilayer SOFCs.

Following the promising performance of thin GDC/YCSB bilayer electrolyte SOFC in terms of delivered power density and stability in the temperature range of 600-500 °C, incorporation of this new bilayer electrolyte into metal-supported SOFCs is highly suggested.

References

[1] K. Huang, J.B. Goodenough, Solid oxide fuel cell technology: principles, performance and operations, Elsevier, 2009.

[2] S. De Souza, S.J. Visco, L.C. De Jonghe, Solid State Ionics, 98 (1997) 57-61.

[3] J. An, Y.-B. Kim, J. Park, T.M. Gür, F.B. Prinz, Nano letters, 13 (2013) 4551-4555.

[4] Z. Zhan, S.A. Barnett, Science, 308 (2005) 844-847.

[5] E. Fontell, T. Kivisaari, N. Christiansen, J.-B. Hansen, J. Pålsson, Journal of Power Sources, 131 (2004) 49-56.

[6] S.P. Jiang, S.H. Chan, Journal of Materials Science, 39 (2004) 4405-4439.

[7] S. Badwal, Solid State Ionics, 143 (2001) 39-46.

[8] S. Ohara, R. Maric, X. Zhang, K. Mukai, T. Fukui, H. Yoshida, T. Inagaki, K. Miura, Journal of power sources, 86 (2000) 455-458.

[9] M. Mogensen, N.M. Sammes, G.A. Tompsett, Solid State Ionics, 129 (2000) 63-94.

[10] B.C.H. Steele, Solid State Ionics, 129 (2000) 95-110.

[11] J.B. Goodenough, Annual review of materials research, 33 (2003) 91-128.

[12] T. Takahashi, H. Iwahara, Materials Research Bulletin, 13 (1978) 1447-1453.

[13] N. Jiang, E.D. Wachsman, S.-H. Jung, Solid State Ionics, 150 (2002) 347-353.

[14] E.D. Wachsman, P. Jayaweera, N. Jiang, D.M. Lowe, B.G. Pound, Journal of the Electrochemical Society, 144 (1997) 233-236.

[15] N. Jiang, E.D. Wachsman, Journal of the American Ceramic Society, 82 (1999) 3057-3064.

[16] E.D. Wachsman, S. Boyapati, M.J. Kaufman, N. Jiang, Journal of the American Ceramic Society, 83 (2000) 1964-1968.

[17] C. Xia, W. Rauch, W. Wellborn, M. Liu, Electrochemical and solid-state letters, 5 (2002) A217-A220.

[18] C. Xia, W. Rauch, F. Chen, M. Liu, Solid State Ionics, 149 (2002) 11-19.

[19] V. Dusastre, J. Kilner, Solid State Ionics, 126 (1999) 163-174.

[20] E.P. Murray, M. Sever, S. Barnett, Solid State Ionics, 148 (2002) 27-34.

[21] L.-W. Tai, M. Nasrallah, H. Anderson, D. Sparlin, S. Sehlin, Solid State Ionics, 76 (1995) 273-283.

[22] Ö. Çelikbilek, E. Siebert, D. Jauffrès, C.L. Martin, E. Djurado, Electrochimica Acta, 246 (2017) 1248-1258.

[23] Z. Wu, M. Liu, Journal of the American Ceramic Society, 81 (1998) 1215-1220.

[24] C. Xia, M. Liu, (2002).

[25] J.-M. Bae, B. Steele, Journal of electroceramics, 3 (1999) 37-46.

[26] T. Takeda, R. Kanno, Y. Kawamoto, Y. Takeda, O. Yamamoto, Journal of The Electrochemical Society, 147 (2000) 1730-1733.

[27] T. Takeda, R. Kanno, K. Tsubosaka, Y. Takeda, Electrochemistry, 70 (2002) 969-971.

[28] E. Courtin, P. Boy, T. Piquero, J. Vulliet, N. Poirot, C. Laberty-Robert, Journal of Power Sources, 206 (2012) 77-83.

[29] S.M. Haile, Acta Materialia, 51 (2003) 5981-6000.

[30] J. Will, A. Mitterdorfer, C. Kleinlogel, D. Perednis, L. Gauckler, Solid State Ionics, 131 (2000) 79-96.

[31] N.Q. Minh, Journal of the American Ceramic Society, 76 (1993) 563-588.

[32] B.C. Steele, A. Heinzel, Nature, 414 (2001) 345-352.

[33] P. Singh, N.Q. Minh, International Journal of Applied Ceramic Technology, 1 (2004) 5-15.

[34] E.D. Wachsman, K.T. Lee, Science (New York, N.Y.), 334 (2011) 935-939.

[35] T. Tsai, E. Perry, S. Barnett, Journal of the Electrochemical Society, 144 (1997) L130-L132.

[36] E.D. Wachsman, ECS Transactions, 25 (2009) 783-788.

[37] J.Y. Park, H. Yoon, E.D. Wachsman, Journal of the American Ceramic Society, 88 (2005) 2402-2408.

[38] J.-Y. Park, E.D. Wachsman, Journal of the Electrochemical Society, 152 (2005) A1654-A1659.

[39] K. Eguchi, T. Setoguchi, T. Inoue, H. Arai, Solid State Ionics, 52 (1992) 165-172.

[40] S. Zha, C. Xia, G. Meng, Journal of Power Sources, 115 (2003) 44-48.

[41] S. Omar, E.D. Wachsman, J.C. Nino, Applied Physics Letters, 91 (2007) 4106.

[42] S.R. Bishop, T.S. Stefanik, H.L. Tuller, Physical Chemistry Chemical Physics, 13 (2011) 10165-10173.

[43] H. Yahiro, Y. Baba, K. Eguchi, H. Arai, Journal of the Electrochemical Society, 135 (1988) 2077-2080.

[44] J.-Y. Park, E.D. Wachsman, Ionics, 12 (2006) 15-20.

[45] E.D. Wachsman, Solid State Ionics, 152 (2002) 657-662.

[46] L. Zhang, C. Xia, F. Zhao, F. Chen, Materials Research Bulletin, 45 (2010) 603-608.

[47] J.S. Ahn, M.A. Camaratta, D. Pergolesi, K.T. Lee, H. Yoon, B.W. Lee, D.W. Jung, E. Traversa, E.D. Wachsman, Journal of the Electrochemical Society, 157 (2010) B376-B382.

[48] K.T. Lee, D.W. Jung, M.A. Camaratta, H.S. Yoon, J.S. Ahn, E.D. Wachsman, Journal of Power Sources, 205 (2012) 122-128.

[49] L. Zhang, L. Li, F. Zhao, F. Chen, C. Xia, Solid State Ionics, 192 (2011) 557-560.

[50] J. Hou, L. Bi, J. Qian, Z. Zhu, J. Zhang, W. Liu, Journal of Materials Chemistry A, 3 (2015) 10219-10224.

[51] Y. Leng, S. Chan, Electrochemical and solid-state letters, 9 (2006) A56-A59.

[52] T. Takahashi, T. Esaka, H. Iwahara, Journal of Applied Electrochemistry, 7 (1977) 299-302.

[53] S. Boyapati, E.D. Wachsman, B.C. Chakoumakos, Solid State Ionics, 138 (2001) 293-304.

[54] S. Boyapati, E.D. Wachsman, N. Jiang, Solid State Ionics, 140 (2001) 149-160.

[55] A.G. Jolley, E.D. Wachsman, in, SOFC XV, 2017.

[56] K. Huang, M. Feng, J.B. Goodenough, Solid State Ionics, 89 (1996) 17-24.

[57] C. Zhang, K. Huang, Journal of Power Sources, 342 (2017) 419-426.

[58] H.-T. Lim, A.V. Virkar, Journal of Power Sources, 192 (2009) 267-278.

[59] T.-H. Kwon, T. Lee, H.-I. Yoo, Solid State Ionics, 195 (2011) 25-35.

[60] S.-G. Kim, S.P. Yoon, S.W. Nam, S.-H. Hyun, S.-A. Hong, Journal of Power Sources, 110 (2002) 222-228.

[61] A.V. Virkar, Journal of the Electrochemical Society, 138 (1991) 1481-1487.

[62] W.-S. Hsieh, P. Lin, S.-F. Wang, International Journal of Hydrogen Energy, 39 (2014) 17267-17274.

[63] Q.L. Liu, K.A. Khor, S.H. Chan, X.J. Chen, Special issue including selected papers from the International Power Sources Symposium 2005 together with regular papers, 162 (2006) 1036-1042.

[64] Z. Wang, X. Huang, Z. Lv, Y. Zhang, B. Wei, X. Zhu, Z. Wang, Z. Liu, Ceramics International, 41 (2015) 4410-4415.

[65] X. Zhang, M. Robertson, C. Decès-Petit, Y. Xie, R. Hui, W. Qu, O. Kesler, R. Maric, D. Ghosh, Journal of Power Sources, 175 (2008) 800-805.

[66] D. Yang, X. Zhang, S. Nikumb, C. Decès-Petit, R. Hui, R. Maric, D. Ghosh, Journal of Power Sources, 164 (2007) 182-188.

[67] A.A. Solovyev, A.V. Shipilova, I.V. Ionov, A.N. Kovalchuk, S.V. Rabotkin, V.O. Oskirko, Journal of Electronic Materials, (2016) 1-8.

[68] Z. Lu, J. Hardy, J. Templeton, J. Stevenson, D. Fisher, N. Wu, A. Ignatiev, Journal of Power Sources, 210 (2012) 292-296.

[69] J. Qian, Z. Zhu, J. Dang, G. Jiang, W. Liu, Electrochimica Acta, 92 (2013) 243-247.

[70] D.-H. Myung, J. Hong, K. Yoon, B.-K. Kim, H.-W. Lee, J.-H. Lee, J.-W. Son, Journal of Power Sources, 206 (2012) 91-96.

[71] E.O. Oh, C.M. Whang, Y.R. Lee, S.Y. Park, D.H. Prasad, K.J. Yoon, J.W. Son, J.H. Lee, H.W. Lee, Advanced Materials, 24 (2012) 3373-3377.

[72] S. Hui, D. Yang, Z. Wang, S. Yick, C. Decès-Petit, W. Qu, A. Tuck, R. Maric, D. Ghosh, Journal of Power Sources, 167 (2007) 336-339.

[73] B. Timurkutluk, C. Timurkutluk, M.D. Mat, Y. Kaplan, Journal of Power Sources, 196 (2011) 9361-9364.

[74] Y. Jee, G.Y. Cho, J. An, H.-R. Kim, J.-W. Son, J.-H. Lee, F.B. Prinz, M.H. Lee, S.W. Cha, Journal of Power Sources, 253 (2014) 114-122.

[75] M.-H. Wu, J.-L. Huang, K.-Z. Fung, H.-C. Liu, D.-F. Lii, Applied Surface Science, 257 (2011) 7871-7875.

[76] A. Jaiswal, C.-T. Hu, E.D. Wachsman, Journal of The Electrochemical Society, 154 (2007) B1088-B1094.

[77] M. Camaratta, E. Wachsman, Journal of the Electrochemical Society, 155 (2008) B135-B142.

[78] K.T. Lee, A.A. Lidie, H.S. Yoon, E.D. Wachsman, Angewandte Chemie International Edition, 53 (2014) 13463-13467.

[79] E.D. Wachsman, K.T. Lee, Science, 334 (2011) 935-939.

[80] J.S. Ahn, D. Pergolesi, M.A. Camaratta, H. Yoon, B.W. Lee, K.T. Lee, D.W. Jung, E. Traversa, E.D. Wachsman, Electrochemistry Communications, 11 (2009) 1504-1507.

[81] K.T. Lee, D.W. Jung, H.S. Yoon, A.A. Lidie, M.A. Camaratta, E.D. Wachsman, Journal of Power Sources, 220 (2012) 324-330.

[82] J.G. Lee, M.G. Park, H.H. Yoon, Y.G. Shul, Journal of Electroceramics, 31 (2013) 231-237.

[83] J. Hou, L. Bi, J. Qian, Z. Gong, Z. Zhu, W. Liu, Journal of Power Sources, 301 (2016) 306-311.

[84] A.L. Ruth, K.T. Lee, M. Clites, E.D. Wachsman, ECS Transactions, 64 (2014) 135-141.

[85] A. Jaiswal, A. Pesaran, S. Omar, E.D. Wachsman, ECS Transactions, 78 (2017) 361-370.

[86] C. Brahim, A. Ringuedé, E. Gourba, M. Cassir, A. Billard, P. Briois, Selected papers from the 2nd France-Deutschland Fuel Cell Conference2nd France-Deutschland Fuel Cell Conference, 156 (2006) 45-49.

[87] T. Yamaguchi, S. Shimizu, T. Suzuki, Y. Fujishiro, M. Awano, Journal of the Electrochemical Society, 155 (2008) B1141-B1144.

[88] T. Yamaguchi, S. Shimizu, T. Suzuki, Y. Fujishiro, M. Awano, Journal of the Electrochemical Society, 155 (2008) B423-B426.

[89] T. Yamaguchi, S. Shimizu, T. Suzuki, Y. Fujishiro, M. Awano, ECS Transactions, 25 (2009) 939-943.

[90] Y. Lee, Y.M. Park, G.M. Choi, Journal of Power Sources, 249 (2014) 79-83.

[91] R.T. Leah, A. Bone, M. Lankin, A. Selcuk, M. Rahman, A. Clare, L. Rees, S. Phillip, S. Mukerjee, M. Selby, ECS Transactions, 68 (2015) 95-107.

[92] Z. Gao, D. Kennouche, S.A. Barnett, Journal of Power Sources, 260 (2014) 259-263.

[93] E.-O. Oh, C.-M. Whang, Y.-R. Lee, S.-Y. Park, D.H. Prasad, K.J. Yoon, B.-K. Kim, J.-W. Son, J.-H. Lee, H.-W. Lee, Ceramics International, 40 (2014) 8135-8142.

[94] N. Jordan, W. Assenmacher, S. Uhlenbruck, V.A.C. Haanappel, H.P. Buchkremer, D. Stöver, W. Mader, Solid State Ionics 16: Proceedings of the 16th International Conference on Solid State Ionics (SSI-16), Part I, 179 (2008) 919-923.

[95] F.C. Fonseca, S. Uhlenbruck, R. Nedéléc, H.P. Buchkremer, Journal of Power Sources, 195 (2010) 1599-1604.

[96] H.-S. Noh, J. Hong, H. Kim, K.J. Yoon, B.-K. Kim, H.-W. Lee, J.-H. Lee, J.-W. Son, Journal of the Electrochemical Society, 163 (2016) F613-F617.

[97] D. Perednis, L.J. Gauckler, Solid State Ionics, 166 (2004) 229-239.

[98] J. Qian, J. Hou, Z. Tao, W. Liu, Journal of Alloys and Compounds, 631 (2015) 255-260.

[99] T. Mukai, S. Tsukui, K. Yoshida, S. Yamaguchi, R. Hatayama, M. Adachi, H. Ishibashi, Y. Kakehi, K. Satoh, T. Kusaka, Journal of fuel cell science and technology, 10 (2013) 061006.

[100] S. Uhlenbruck, N. Jordan, J.M. Serra, H.P. Buchkremer, D. Stöver, Solid State Ionics, 181 (2010) 447-452.

[101] W. Yu, G.Y. Cho, S. Hong, Y. Lee, Y.B. Kim, J. An, S.W. Cha, Nanotechnology, 27 (2016) 415402.

[102] M.V.F. Schlupp, A. Evans, J. Martynczuk, M. Prestat, Advanced Energy Materials, 4 (2014).

[103] T. Tsai, S.A. Barnett, Journal of the Electrochemical Society, 145 (1998) 1696-1701.

[104] S. Ji, Y.H. Lee, T. Park, G.Y. Cho, S. Noh, Y. Lee, M. Kim, S. Ha, J. An, S.W. Cha, Selected papers from 16th International Conference on Thin Films, October 13-16, 2014, Dubrovnik, Croatia, 591, Part B (2015) 250-254.

[105] H. Uchida, H. Suzuki, M. Watanabe, Journal of the Electrochemical Society, 145 (1998) 615-620.

[106] D. Joh, J. Park, D. Kim, E. Wachsman, K. Lee, ACS applied materials & interfaces, (2017).

[107] S.-F. Wang, Y.-F. Hsu, Y.-C. Huang, W.-C. Wei, Ceramics International, 37 (2011) 2095-2100.

[108] Y.-L. Huang, C. Pellegrinelli, A.S. Painter, E.D. Wachsman, ECS Transactions, 78 (2017) 573-580.

[109] J. Hou, F. Liu, Z. Gong, Y. Wu, W. Liu, Journal of Power Sources, 299 (2015) 32-39.

[110] Y.J. Leng, S.H. Chan, Electrochemical and solid-state letters, 9 (2006) A56-A59.

[111] D.W. Jung, K.L. Duncan, E.D. Wachsman, Acta Materialia, 58 (2010) 355-363.

[112] S. Omar, E.D. Wachsman, J.C. Nino, Applied Physics Letters, 91 (2007) 144106.

[113] A.G. Jolley, E.D. Wachsman, ECS Transactions, 78 (2017) 355-360.

[114] S. Sanna, V. Esposito, J.W. Andreasen, J. Hjelm, W. Zhang, T. Kasama, S.B. Simonsen, M. Christensen, S. Linderoth, N. Pryds, Nature materials, (2015).

[115] T. Ishihara, J. Yan, M. Enoki, S. Okada, H. Matsumoto, Journal of fuel cell science and technology, 5 (2008) 031205.

[116] Y.-W. Ju, H. Eto, T. Inagaki, S. Ida, T. Ishihara, Electrochemical and Solid-State Letters, 13 (2010) B139-B141.

[117] T. Ishihara, H. Eto, J. Yan, The 3rd Annual Korea-USA Joint Symposium on Hydrogen & Fuel Cell Technologies, 36 (2011) 1862-1867.

[118] J. Qian, Z. Zhu, G. Jiang, W. Liu, Journal of Power Sources, 246 (2014) 556-561.

[119] J. Yan, H. Matsumoto, M. Enoki, T. Ishihara, Electrochemical and solid-state letters, 8 (2005) A389-A391.

[120] Z. Bi, B. Yi, Z. Wang, Y. Dong, H. Wu, Y. She, M. Cheng, Electrochemical and solid-state letters, 7 (2004) A105-A107.

[121] Z. Bi, M. Cheng, Y. Dong, H. Wu, Y. She, B. Yi, Solid State Ionics, 176 (2005) 655-661.

[122] D.E. Fowler, J.M. Haag, C. Boland, D.M. Bierschenk, S.A. Barnett, K.R. Poeppelmeier, Chemistry of Materials, 26 (2014) 3113-3120.

[123] Z. Bi, Y. Dong, M. Cheng, B. Yi, Journal of Power Sources, 161 (2006) 34-39.

[124] E. Fabbri, D. Pergolesi, A. D'Epifanio, E. Di Bartolomeo, G. Balestrino, S. Licoccia, E. Traversa, Energy & Environmental Science, 1 (2008) 355-359.

[125] J. Qian, W. Sun, Q. Zhang, G. Jiang, W. Liu, Journal of Power Sources, 249 (2014) 131-136.

[126] J. Qian, W. Sun, Z. Shi, Z. Tao, W. Liu, Electrochimica Acta, 151 (2015) 497-501.

[127] L. Zhao, B. He, J. Shen, F. Chen, C. Xia, Electrochemistry Communications, 13 (2011) 450-453.

[128] W. Sun, Z. Shi, Z. Wang, W. Liu, Journal of Membrane Science, 476 (2015) 394-398.

[129] K.-Z. Fung, T.-Y. Chen, 9th International Symposium on Systems with Fast Ionic Transport, 188 (2011) 64-68.

[130] Y. Mishima, H. Mitsuyasu, M. Ohtaki, K. Eguchi, Journal of the Electrochemical Society, 145 (1998) 1004-1007.

[131] G. Hao, X. Liu, H. Wang, H. Be, L. Pei, W. Su, Solid State Ionics 18 Proceedings of the 18th International Conference on Solid State Ionics Warsaw, Poland, July 3 -8, 2011, 225 (2012) 81-84.

[132] F. Liu, J. Dang, J. Hou, J. Qian, Z. Zhu, Z. Wang, W. Liu, Journal of Alloys and Compounds, 639 (2015) 252-258.

[133] A. Jaiswal, E.D. Wachsman, Journal of the Electrochemical Society, 152 (2005) A787-A790.

[134] K.L. Duncan, K.-T. Lee, E.D. Wachsman, Journal of Power Sources, 196 (2011) 2445-2451.

[135] K.L. Duncan, E.D. Wachsman, Journal of the Electrochemical Society, 156 (2009) B1030-B1038.

[136] S. Wang, T. Kobayashi, M. Dokiya, T. Hashimoto, Journal of the Electrochemical Society, 147 (2000) 3606-3609.

[137] I. Yasuda, K. Ogasawara, M. Hishinuma, T. Kawada, M. Dokiya, Solid State Ionics, 86 (1996) 1197-1201.

[138] B. Steele, Solid State Ionics, 75 (1995) 157-165.

[139] Z. Jiang, C. Xia, F. Chen, Electrochimica Acta, 55 (2010) 3595-3605.

[140] S.P. Jiang, Materials Science and Engineering: A, 418 (2006) 199-210.

[141] Z. Liu, B. Liu, D. Ding, M. Liu, F. Chen, C. Xia, Journal of Power Sources, 237 (2013) 243-259.

[142] S.P. Jiang, International journal of hydrogen energy, 37 (2012) 449-470.

[143] R. Gorte, J. Vohs, Current Opinion in Colloid & Interface Science, 14 (2009) 236-244.

[144] T.Z. Sholklapper, H. Kurokawa, C. Jacobson, S. Visco, L. De Jonghe, Nano letters, 7 (2007) 2136-2141.

[145] T. Sholklapper, C. Jacobson, S. Visco, L. De Jonghe, Fuel Cells, 8 (2008) 303-312.

[146] D. Ding, X. Li, S.Y. Lai, K. Gerdes, M. Liu, Energy & Environmental Science, 7 (2014) 552-575.

[147] S.P. Jiang, S. Zhang, Y.D. Zhen, W. Wang, Journal of the American Ceramic Society, 88 (2005) 1779-1785.

[148] L. Nie, M. Liu, Y. Zhang, M. Liu, Journal of Power Sources, 195 (2010) 4704-4708.

[149] S.P. Jiang, Y.Y. Duan, J.G. Love, Journal of the Electrochemical Society, 149 (2002) A1175-A1183.

[150] S. Jiang, Y. Leng, S. Chan, K. Khor, Electrochemical and solid-state letters, 6 (2003) A67-A70.

[151] S. Jiang, W. Wang, Solid State Ionics, 176 (2005) 1351-1357.

[152] H. He, Y. Huang, J. Regal, M. Boaro, J.M. Vohs, R.J. Gorte, Journal of the American Ceramic Society, 87 (2004) 331-336.

[153] Y. Huang, J.M. Vohs, R.J. Gorte, Journal of The Electrochemical Society, 152 (2005) A1347-A1353.

[154] Z. Jiang, Z. Lei, B. Ding, C. Xia, F. Zhao, F. Chen, international journal of hydrogen energy, 35 (2010) 8322-8330.

[155] Z. Jiang, C. Xia, F. Zhao, F. Chen, Electrochemical and Solid-State Letters, 12 (2009) B91-B93.

[156] T.Z. Sholklapper, C. Lu, C.P. Jacobson, S.J. Visco, L.C. De Jonghe, Electrochemical and solid-state letters, 9 (2006) A376-A378.

[157] N. Xu, X. Li, X. Zhao, H. Zhao, K. Huang, Electrochemical and Solid-State Letters, 15 (2011) B1-B4.

[158] T.J. Armstrong, J.G. Rich, Journal of the Electrochemical Society, 153 (2006) A515-A520.

[159] A. Samson, M. Søgaard, R. Knibbe, N. Bonanos, Journal of the Electrochemical Society, 158 (2011) B650-B659.

[160] S. Lee, K.S. Lee, S.K. Woo, J.W. Kim, T. Ishihara, D.K. Kim, Solid State Ionics, 158 (2003) 287-296.

[161] Y. Huang, K. Ahn, J.M. Vohs, R.J. Gorte, Journal of The Electrochemical Society, 151 (2004) A1592-A1597.

[162] W. Wang, M.D. Gross, J.M. Vohs, R.J. Gorte, Journal of The Electrochemical Society, 154 (2007) B439-B445.

[163] S.P. Simner, M.D. Anderson, M.H. Engelhard, J.W. Stevenson, Electrochemical and Solid-State Letters, 9 (2006) A478-A481.

[164] M. Shah, S. Barnett, Solid State Ionics, 179 (2008) 2059-2064.

[165] X. Lou, S. Wang, Z. Liu, L. Yang, M. Liu, Solid State Ionics, 180 (2009) 1285-1289.

[166] C. Lu, T.Z. Sholklapper, C.P. Jacobson, S.J. Visco, L.C. De Jonghe, Journal of the Electrochemical Society, 153 (2006) A1115-A1119.

[167] F. Liang, J. Chen, S.P. Jiang, B. Chi, J. Pu, L. Jian, Electrochemical and Solid-State Letters, 11 (2008) B213-B216.

[168] S. McIntosh, J. Vohs, R. Gorte, Journal of the Electrochemical Society, 150 (2003) A470-A476.

[169] S. Jiang, W. Wang, Y. Zhen, Journal of power sources, 147 (2005) 1-7.

[170] D. Ding, W. Zhu, J. Gao, C. Xia, Journal of Power Sources, 179 (2008) 177-185.

[171] H. Kurokawa, T.Z. Sholklapper, C.P. Jacobson, L.C. De Jonghe, S.J. Visco, Electrochemical and Solid-State Letters, 10 (2007) B135-B138.

[172] A.M. Hussain, J.V. Høgh, W. Zhang, P. Blennow, N. Bonanos, B.A. Boukamp, Electrochimica acta, 113 (2013) 635-643.

[173] A.M. Hussain, J.V. Høgh, T. Jacobsen, N. Bonanos, international journal of hydrogen energy, 37 (2012) 4309-4318.

[174] R. Craciun, S. Park, R. Gorte, J. Vohs, C. Wang, W. Worrell, Journal of The Electrochemical Society, 146 (1999) 4019-4022.

[175] S. Park, J.M. Vohs, R.J. Gorte, Nature, 404 (2000) 265.

[176] Z. Wang, W. Weng, K. Cheng, P. Du, G. Shen, G. Han, Journal of Power Sources, 179 (2008) 541-546.

[177] L. Liu, K. Sun, X. Wu, X. Li, M. Zhang, N. Zhang, X. Zhou, international journal of hydrogen energy, 37 (2012) 10857-10865.

[178] P. Jasinski, T. Suzuki, V. Petrovsky, H.U. Anderson, Electrochemical and Solid-State Letters, 8 (2005) A219-A221.

[179] A. Busawon, D. Sarantaridis, A. Atkinson, Electrochemical and Solid-State Letters, 11 (2008) B186-B189.

[180] A. Buyukaksoy, V. Petrovsky, F. Dogan, Journal of the Electrochemical Society, 159 (2012) B666-B669.

[181] Q. Fu, F. Tietz, Fuel Cells, 8 (2008) 283-293.

[182] H. Uchida, N. Mochizuki, M. Watanabe, Journal of The Electrochemical Society, 143 (1996) 1700-1704.

[183] A. Babaei, S.P. Jiang, J. Li, Journal of the Electrochemical Society, 156 (2009) B1022-B1029.

[184] L.L. Zheng, X. Wang, L. Zhang, J.-Y. Wang, S.P. Jiang, international journal of hydrogen energy, 37 (2012) 10299-10310.

[185] S.P. Jiang, Y. Ye, T. He, S.B. Ho, Journal of Power Sources, 185 (2008) 179-182.

[186] G. Corre, G. Kim, M. Cassidy, J. Vohs, R. Gorte, J. Irvine, Chemistry of materials, 21 (2009) 1077-1084.

[187] G. Kim, S. Lee, J. Shin, G. Corre, J. Irvine, J. Vohs, R.J. Gorte, Electrochemical and Solid-State Letters, 12 (2009) B48-B52.

[188] S. Lee, G. Kim, J.M. Vohs, R.J. Gorte, Journal of The Electrochemical Society, 155 (2008) B1179-B1183.

[189] Y.-L. Huang, A.M. Hussain, E.D. Wachsman, Nano Energy, 49 (2018) 186-192.

[190] T. Hays, A.M. Hussain, Y.-L. Huang, D.W. McOwen, E.D. Wachsman, ACS Applied Energy Materials, 1 (2018) 1559-1566.

[191] C. Duan, J. Tong, M. Shang, S. Nikodemski, M. Sanders, S. Ricote, A. Almansoori, R. O'Hayre, Science, 349 (2015) 1321-1326.

[192] Q. Liu, K.A. Khor, S. Chan, Journal of Power Sources, 161 (2006) 123-128.

[193] C. Xia, M. Liu, Solid State Ionics, 144 (2001) 249-255.

[194] Y.-W. Ju, S. Ida, T. Inagaki, T. Ishihara, Solid State Ionics, 216 (2012) 58-63.

[195] J. Hwang, H. Lee, J.-H. Lee, K.J. Yoon, H. Kim, J. Hong, J.-W. Son, Journal of Power Sources, 274 (2015) 41-47.

[196] J.G. Lee, M.G. Park, S.-H. Hyun, Y.G. Shul, Electrochimica Acta, 129 (2014) 100-106.

[197] H.-S. Noh, K.J. Yoon, B.-K. Kim, H.-J. Je, H.-W. Lee, J.-H. Lee, J.-W. Son, Journal of Power Sources, 247 (2014) 105-111.

[198] X. Zhang, M. Robertson, S. Yick, C. Deĉes-Petit, E. Styles, W. Qu, Y. Xie, R. Hui, J. Roller, O. Kesler, Journal of power sources, 160 (2006) 1211-1216.

[199] J. Kim, W.-y. Seo, J. Shin, M. Liu, G. Kim, Journal of Materials Chemistry A, 1 (2013) 515-519.

[200] Z. Shao, S.M. Haile, Nature, 431 (2004) 170.

[201] W. Zhou, Z. Shao, R. Ran, W. Jin, N. Xu, Chemical Communications, (2008) 5791-5793.

[202] S. Yoo, A. Jun, Y.W. Ju, D. Odkhuu, J. Hyodo, H.Y. Jeong, N. Park, J. Shin, T. Ishihara, G. Kim, Angewandte Chemie International Edition, 53 (2014) 13064-13067.

[203] A.S. Painter, Y.-L. Huang, E.D. Wachsman, Journal of Power Sources, 360 (2017) 391-398.